Geological-Material Model Complexity Level and Excavation Sequencing on Numerical Modelling of Progressive Failure in Deep Open-Pit Slopes: A Case Study in a Porphyry Deposit Mine

by

Andrés Felipe Puerta Mejía

A thesis submitted in partial fulfillment of the requirements for the degree of

Master of Science

in

Geotechnical Engineering

Department of Civil and Environmental Engineering
University of Alberta

Abstract

This research delves into the intricate dynamics of progressive rock slope failure and its significant impact on the stability of deep open pit mining operations (over 500 meters according to Li et al., 2022), focusing on the crucial aspect of inter-ramp failure (large scale). The primary objective of this study is to comprehensively evaluate the implications of different levels of detail in Geological and Material models. Moreover, the research explores the intricate influence of various pushback sequencings (Excavation sequences) on the accurate modelling of progressive failure in deep open-pit slopes, thereby highlighting the depth of our study.

The research methodology employs a meticulous back analysis strategy to accurately replicate inter-ramp failure within a principal slope of a deep open pit mine. A series of geometrical pushback sequence models are systematically constructed, incorporating various levels of detail in Geological and Material models. This modelling spectrum ranges from simplified representations using homogeneous elastic materials to more intricate scenarios involving lithology differences, hydrothermal alterations, and Mohr-Coulomb with strain-softening materials, thereby instilling confidence in the thoroughness of our approach.

The modelling process commences with creating detailed geometrical models in Rhino V7.0 software, followed by a comprehensive analysis in Itasca's FLAC3D V.7.0 software. The evaluation of model results includes in-depth comparisons of

displacement records, stress patterns, plastic strain, shear strain, and volumetric strains. This rigorous analytical approach aims to discern the subtle implications of increasing levels of detail in Geological and Material models on the forecasting accuracy of progressive failure.

Moreover, in the context of this case study, our research delves into the influence of different pushback sequences on the progression of failure. The results of this study underscore the significant impact of pushback sequencing choices on the initiation and extent of progressive slope failure, given the diverse stress paths within the slope. This comprehensive investigation significantly enhances our comprehension of the intricate interplay between excavation sequencing, stress paths, and slope stability, emphasising the importance of our findings.

According to the results of thorough model comparisons, there is a direct relationship between realistic depictions of progressive failure and the detailing levels of Geological and Material models. This relationship is created while critically considering various pushback sequences. Using fewer complex models allows for establishing restrictions for residual parameters related to strain-softening materials, expediting the iterative calibration process for more complicated models.

The study underscores the pivotal role of Geological-Material Model Complexity and Excavation Sequencing in projecting progressive failure in deep open-pit slopes. Through an in-depth analysis of a Porphyry Deposit Mine, novel insights emerge. Integrating geological complexities into numerical models is a crucial prerequisite for

predicting progressive collapse. The most intricate geotechnical model, encompassing multiple lithologies, their alterations, and a strain-softening material behaviour model, is the most effective, accurately reproducing failure zone characteristics. Excavation sequencing significantly influences failure development, with different pushback sequences hastening or postponing failure initiation, thereby impacting the magnitude and spread. Pushback geometry, such as slope angle and spacing, is closely linked to failure initiation and progression. These findings provide unique perspectives on mitigating slope instability hazards in open-pit mining. Further research is needed to validate and generalise these findings across diverse geological contexts, considering additional factors such as large-scale fractures.

Preface

Versions of Chapters 3 and 4 from this thesis are being prepared for submission to the Engineering Geology journal with the following citations:

Puerta-Mejía, A.F., Deisman, N., Macciotta, R., O'Neil, S., and Eberhardt, E. 2024. Numerical modelling of progressive failure due to mine sequencing of a deep open pit slope: Importance of the geotechnical model in validating against a back-analysis. University of Alberta Geotechnical Centre [Unpublished].

Puerta-Mejía, A.F., Deisman, N., Macciotta, R., O'Neil, S., and Eberhardt, E. 2024. Numerical modelling of progressive failure due to mine sequencing of a deep open pit slope: Importance of the excavation sequencing in failure development. University of Alberta Geotechnical Centre [Unpublished].

A summary version of Chapter 3 from this thesis was published by the Australian Centre For Geomechanics, ACG, as a part of the SSIM 2023: Third International Slope Stability in Mining conference proceedings with the following citation:

Puerta-Mejía, AF, Deisman, N & Macciotta, R 2023, 'The importance of geological and material model detail in modelling progressive failure: Andes deep open pit', in PM Dight (ed.), SSIM 2023: Third International Slope Stability in Mining Conference, Australian Centre for Geomechanics, Perth, pp. 315-332, https://doi.org/10.36487/ACG_repo/2335_18

Dedication

This endeavour is dedicated to the most important, to God, to the Blessed Virgin Mary, and to my beloved parents, Libardo de Jesús and Aura Rosa, whose guidance and love have been the pillars of my life. To my cherished family, your steadfast support has strengthened and encouraged me throughout this journey. Additionally, I extend heartfelt gratitude to all my relatives who passed away during this challenging time: Aunty Oliva de Jesús, who was like a second mother and taught me about my grandparents, ancestors and family's rich history; Uncle José Ignacio, who showed me how cool science and engineering is, from him I learnt to love literature and History as well, to Aunties Luz Elena and Nora, they taught me to follow my dreams, Uncle Luis Guillermo who I take as an example of responsibility and sacrifice for the family. All of them whose unwavering reassurance and understanding have been invaluable as I diligently worked towards the fruition of this endeavour.

Acknowledgements

I sincerely thank my supervisor, Dr. Renato Macciotta Pullisci, and Dr. Nathan Deisman from the University of Alberta for their steadfast support and guidance throughout my academic journey. Dr Macciotta has been instrumental in not only providing me with the opportunity to pursue this degree but also, despite the family issues and health problems I had during this endeavour, in never giving up and encouraging me to keep going to enhance my personal and professional skills.

I am also deeply appreciative of the invaluable contributions and support of Dr Erik Eberhardt and Shane O'Neill from the University of British Columbia, Dr Carlos Carranza-Torres from the University of Minnesota-Duluth, and Dr Nicolás Labanda from the University of Buenos Aires and WSP Australia. Their expertise has greatly enhanced the outcomes of this research.

I extend my heartfelt thanks to Fernando Villegas, Leonardo Cornejo, and Rigoberto Rimmelin from BHP, as well as Ashley Craighton from Rio Tinto, for their collaboration and support, which have been indispensable to the success of this project.

Special recognition is also due to the LOP project for the opportunity to collaborate and the resources provided. I am also immensely grateful to the Mitacs programme for its economic support.

Additionally, I want to thank my colleagues at the University of Alberta Geotechnical Centre, especially Sonam Choden, Ingrid Berrú, Myzael Valdivia, Gustavo Velarde and Luiz Biagini for their partnership, advice, discussions, comments, and support

Table of Contents

1 **Introduction** 1

1.1 Background 1

1.2 Problem Description 6

1.3 Thesis Objectives 7

1.4 Overview of the Methodology 8

1.5 Outline of the Thesis 10

2 **Literature Review** 12

2.1 Open Pit Mining Terminology 12

2.2 Progressive Failure 16

2.2.1 Progressive Failure in Intact Rock 17

2.2.2 Progressive Failure in Rock Masses 17

2.3 Progressive Failure in Rock Slopes 18

2.4 Models to Assess Progressive Failure 19

2.4.1 Mohr-Coulomb with Strain Softening 20

2.5 Assessing Progressive Failure in Slopes 21

2.5.1 Factors Affecting Assessing 22

2.5.2 Back-Analysis Technique 22

2.5.3 Numerical Modelling 23

2.6 Porphyry Deposits 26

2.6.1 Porphyry Deposits Alteration Types 26

2.6.2 Materials Geomechanical Properties 28

3 **Numerical modelling of progressive failure due to mine sequencing of a large open pit slope: Importance of the geotechnical model in validating against a back-analysis** 29

3.1 Contributions made to this Chapter: 29

3.2 Abstract 30

3.3 Introduction 31

3.4 Case Study 33

3.5 Geological Setting 35

3.5.1 Lithology 35

3.5.2 Rock Mass Alterations 35

3.5.3 Major Structural Features 37
3.6 In-Situ Stresses 37
3.7 Water Conditions 38
3.8 Materials Parameter and Geotechnical Model 38
3.9 Case Study Progressive Failure Event 40
3.10 Modelling Process 44
3.10.1 Model Characteristics and Assumptions 48
3.11 Results 54
3.12 Discussion 69
3.13 Conclusions 74
3.14 Acknowledgements 77

4 Effect of Excavation Sequence in the development of Inter-Ramp Progressive failure in deep open pit slopes 78
4.1 Contributions made to this Chapter: 78
4.2 Abstract 79
4.3 Introduction 80
4.4 Case Study 83
4.4.1 Geological Setting 85
4.4.2 Major structural features, In-situ stresses and Water conditions 86
4.4.3 Material Parameters and Geotechnical Model 87
4.5 Modelling Process 93
4.5.1 Model's Characteristics and Pushback Sequencings 95
4.6 Results and Discussion 100
4.7 Conclusion 116
4.8 Acknowledgements 117

5 Conclusion and Future Work Recommendations 118

Bibliography 122

Appendix: Details about the calibration process 156

List of Tables

Table 3-1. Major faults in the mine zone and its characteristics. (Data provided by the mine's operator, 2021) 37
Table 3-2. Geomechanical parameters compiled for the key rock mass domains in the modelled area of the mine, according to their lithology and alteration type. 40
Table 3-3. Criteria used to establish whether a model can be calibrated, with increasing level of fit. 50
Table 3-4. Failure characteristics of the NE wall, and the other walls where failure did not occur, compared to the results for the different model types. 57
Table 3-5. Geomechanical parameters back analysed for the EPP type models. The domains that were involved in the observed failure are identified by an asterisk. 61
Table 3-6. Geomechanical parameters back analysed for the SS-type models. The best fitting parameters for the Lit+Alt-SS model is enclosed in a red rectangle. The domains that were involved in the observed failure are identified by an asterisk. 62
Table 4-1. Major faults characteristics at the mine zone. (From mine's operator data. 2021) 87
Table 4-2. Geomechanical parameters compilation for the mine site outcropping materials, according to their lithology and alteration type. Rapiman and Sepulveda (2006) as well as Valdivia and Lorig (2001) 89
Table 4-3. Geomechanical parameters from back analysis procedure in calibrated model. The failure got through those marked with an asterisk. 100
Table 4-4. Summary of results involving the onset of failure timing, the pushback orientation, pushback inclination degree, and comparatives between the required excavated material (ore extracting) to the onset of failure and the maximum involved volume in the failure. 106
Table 4-5. Summary of trial model geometrical characteristics with failure order (onset of failure) 110

List of Figures

Figure 2-1. Some of the main geometrical features in open pits.. 16
Figure 3-1. Plan view of the open pit case study (modified from Google Earth, 2019). The failure appears as the disturbed area in the northeast corner of the pit, with the longitudinal section line A-A passing through the slide and the transversal section line B-B crossing the toe of the failed zone. The corresponding profiles are provided in Figure 3-2..33
Figure 3-2. Mining and open-pit pushback sequence, shown for (a) Profile B-B (see Figure 3-1), which crosses NW-SE through the pit and provides a section through the pushback in the NW wall. The outline of the failed zone projected onto the NE wall is shown as a pink dashed line. (b) Cross profile A-A, provides a longitudinal section through the NE wall where the failed zone developed, as shown in Figure 3-1. 34
Figure 3-3. Site geology, including isometric and sectional views along A-A (see Figure 3-1), showing the distribution of (a) lithologies and (b) alteration types, as mapped in the open pit with the outline of the failed area shown by the dashed red line. (Data derived from Garza et al., 2001; model built using Rhinoceros 3D, V. 7.0., McNeel, R., & others., 2020). 36
Figure 3-4. Geotechnical model showing the distribution of lithological and hydrothermal alteration units built into the numerical model and their relationship to the outline of the failed zone location, as seen in (a) isometrical view, and (b) along profile A-A. Model built using FLAC3D V. 7.0., Itasca Consulting Group, Inc. (2019). 39
Figure 3-5. General procedure for obtaining displacement estimates for the period between the initiation of slope movements and 2017, when geodetic monitoring of the slope began. (Modified from Google Earth, 2017). 41
Figure 3-6. Cumulative displacement plot of a tracking point (CP) located on the failed mass and corresponding trend derived from satellite imagery. Also shown are images outlining the evolution of cracking coinciding with the boundary of the unstable area. 42
Figure 3-7. Slope failure spatial characteristics, as outlined relative to (a) an isometric view and (b) along cross-section A-A in the direction of slip movement. Model built using FLAC3D V.7.0., Itasca Consulting Group, Inc. (2019)..43
Figure 3-8. Flowchart showing the modelling procedure and consideration of geological and behaviour model complexity levels. 45
Figure 3-9. Flowchart detailing the model set-up process. 46

Figure 3-10. Flowchart illustrates the sub-routine followed to calibrate the models through back analysis of the case study failure. 47
Figure 3-11. Geometric locations of the material zonation used in the model, relative to: (a) an isometric view showing the overall model size and detailing of the failed zone, and (b) section B-B with the simplified excavation sequencing. 51
Figure 3-12. Mesh and model characteristics. Model built using Rhinoceros 3D V. 7.0., Griddle V. 2.0., McNeel, R., & others. (2020), and Itasca Consulting Group, Inc. (2020), respectively. 51
Figure 3-13. (a) Illustration of the strength degradation curve concept for strain softening, with typical shape for slope stability analyses as proposed by Renani and Martin (2020). (b) Example of a strength degradation curve used in this work. 52
Figure 3-14. Monitoring points incorporated into the model to track the model responses. (a) Isometric view with monitoring points within and external to the failed zone, and (b) cross sectional view showing the monitoring points at surface and depth. 53
Figure 3-15. Isometric view showing the slope displacement contours 55
Figure 3-16. Cross section view A-A showing the slope displacements with depth for the final pushback excavation sequence, as a function of increasing complexity in the geological model .56
Figure 3-17. Time history of displacements for the different model types compared to the reference measured slope displacements....57
Figure 3-18. Bar charts comparing the modelled failure characteristics for each model type to the actual failure values shown by the black dashed line....58
Figure 3-19. History plot of the plastic strains versus time for the different model types. 59
Figure 3-20. History plot of the volumetric strains versus time for the different model types. 59
Figure 3-21. History plot of the maximum shear strain rate versus time for the different model types. 60
Figure 3-22. Bar charts presenting the change in the rock mass strength parameters as a function of geological and behaviour model complexity for the domains involved in the failure. 63
Figure 3-23. Summary plot comparing the back analysed peak and residual strength parameters for the different model variants and typical values obtained in previous studies involving porphyry deposit lithologies (modified from Wyllie & Mah, 2017 after Hoek & Bray, 1981). 65
Figure 3-24. Element failure type (shear versus tension) at different key stages in the pushback sequence for the best fitting model (Lit+Alt-SS). Results from model built on FLAC3D V. 7.0., Itasca Consulting Group, Inc. (2019)....66
Figure 3-25. Comparison between the different model type stress paths and Mohr-Coulomb peak and residual strength envelopes, assuming homogeneous model strengths for simplicity: 68
Figure 3-26. Displacement outcomes relative to the geological model domain contacts.... 71

Figure 4-1. Hypothetical stress paths on a principal stress plane, that states that onset of failure timing depends on excavation sequence characteristics. 82
Figure 4-2. Google Earth's plan view of the open pit, with failure zone profiles and project location, modified from Google (2019). 83
Figure 4-3. Actual open-pit pushback sequence (numbered colours in the legend), pit's transversal (A) and longitudinal (B) cross profiles (adapted from data provided by the mine operator, 2021).. 84
Figure 4-4. Isometric and cross profile views of the outcropping lithologies at the open pit failed area (Built from Garza et al. 2001 descriptions, using Rhinoceros 3D V.7.0, McNeel and others, 2020)...85
Figure 4-5. Isometric view and cross profile of the different alteration types at the open pit failed area (Built from Garza et al. 2001 descriptions, using Rhinoceros 3D V.7.0, McNeel and others, 2020).. 86
Figure 4-6. Geotechnical model summarising lithological and hydrothermal alteration materials' distribution and their relationship regarding failed zone location, (a) Isometrical view, and (b) profile A's view. An, ES, PZ and Rh correspond to the different lithologies Andesite, Stockwork, Paleozoic Andesite and Rhyolite, respectively. The alteration type is noted after a dash mark. Model built on FLAC3D V. 7.0., Itasca Consulting Group, Inc. (2019)....................................... 88
Figure 4-7. General procedure for obtaining displacement estimates. For example, the methodology application for June 2017 (modified from Google. 2017) 90
Figure 4-8. History plot of a tracking point onto the failed mass, and images showing cracking evolution (from data provided by the operator in 2021. imagery modified from Google. 2007 2011, 2013, 2016).. 91
Figure 4-9. Failure characteristics: (a) Isometric view with movement extension, (b) Cross section A with slip surface features. Analysis model with data provided by mine operator. 2021, and built on FLAC3D V.7.0., Itasca Consulting Group, Inc. (2019)..92
Figure 4-10. Flow chart showing the general procedures for analysing the excavation sequencing on modelling progressive failure in deep open-pit slopes. 93
Figure 4-11. Base model characteristics (calibrated model): (a) Plan and cross profile views with overall model's dimensions and mesh grading, (b) Longitudinal cross profile (B) with the simplified actual mine's pushback sequence. 95
Figure 4-12. Schematic view of the cross profile (B) showing the geometrical parameters to define the modelling trial excavation sequences. 96
Figure 4-13. Example of the distribution of each theta, Ht pairs that represent individual pushbacks presented in Figure 4-15 for each excavation sequence (Case 1 to Case 5, and

Calibrated model inclusive). 97
Figure 4-14. Average geometric characteristics for each excavation sequence defined in Figure 4-15. 98
Figure 4-15. Trial model sequencings, where excavation order is given by letters in the tables: (a) Isometric view for Case 1 and Case 2, (b) Cross profile and Isometric for Case 3, and (c) Cases 4 and 5. Models built on Rhinoceros 3D V. 7.0., McNeel, R., & others. 99
Figure 4-16. Comparative history plots of displacements in a monitoring point located onto failed mass and within failed contour for each pushback sequence model. 101
Figure 4-17. Isometrical view shows each modelled case's failure extension at the final stage (Pushback 19). Results from FLAC3D V. 7.0., Itasca Consulting Group, Inc. (2019) 103
Figure 4-18. Cross profile (A) view showing the failure depth, extension, and shape achieved by each modelled case at the final stage (Pushback 19). Results from FLAC3D V. 7.0., Itasca Consulting Group, Inc. (2019) 104
Figure 4-19. History plots of each excavation sequence case showing how the involved in the failure material at the actual failed site evolves throughout pushbacks. 105
Figure 4-20. Comparative plots between the excavated material volume in percentage versus the unstable volume generated (affected volume) for each excavation sequence. 105
Figure 4-21. History plot of the excavated material throughout the nineteen (19) pushbacks for each excavation sequence defined in Figure 4-15, and their maximum excavation rate (dashed lines) before the onset of failure (dots). 107
Figure 4-22. Stress paths from the MS-2 monitoring point across nineteen (19) excavation stages, displayed on principal stress spaces with pushback sequencing and a calibrated model. Each plot includes the Mohr-Coulomb shear strength envelopes for slip surface materials involved in failure...109
Figure 4-23. Distribution of excavation sequence cases pushbacks according to their overall height and slope (represented by dots), and group them according whether they inflict instabilities (red colour) on NE wall or not (green colour)..111
Figure 4-24. a) Ht and theta pairs according to case groups and pushback orientation, b) Ht and θ pairs distribution with affected volume on NE wall (colours) and stability line (separation between stable and unstable pushback individual cases)..113
Figure 4-25. Stress path envelope for all the evaluated cases.. 114
Figure 4-26. Effects of pushback average geometric characteristics (θ, and Ht,), orientation, and excavation sequence rate on the onset of failure order...115
Figure 7-1. Rhino 3D model (Isometric View) comprised of surfaces and poly-surfaces enclosing

watertight regions. 157
Figure 7-2. Illustration of the various types of flaws and defects that can occur in polygon meshes. Taken from Attene et al (2013). 158
Figure 7-3. Spotted stress concentration after an elastic running at a previous to open-pit excavation stage. 161
Figure 7-4. Elastic run showing vertical stresses increasing at depth. The stage is previous to any pushback excavation in the open-pit. 161
Figure 7-5. Elastic run showing maximum principal stresses increasing at depth and redistributed by a pushback excavation. 162
Figure 7-6. Elastic run showing displacement settlements with vectors before any open-pit pushback excavation. 162
Figure 7-7. Elastic run showing displacement (Elastic rebound) with vectors at an open-pit pushback excavation. 163
Figure 7-8. Schemme showing different C and Phi combinations and their effects regarding slip surface shape and position. 165
Figure 7-9. A plot of recommended dilation angle to friction angle relationships according to GSI material values from Lorig and Varona (2013) guidelines for the numerical assessment of underground structures. Enclosed are the values considered for the main lithologies for the present case study. The plot also depicts the effect of varying dilatancy on the model´s failure development. 167
Figure 7-10. A plot of recommended critical strain relationships according to GSI material values, from Lorig and Varona (2013) guidelines to underground structures numerical assessment. The plot also depicts the effect of varying critical strain on the model´s failure development. 167
Figure 7-11. Plot depicting the effect of different post-peak degradation parameters shape curves on the model´s failure development. 168
Figure 7-12. Plot of typical values obtained in previous studies involving porphyry deposit lithologies (modified from Wyllie & Mah, 2017 after Hoek & Bray, 1981). 168
Figure 7-13. Scheme showing results of a hypothetical plastic run for an SS-type model after applying initial geomechanical parameters where no significant displacements or failure is produced. 171
Figure 7-14. Scheme showing results of a hypothetical plastic run for a SS type model after applying adjusts to the initial geomechanical parameters in Figure 7-13, at this time significant displacements or failure is produced. Previous adopted parameters are represented as grey dots. 172

Figure 7-15. Scheme showing results of a hypothetical plastic run for an SS-type model after applying adjusts to the previous step in Figure 7-14; at this time, failure is close to the actual characteristics. Previously adopted parameters are represented as grey dots. 173

Chapter 1
Introduction

1.1 Background

Progressive failure in geotechnical engineering, particularly in rock slopes and the open-pit mining industry, has been the subject of extensive research and analysis. This phenomenon is primarily driven by high lateral stresses in the soil or rock masses before excavation (Potts et al., 1997). It is important to note that progressive failure and strain localisation phenomena occur in geotechnical engineering, where materials exhibit brittle or strain-softening properties (Tang & Chen, 2016). This is particularly relevant in the context of open-pit mining. Safety in open-pit mining, which is crucial for the efficiency of operations, is managed through monitoring and TARPS (trigger action and response plans).

The study of progressive failure in geotechnical engineering has been supported by finite element analysis development, which has been used to understand the mechanisms and factors contributing to gradual deterioration in various geotechnical structures, such as embankments and cut slopes (Potts et al., 1990). Additionally, numerical analysis has been employed to investigate the behaviour of soils with strain-softening properties, providing insights into the occurrence of progressive failure in these materials (Troncone, 2005).

In open-pit mining, the geomechanical stabilisation of rock masses during ore extraction from open pits has been identified as a significant challenge (Stupnik, 2023). This highlights the importance of understanding the factors contributing to progressive failure in rock slopes within the industry, as they directly impact the transition to alternative energy sources.

The impact of open-pit mining on groundwater levels has been studied, particularly in regions such as the Baorixile Coal Mine in Northeast China (Du et al., 2022). The drainage operations during open-pit mining have been found to trigger a drop in groundwater levels, leading to a cone of depression. In some cases, the excess pore pressure generated and the implemented depressurisation schemes have been one of the causes of progressive failure in slopes. For example, Troncone et al. (2019) discussed how excess pore water pressure can arise from rapid water recharge or phreatic level rise, potentially leading to slip and landslides. Similarly, Igwe et al. (2006) emphasised the role of excess pore water pressure as a triggering factor for soil landslides, highlighting its impact on soil fluidisation. Furthermore, Wang and Sassa (2008) explored how the generation of excess pore water pressure, in combination with factors like shear displacement and dissipation inhibition, can contribute to post-failure landsliding.

On the other side, the stability of open pit slopes in high-altitude and cold regions has been investigated, considering factors such as freeze-thaw effects on the stability of rock slopes (Hong et al., 2021). This demonstrates the diverse environmental and geological factors influencing progressive failure in open-pit mining areas.

The study of progressive failure in geotechnical engineering, particularly in rock slopes and the open-pit mining industry, encompasses various interdisciplinary research areas, including geology, environmental science, and materials engineering.

Recent advances in the study of progressive failure in geotechnical engineering, particularly in rock slopes and the open-pit mining industry, have seen significant contributions from various research endeavours. One notable area of advancement is the application of Discrete Element Method (DEM) analysis to understand step-path failure in jointed rock slopes (Scholtès & Donzé, 2015). This approach has enabled researchers to reproduce the progressive failure mechanisms occurring in jointed rock slopes, providing valuable insights into the behaviour of such geological formations.

The modelling of step-path failure of rock slopes with intermittent joints using fracture mechanics and the strength reduction method has contributed to a deeper understanding of progressive failure in jointed rock slopes (Huang et al., 2014). This approach has facilitated the development of calculation methods for Stress Intensity Factors (SIF) in jointed rock slopes, shedding light on the factors influencing their stability.

The development of numerical manifold methods for analysing the progressive failure of rock slopes has provided a robust framework for studying the failure processes and stability calculation models of rock slopes with intermittent joints (Zhou et al., 2021). This advancement has significantly contributed to the comprehensive understanding of the failure mechanisms in such geological formations.

In addition to advancements in numerical analysis techniques, recent developments in reliability analysis, particularly in the context of aero-engine rotor systems, have provided valuable insights into efficient reliability analysis and its applications in complex engineering structures (Li et al., 2021).

While this reference is not directly related to geotechnical engineering, the principles and methodologies developed in reliability analysis can be adapted and applied to enhance the reliability assessment of geotechnical structures and systems and then applied to the field of the progressive failure study.

Developing a multiscale work-analysis approach for geotechnical structures has contributed to theoretical advancements in solving geotechnical engineering problems (Xiong et al., 2019). This approach has the potential to enhance the understanding of geotechnical structures' behaviour under various loading conditions, thereby contributing to the overall knowledge of progressive failure at the micro-meso and macroscales (the last traditional approaches).

Another research stream is the application of artificial neural systems in geotechnical engineering, which has provided valuable insights into the potential use of advanced computational techniques in addressing geotechnical challenges (Shahin et al., 2009). This signifies the ongoing efforts to integrate advanced computational methods into geotechnical engineering practices, potentially leading to more efficient and accurate analyses of geotechnical problems.

Other endeavours have focused on the study of the role of temperature in strength deterioration, indicating an increasing focus on the mechanical characteristics and deformation failure of surrounding rock support in geotechnical engineering (ZHANG et al., 2023). This highlights the importance of considering environmental factors in analysing progressive failure in geotechnical structures and systems.

Whilst theoretical and numerical analysis has given us valuable insights, historical case studies of progressive failure in open-pit slopes have provided important information into the geotechnical challenges and failure mechanisms usually encountered in mining operations. These case studies have contributed to understanding slope stability, rock mass behaviour, and the impact of mining activities on the surrounding environment. Several notable historical case studies shed light on the geotechnical aspects of progressive failure in open-pit mining.

One case study uses inverse velocity to forecast potential rock slope failure in open-pit mines. This method provides critical insights into predicting potential slope failures in open-pit mining environments (Rose & Hungr, 2007). This study highlights the importance of advanced prediction methods in mitigating potential slope failures that occur gradually in open-pit mining areas.

Another significant case study focused on the monitoring and early warning of brittle slope failures in hard rock masses in an open pit mine, providing examples of progressive failure in hard rock masses and the challenges in identifying precursors to failure events was presented by Carlà et al., (2017). This study emphasised the importance of early-warning systems and the complexities of monitoring brittle slope failures in open-pit mining environments.

To the above aspect, the delayed collapse of cut slopes in stiff clay provided a historical case study of progressive failure, demonstrating the considerable impact of progressive failure and the observed field behaviour in cut slopes (Potts et al., 1997). This case study highlighted the challenges and implications of delayed collapse in open-pit mining environments.

Moreover, the emergence of new monitoring technologies, such as the integration of ground-based radar and satellite InSAR data for the analysis of an unexpected slope failure in an open-pit mine, has provided insights into the unexpected failure mechanisms Carlà et al. (2018). This study demonstrated the application of advanced data integration for analysing unexpected slope failures in open-pit mining environments.

Remote analysis of an open-pit slope failure in the Las Cruces case study, Spain, demonstrated the use of remote sensing technologies for analysing slope failures, emphasising the importance of advanced monitoring and analysis techniques in open-pit mining environments (López-Vinielles et al., 2020). This study showcased the potential of remote analysis for understanding slope failures in open-pit mining areas, and the case studies show the importance of such slope behaviour information for the reliable understanding of slope failure mechanisms through adequately calibrated numerical models.

Historical case studies of progressive failure in open-pit slopes have played a crucial role in understanding geotechnical challenges, failure mechanisms, and the complexities of slope stability in mining operations. These case studies have contributed to developing innovative technologies, best practices, and mitigation strategies for ensuring the safety and sustainability of open-pit mining activities.

1.2 Problem Description

Progressive failure in open-pit mining presents complex challenges influenced by geological and material model complexities and excavation sequencing. While advancements in numerical modelling provide insights, systematic calibration approaches are needed due to complexities in tool and geological contexts. Moreover, optimising pushback designs requires considering ore extraction, excavated volumes, and the potential for progressive failure initiation and timing. Yet, a systematic tool for optimisation is lacking. Understanding these complexities is crucial for improving safety and efficiency in mining operations, which are managed through monitoring and TARPS. The study aims to address these gaps by assessing geological model complexity, proposing a systematic back analysis method for slope failure at a large scale (inter-ramp scale), and exploring the effects of excavation sequencing for a deep open pit (over 500 meters depth, Li et al., 2022). By investigating these factors, the study aims to enhance understanding and management practices of progressive failure in deep open-pit mining, contributing to safer and more efficient mining practices.

1.3 Thesis Objectives

The overall thesis objective is to provide a systematic method for back analysis and slope geometry optimisation that considers the complexities of the geological context and the potential and timing for the onset of progressive failure at an inter-ramp scale (large scale) for over 500 meters depth open pits (deep open pits according to Li et al., 2022). The study aims to achieve the following specific objectives:

1- Assessment of Geological Model Complexity: The first objective is to assess the impact of geological model complexity on the accuracy of numerical modelling of progressive failure, which previous authors have not explicitly evaluated. This involves comparing models of varying complexity, from simple homogeneous representations to more detailed models incorporating lithological variations and alterations. By doing so, the study seeks to determine what lithological features are essential for proper numerical modelling representing a progressive failure phenomenon in deep open pit slopes. Large-scale fractures are not part of the scope of this work.

2- Propose and illustrate a systematic method for slope failure back analysis that can be consistently adopted in open-pit mining slope analysis: This method aims to validate numerical models against real-world data by comparing them with observed failure zones. Factors such as failure location, shape, depth, affected volume, and other criteria will be assessed to determine the accuracy of different numerical modelling approaches. The validation process will include utilising on-field monitoring displacement data in history plots to enhance the reliability of the analysis. Although back analysis of open pit slope instability cases is found throughout technical literature, detailed flow charts and procedures like the ones that will be presented are scarce.

3- Exploration of Excavation Sequencing Effects: The study also aims to investigate the influence of excavation sequencing (pushback sequencing) on the onset and progression of failure in deep open-pit slopes. By analysing different pushback sequences and their impact on failure magnitude, spatial extent, and onset of failure timing in a real case study (previous authors have done it for hypothetical cases and non-realistic material models like elastic ones), the study aims to provide insights into the role of excavation planning in mitigating slope instability risks for deep open pit mining.

1.4 Overview of the Methodology

The methodology is based on the analysis of a case study to develop and illustrate the methods proposed. Each chapter outlines the procedures in detail, and an overall methodology summary is presented here. The technique outlined in the text encompasses several crucial steps to comprehensively assess the impact of geological-material model complexity and excavation sequencing on the numerical modelling of progressive failure at a large scale (inter-ramp scale) in deep open-pit slopes (over 500 meters depth, Li et al., 2022).

The method begins with gathering pertinent information, where comprehensive data on site geology and typical geotechnical parameters are collected along with data about the mine and the failure mechanism: pit shells, pushback sequencing, and displacement monitoring. This involves studying technical literature to understand the geological composition of the site, including lithologies, hydrothermal alterations, fault systems, and other pertinent geological features. Geotechnical parameters such as rock mass strength, cohesion, friction angles, and deformation modulus are typically collected or estimated based on similar or nearby geological formations.
Following data gathering, the following steps involve planning the model types (in number and characteristics) and constructing numerical models based on the collected information. This includes building the geometry of the pit slopes, incorporating geological features such as lithologies and alterations, and defining material properties and boundary conditions. The model geometry is constructed using Rhino software and then meshed to ensure compatibility with FLAC3D modelling software.

The calibration process is then undertaken to refine the numerical models. This includes verifying stress-strain behaviour and comparing displacement history to ensure alignment with observed data. Adjustments to model parameters are made iteratively until the simulated outcomes closely match the observed data obtained from field observations, literature review, and satellite imaging.

Once the models are calibrated, the results analysis begins. This involves simulating failure with various geological complexities and excavation sequencing scenarios to identify trends, patterns, and correlations between geological parameters, excavation sequences, and slope stability. Key metrics such as failure mechanisms, surfaces, displacement fields, and stress distributions are evaluated and compared across different model scenarios.

Finally, based on the analysis of the results, conclusions are drawn. These conclusions provide insights into the influence of geological-material model complexity and excavation sequencing on the predictability of progressive failure in deep open-pit slopes. They may include recommendations for optimising excavation sequences, adjusting geotechnical parameters, or enhancing numerical modelling techniques to improve the predictability and management of slope instability risks in similar mining contexts.

1.5 Outline of the Thesis

Chapter 1 introduces the thesis's background, problem statement, and objectives, emphasising the study field's importance for mine safety and operational efficiency. It then discusses the impact of geological-material model complexity and excavation sequencing on numerical modelling accuracy.

Chapter 2 thoroughly examines the causes of progressive failure in intact rock and rock masses and the various material models and numerical approaches used for slope stability analysis. It defines a porphyry deposit and, drawing on previous research, explains the importance of hydrothermal alterations in geotechnical material properties.

Chapter 3 describes a systematic approach for back-analysing pit slope failure, considering increasing levels of geologic complexity until a balance between accuracy and model complexity is achieved. It illustrates the approach with a case study.

Chapter 4 analyses the influence of excavation sequence on the possibility and timing for the onset of slope progressive failure. It presents an approach to consider excavation sequences for optimising pushback designs.

The thesis finishes with Chapter 5, which summarises its significant results and recommends further research.

Chapter 2

Literature Review

2.1 Open Pit Mining Terminology

The terminology commonly employed in the open pit mining industry, as delineated by **Error! Reference source not found.** and Stacey (2009), has been adopted in the present work to articulate the case study and analysis outcomes. Figure 2-1 has been included to facilitate reader comprehension.

Bench face: A bench face is a step-like excavation level in mine walls, critical for safe and efficient mining operations (Holwell & Jordaan, 2006).

Bench: Benching involves creating levelled platforms in mine walls, which is essential for safety, efficiency, and environmental considerations (Morales & Panthi, 2017; Toderas & Filatiev, 2021).

Berm: Berms are levelled areas in pit walls designed to prevent material movement, evolving from transport routes to safety features (Toderas & Filatiev, 2021).

Bench height and width: Bench height and width are critical parameters influencing efficiency and safety. Bench height, ranging from 12 to 30 meters in iron ore pits, is optimized for safety and slope stability (Sobko et al., 2022). Bench width, typically around 20 meters, accommodates heavy equipment (Oyebamiji et al., 2019).

Bench face angle: The bench face angle, or the inclination of the vertical face of a bench, significantly affects stability, efficiency, and safety. Stable slopes usually range from 10° to 30°, which is crucial for preventing hazards and ensuring safe operations (Oyebamiji et al., 2019).

Pit's floor: The pit floor serves as the foundation for mining activities, with its stability and safety crucial for production (Hindy, 2021; Li et al., 2022). Recirculation flow and groundwater dynamics impact its stability (Chen, 2023; Du et al., 2022). Bench design is key in optimizing the pit floor, affecting ore recovery and mining efficiency (Haile & Konka, 2021). Post-mining, the pit floor may form a pit lake, requiring proper future land use planning (Tuheteru et al., 2021).

Ramp: Ramps connect working faces to pit exits, facilitating material transportation for processing or disposal (Haile & Konka, 2021). Configurations like spiral ramps optimise equipment operation and productivity (Pysmennyi et al., 2022). They ensure efficient access to different pit levels, enhancing operational efficiency and safety by providing stable access for personnel and equipment.

Wall: Walls are vertical or near-vertical rock faces surrounding excavations, providing essential structural support (Bagdasaryan & Sytenkov, 2014). Wall stability is crucial to preventing accidents and maintaining excavation integrity (Sdvyzhkova et al., 2022).

Toe: The toe marks the lowest point where the slope or wall meets the ground surface, serving as a critical boundary (Dintwe et al., 2021). Toe stability is vital for overall safety and integrity, as it is susceptible to stresses induced by mining activities, necessitating continuous monitoring and management to prevent slope failures (Zhang et al., 2022; Taji et al., 2012).

Crest: The crest is the highest point or upper boundary of a slope or wall within the pit, defining excavation limits (Dintwe et al., 2021). It significantly influences slope stability and safety, necessitating careful monitoring and management (Traykovski et al., 2007). The crest's role in determining excavation geometry and structural integrity is crucial for preventing collapses and ensuring worker safety (Haile & Konka, 2021).

Inter-benches: Inter-benches are horizontal or near-horizontal surfaces separating benches, crucial for slope design and stability (Grenon & Laflamme, 2011). They provide platforms for equipment and material handling, enhancing operational efficiency and safety. Factors like width, height, and slope angle influence their stability and accessibility, requiring careful planning (Grenon & Laflamme, 2011).

Inter-ramp: Inter-ramp angles refer to the angles between successive ramps or benches, crucial for slope stability and optimisation (Grenon & Laflamme, 2011). Optimal inter-ramp geometry is vital for safety and productivity, considering factors like groundwater drawdown (Borges et al., 2023). Monitoring these angles is essential to prevent slope instability, often using technologies like camera networks (Zhang et al., 2021).

Overall angle: The overall slope angle in open-pit mining refers to the angle of inclination of the entire slope surface, crucial for stability, safety, and operational efficiency (Hu et al., 2022). Optimization of this angle is essential for ensuring safe mining practices and maximizing economic viability (Maleki et al., 2011; Hryhoriev, 2023).

Pushback: A pushback signifies a defined area for material extraction, crucial for mine planning and production scheduling (Goodfellow & Dimitrakopoulos, 2013). Designing and optimizing pushbacks is vital for maximising the net present value (NPV) of mine production schedules (Goodfellow & Dimitrakopoulos, 2013). The distance between pushbacks is determined considering operational constraints like bench width and wall slope angle (Maiti et al., 2021). Optimal spacing ensures safe operations, material extraction efficiency, and project economic viability (Maiti et al., 2021). By assessing factors such as equipment productivity and geological uncertainty, engineers determine the ideal pushback distance to meet production targets and economic goals (Araya et al., 2020).

Ore body: An ore body in open-pit mining refers to the natural concentration of minerals that can be extracted economically. It is a mineralized rock that contains valuable minerals or metals that can be mined and processed for profit. Ore bodies can vary in size, shape, and composition, influencing the mining methods and techniques used for extraction (Dintwe et al., 2021). These deposits can be suitable for different mining methods, such as underground mining or open-pit mining, depending on factors like depth, ore quality, and stability requirements (**Error! Reference source not found.** et al., 2021).

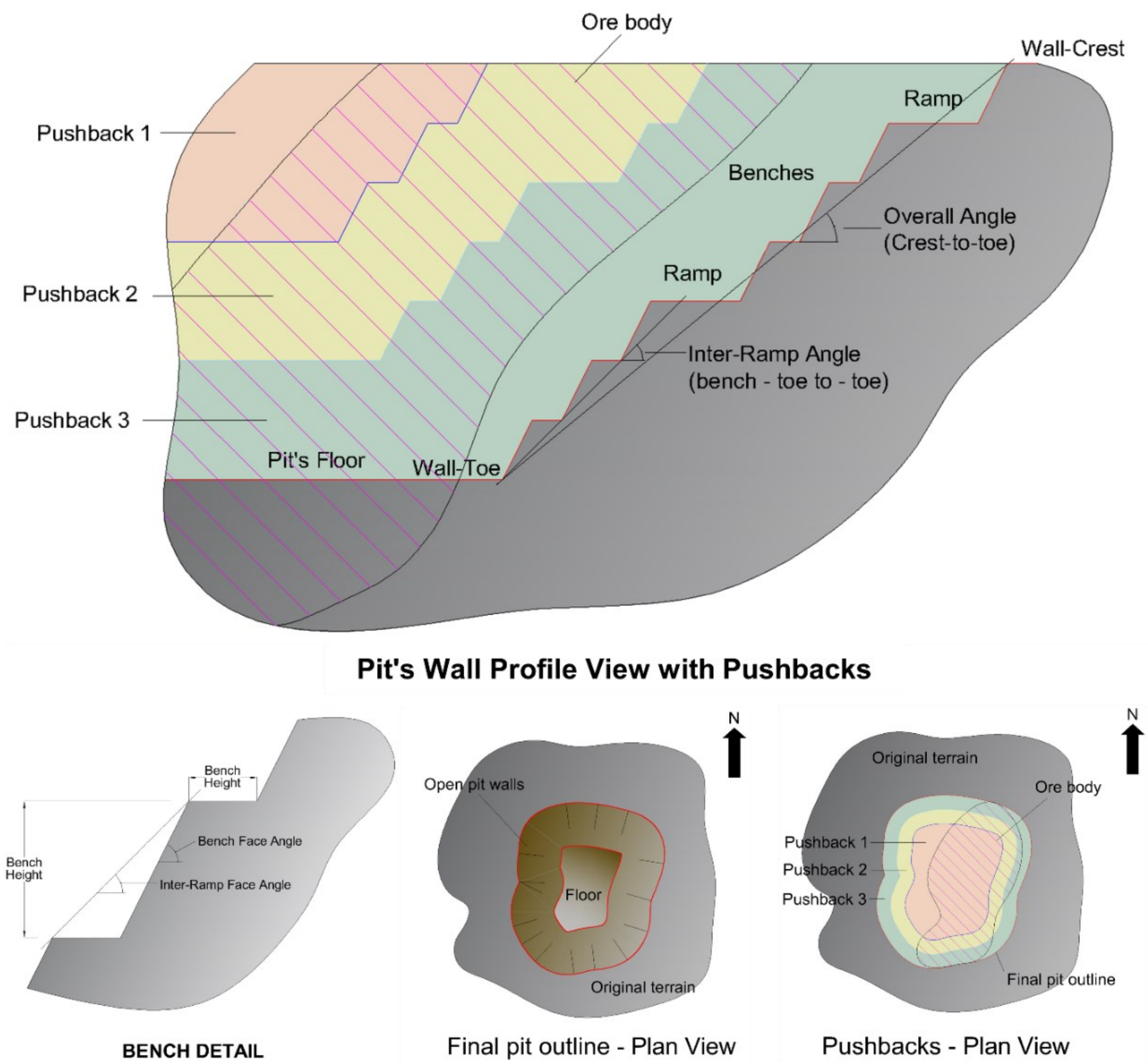

Figure 2-1. Some of the main geometrical features in open pits.

2.2 Progressive Failure

Progressive failure in geotechnical engineering, marked by gradual instability, is influenced by factors like non-uniform loading and strain-softening behaviour (Tang et al., 2017; Potts et al., 1997). This phenomenon poses risks to various structures, from slope collapses to embankment failures (Potts et al., 1997; Potts et al., 1990). Strain localisation, a consequence of progressive failure, affects underground constructions and dam base rock stability (Tang & Chen, 2016; Song et al., 2020). Understanding and mitigating progressive failure are crucial for effective risk management, preventing catastrophic failures and ensuring worker and environmental safety (Spross et al., 2021; Spross et al., 2017).

2.2.1 Progressive Failure in Intact Rock

Progressive failure in intact rock, influenced by factors like non-uniform loading and strain-softening behaviour, involves gradual instability, observable from microcracking to fragmentation (Huang et al., 2020; Davidsen et al., 2021; Strauhal & Zangerl, 2021). This process surpasses shear strength and releases seismic energy, providing insights into the deterioration of material integrity (Guo et al., 2020). Quantifying intact rock bridge failure involves fracture coalescence and crack growth driven by time-dependent changes in situ stresses, highlighting its complexity (Strauhal & Zangerl, 2021).

2.2.2 Progressive Failure in Rock Masses

Progressive failure in rock masses involves gradual material instability influenced by the ones previously mentioned, and high lateral stresses (Wang et al., 2020; Zangerl et al., 2021; Luo et al., 2018). Laboratory and field tests reveal stages marked by fracturing, internal shear zones, and block failure (Zangerl et al., 2021). Reservoir water level fluctuations can induce creep deformation as a predominant failure type (Luo et al., 2018), while stress-dominated failure, notably affected by in situ stress, is common (Wang et al., 2020).

Rock masses, unlike intact rock, have structural defects like joints and fractures, crucial in progressive failure and influencing mechanical, thermal, and hydraulic behaviours (Jiang et al., 2009). Deformation mechanisms and stability depend on existing discontinuities and stress-induced crack generation during excavation (Jiang et al., 2009). Weak interlayers lead to distinct failure characteristics, with soft rocks prone to cracking and hard rocks prone to tensile splitting (Miao et al., 2023). Anisotropy of compressive strength affects the progressive failure process (Han & Tang, 2010).

2.3 Progressive Failure in Rock Slopes

Progressive failure in rock slopes involves gradual instability, leading to various types of slope failures influenced by geological discontinuities, seismic activity, weathering, and human activities (Zhang et al., 2022; Guo et al., 2020; Roshankhah, 2022; Premasiri, 2018; Azmi & Yu, 2023).

Rock slope progressive failure entails the gradual development of cracks, deformation, and collapse, resulting in rockfalls, rockslides, and rock topples, posing risks to infrastructure and the environment (Zhang et al., 2022; Guo et al., 2020; Roshankhah, 2022). Seismic events trigger catastrophic consequences, while accumulated deformation energy and confinement loss contribute to dynamic instability (Zhang et al., 2022; Roshankhah, 2022). Discontinuities induce structurally controlled slope instability, while weathering processes weaken rock masses, increasing vulnerability to rockslides (Donati et al., 2019; Riva et al., 2018).

Human activities exacerbate rock slope failure through inadequate construction practices and monitoring (Azmi & Yu, 2023). Case studies like the Rhombus Wall rock fall in Yosemite Valley and the Tianshan Road slope under freeze-thaw cycles provide insights into time-dependent discontinuity propagation and in situ accumulation post-failure (Stock et al., 2012; Zhang et al., 2021).

2.4 Models to Assess Progressive Failure

Assessing progressive failure in soils and rocks involves utilising various constitutive models to capture their complex behaviour under loading conditions. These models have been extensively studied and applied in geotechnical engineering and research. Below are the characteristics, advantages, disadvantages, and applications of the most used constitutive models:

- **Elasto-Plastic Model:**
  - Characteristics: Widely used for its ability to capture non-linear rock behaviour.
  - Advantages: Effective in simulating plastic deformation and progressive failure.
  - Disadvantages: May lack full representation of time-dependent behaviour and require calibration.
  - Applications: Commonly used in tunnel deformation and failure simulations (Li et al., 2022).

- **Mohr-Coulomb Constitutive Model:**
  - Characteristics: Frequently used for simulating soil and rock behaviour.
  - Advantages: Provides a simple approach for capturing shear strength and failure behaviour.
  - Disadvantages: May not fully represent complex non-linear behaviour or time-dependent effects.
  - Applications: Used in deep excavation and slope stability analysis (Li et al., 2022).

- **Strain-Softening Constitutive Model:**
  - Characteristics: Effective in simulating progressive failure of slopes.
  - Advantages: Captures softening behaviour crucial for understanding progressive failure.
  - Disadvantages: Requires careful calibration and validation.
  - Applications: Widely used in dynamic stability simulations of slopes under earthquake conditions (Ai et al., 2022).

- **Viscoelastic Plastic Model:**
  - Characteristics: Describes rheological deformation of deep rock.
  - Advantages: Captures time-dependent behaviour and viscoelastic response.
  - Disadvantages: Requires complex parameter determination and computational challenges.
  - Applications: Suitable for simulating rheological deformation in deep rock and well drilling analysis (Fang et al., 2021).

- **Hoek-Brown Failure Criterion-Based Creep Constitutive Model:**
  - Characteristics: Based on the Hoek-Brown failure criterion for soft rock mass creep simulation.
  - Advantages: Practical for capturing long-term strength and creep behaviour.
  - Disadvantages: It may have limitations in representing complex time-dependent behaviour.
  - Applications: Commonly used in tunnel engineering for soft rock mass analysis (Chen et al., 2021).

2.4.1 Mohr-Coulomb with Strain Softening

The Mohr-Coulomb with strain softening model is a widely employed tool in geotechnical engineering for simulating progressive failure in rock and soil slopes, which is crucial for assessing slope stability. By incorporating strain-softening to represent material softening post-peak stress, it aids in evaluating post-peak behaviour effectively (Colom et al., 2014; Rajmeny et al., 2016; Yerro et al., 2015; Molladavoodi & RahimiRezaei, 2018; Ahmed & Hawlader, 2016). This model's advantages include its capability to simulate material brittleness, align with observations in mines, and describe mobilised rock mass brittleness (Colom et al., 2014; Rajmeny et al., 2016; Yerro et al., 2015). It also considers mean effective stress and relative density effects on stress-softening behaviour in dense sand (Ahmed & Hawlader, 2016).

However, limitations exist. Its simplification of post-peak behaviour into a four-line model may not fully capture material complexities, and its conservative predictions in plane strain scenarios could restrict its applicability (Wang et al., 2012; Tschuchnigg et al., 2019).

In slope stability analysis, this model finds diverse applications across various domains, including mines, deep-seated landslides, tunnels, lateral pipeline-soil interactions, compaction grouting pressure simulation, and modelling ground reaction curves for deep circular tunnels (Rajmeny et al., 2016; Yerro et al., 2015; Chen et al., 2022; Roy et al., 2016; Tschuchnigg et al., 2019; Yang & Zou, 2009; Zareifard, 2020).

2.5 Assessing Progressive Failure in Slopes

Assessing progressive failure in rock slopes is vital in geotechnical engineering, demanding diverse numerical and analytical methods to capture complex behaviours. The Mohr-Coulomb failure criterion is a prominent approach, demonstrated by An et al. (2013) using the numerical manifold method (NMM) to simulate progressive failure in rock slopes with non-persistent joints. Similarly, Delonca et al. (2020, 2021) employed the Mohr-Coulomb criterion to simulate the cascade effect of rock bridge failure in planar rockslides. Huang et al. (2014) integrated a Mohr-Coulomb criterion-based fracturing algorithm into the NMM to simulate step-path failure in rock slopes with intermittent joints.

Dynamic loading effects and strain-softening behaviour are critical considerations. Ai et al. (2022) introduced strain-softening and vibration deterioration models to simulate seismic slope stability coupled with progressive failure, incorporating dynamic loading effects. Riva et al. (2018) simulated progressive failure in large rock slopes by considering damage-based time-dependent modelling, underlining the importance of accounting for damage accumulation.

2.5.1 Factors Affecting Assessing

Assessing progressive failure in slopes, mainly rock slopes involves considering various physical and numerical factors and limitations that significantly impact accuracy and reliability. Physical characteristics like material properties, geological conditions, and dynamic loading effects are crucial determinants of slope stability and failure mechanisms (Zhang et al., 2013; Bowa & Gong, 2021; Park et al., 2021).

Numerical considerations, including model parameters, mesh discretisation, solution domain size, and computational challenges, are equally important (Richer et al., 2020; Lu et al., 2020; Gao et al., 2016; Locat et al., 2013; Tu et al., 2021). These factors influence the reliability and accuracy of numerical assessments of progressive failure.

2.5.2 Back-Analysis Technique

Back-analysis technique in slope stability, with probabilistic and three-dimensional analysis, offer valuable approaches for refining model parameters and estimating in situ strength. These techniques contribute to a comprehensive understanding of slope behaviour and help capture implicit parameters, enhancing the accuracy of stability assessments (Zhang et al., 2010; Griffiths & Marquez, 2007). While probabilistic back-analysis methods explicitly consider uncertainties, three-dimensional analysis techniques provide insights into complex slope geometry and material behaviour. Additionally, metaheuristic algorithms and traditional kinematic analysis methods play roles in assessing slope stability, offering innovative solutions and valuable insights (Haghshenas et al., 2021; Bakhtiyari et al., 2017). Despite their advantages, back-analysis techniques require careful consideration of failure initiation mechanisms and computational complexities, highlighting the importance of understanding the causes of failure and selecting appropriate methods (Wei et al., 2019; Bouajaj et al., 2016). These diverse methodologies collectively contribute to a more accurate and reliable slope stability assessment, particularly in the context of progressive failure in rock slopes.

2.5.3 Numerical Modelling

Numerical modelling methods are vital in assessing progressive failure in rock slopes, offering diverse approaches tailored to capture complex rock mass behaviour and failure mechanisms. FLAC3D provides insights into the influence of features such as a joint inclination on slope stability but may not fully capture the complexity of failure mechanisms (Wu et al., 2012). Similarly, the distinct element method (UDEC-ITASCA) offers a detailed understanding of rock block stability on inclined joints but may struggle with simulating large-scale failure mechanisms (Delonca et al., 2020).

Hybrid continuum and discontinum techniques provide a comprehensive approach to model progressive failure, although their complexity and computational demands can be challenging (Nishimura et al., 2010). Finite element limit analysis (FELA) offers robust estimation of critical seismic coefficients for rock slopes, yet computational demands and mesh distortion issues may limit its applicability (Meng et al., 2021). DEM and FDM offer insights into sublevel caving mining-induced slope instability but face challenges with computational expense and mesh distortion (Tu et al., 2021).

Thermo-mechanical coupled models allow a comprehensive assessment of degrading permafrost rock slopes, considering warming-and-thawing-dependent deformation, but their implementation complexity and computational demands pose challenges (Mamot et al., 2020). In summary, while numerical modelling methods offer valuable insights into rock slope stability, their suitability for specific applications must be carefully considered, given their advantages and limitations.

2.5.3.1 Finite Differences Method

The finite difference method (FDM) implemented in FLAC3D is a numerical technique utilised for solving differential equations through approximations with difference equations (Kaczmarzyk et al., 2018). FLAC3D leverages FDM to adjust polyhedron elements in three-dimensional meshes to fit the structure, making it applicable to various geotechnical engineering challenges (Wu et al., 2021).

FLAC3D has been employed in slope stability to create 3D finite difference models using the strength reduction method to analyse rock slope stability and deformation processes (Zhan et al., 2019; Wu et al., 2023). Furthermore, it has been utilised to evaluate the stability of offshore artificial islands, providing insights into foundation settlement and wall deformation during construction (Hou et al., 2016). Additionally, FLAC3D has been instrumental in assessing underground space stability and sensitivity to in situ stress uncertainties (Gong, 2021).

Regarding pile foundations, FLAC3D has contributed to seismic performance analyses, including lateral spreading induced by liquefaction and seismic loading (Gowda et al., 2022; Kong et al., 2019; Luan et al., 2015). It has also been employed to study pile group seismic responses, soil-structure interaction, and novel retaining system behaviours (Kong et al., 2019; Zhang et al., 2020; Tian et al., 2016).

However, FLAC3D's applicability has limitations. It requires careful parameter selection and consideration of material properties, and the computational demand for 3D modelling can be substantial (Ye et al., 2005). To enhance analyses, integrating advanced material models, reliability analysis techniques, and dynamic loading considerations can further improve FLAC3D's efficacy (Yan-hui et al., 2022; Wang et al., 2018; Ai et al., 2022).

2.5.3.2 Explicit Finite Volume Method

The Explicit Finite Volume Method (EFVM) is a numerical approach for solving partial differential equations (PDEs) by discretising the domain into control volumes, implemented in FLAC3D to handle irregular geometries effectively (Krivá & Mikula, 2002; Castro et al., 2018). Unlike finite differences, EFVM conserves quantities within control volumes, making it suitable for systems like rock slopes with non-persistent joints (Papanikos & Gousidou-Koutita, 2015). Although it accurately conserves physical quantities, it may demand higher computational resources due to solving equations within each volume (Papanikos & Gousidou-Koutita, 2015).

EFVM finds applications in various fields, including geomechanics, for understanding progressive failure in rock slopes, capturing complex geometries and material properties for reliable predictions (An et al., 2013). Compared to Finite Element Method (FEM), EFVM offers advantages in handling irregular geometries and complex boundary conditions in geotechnical applications (Busto et al., 2021). FEM excels in analysing stress and deformation but may struggle with certain discontinuities and geometries, while finite differences face limitations with irregular geometries (Keilegavlen & Nordbotten, 2017).

In conclusion, EFVM's effectiveness lies in handling irregular geometries effectively, making it valuable for modelling complex systems like rock slopes. The choice between EFVM, FEM, and finite differences should align with problem characteristics to ensure suitability and effectiveness in geotechnical applications.

2.6 Porphyry Deposits

Porphyry deposits, significant for metals like copper, molybdenum, and gold, result from metal-rich fluid interaction with rocks during magmatic activity, primarily near convergent plate boundaries (Sillitoe, 2010). Porphyry copper deposits, a common type, feature disseminated ore minerals within stockwork fractures (Bewick et al., 2022). Factors such as tectonic setting, magma composition, and oxidation state influence their formation, along with the timing of magmatic events and crustal structural controls (Lopes & Moura, 2019).

2.6.1 Porphyry Deposits Alteration Types

Porphyry deposits exhibit various alteration types, providing valuable insights into mineralisation processes and geotechnical characteristics. Two common types are propylitic and argillic alterations, often accompanied by silicification and advanced argillic alteration (Sillitoe, 1973). Other alterations include potassic, phyllic, sericitic, and carbonate (Schmidt, 1985).

- **Propylitic Alteration:** Characterized by chlorite and carbonate replacement of primary minerals, typical in low-temperature, low-sulfidation environments, impacting rock strength and stability (Sillitoe, 1973).

- **Argillic Alteration:** Involves clay mineral formation like kaolinite and illite due to acidic, high-temperature conditions, affecting rock permeability and mechanical properties (Sillitoe, 1973).

- **Potassic Alteration:** The presence of potassium-rich minerals like biotite, associated with high-temperature conditions, influencing rock strength (He et al., 2021).

- **Phyllic Alteration:** Characterized by sericite and pyrophyllite replacement, indicative of moderate temperatures and acidic conditions, impacting rock permeability and deformation behaviour (Becker et al., 2008).

- **Sericitic Alteration:** The presence of fine-grained sericite from feldspar alteration, associated with lower temperatures, affecting mechanical properties (Chen et al., 2019).

- **Carbonate Alteration:** Involves carbonate mineral replacement, affecting acid-rock drainage potential and geochemical behaviour (Yu et al., 2017).

2.6.2 Materials Geomechanical Properties

Weathering and alterations significantly impact rock properties, often resulting in decreased mechanical strength but occasionally enhancing specific characteristics. Research consistently shows a decline in properties like uniaxial compressive strength (UCS) with increased alteration degree (Rupar et al., 2021; Flandes, 2023). However, alterations can also improve certain properties; for example, porosity reduction and mineral elasticity alteration may increase wave speeds in volcaniclastic rocks (Durán et al., 2019).

Typical altered rock properties vary based on alteration type and rock composition. In the Kuril–Kamchatka Island arc, compressive strength ranged from 999.68 to 2469.10 kg/cm^2, and abrasion resistance ranged from 29.67 to 54.64 Ha (Frolova et al., 2014). Dacite rocks exhibited exponentially decreasing UCS with increased alteration degree (Rupar et al., 2021). Alterations in volcaniclastic rocks led to significant wave speed variations, indicating mechanical property changes (Durán et al., 2019). Short wavelength infrared spectral curves identified altered rocks with UCS ranging between 100–150 MPa in specific wavelength ranges (Pan et al., 2022).

Chapter 3

Numerical modelling of progressive failure due to mine sequencing of a deep open pit slope: Importance of the geotechnical model in validating against a back-analysis

3.1 Contributions made to this Chapter:

The M.Sc. Recipient carried out the work presented in this chapter, which includes a literature review, data collection, methodology, analysis, discussion of results, and writing of the text.

Dr. Renato Macciotta reviewed all parts of the work and guided the development of the methodology and its application. The other authors reviewed the text and provided edits and additional discussion recommendations.
A version of this Chapter is being prepared for submission to the Engineering Geology journal with the following citation:

Puerta-Mejía, A.F., Deisman, N., Macciotta, R., O'Neil, S., and Eberhardt, E. 2024. Numerical modelling of progressive failure due to mine sequencing of a deep open pit slope: Importance of the geotechnical model in validating against a back-analysis.

University of Alberta Geotechnical Centre [Unpublished].

3.2 Abstract

The progressive failure of rock slopes significantly impacts the stability of deep open-pit mining operations, particularly large multi-bench failures that are not purely structurally controlled. This paper aims to give insights into the impact of different levels of detail in the geotechnical model, comprising the geology and rock mass behaviour, on the simulation of large-scale progressive slope failure in a deep open pit (over 500 meters depth according to Li et al., 2022). This was completed by systematically varying the level of detail and complexity in the geotechnical model. Validation was carried out using a back analysis of a significant deep open pit slope failure, testing the sensitivity of the results against the mining sequence, which included a pushback of the wall adjacent to the failure and the range of variability encompassed in the geotechnical model. The latter included a comparative analysis of model results assuming homogeneous elastic behaviour and increasing complexity involving varying lithology with hydrothermal alteration and Mohr-Coulomb with strain-softening behaviour. The results were evaluated against displacement data from a geodetic monitoring point within the boundaries of the failed mass and satellite images to help determine the approximate initiation of the failure. Plots of displacements, stresses, plastic shear and volumetric strains gave valuable insight to infer the influence of the geotechnical model and suggested procedures on how to best model progressive failure in deep open pit slopes.

Keywords: Deep open pit slope failure, progressive failure, rock slope engineering, geotechnical model, rock mass behaviour, numerical modelling, porphyry deposits.

3.3 Introduction

As open-pit mining operations implement designs and pushbacks resulting in slope heights exceeding 500 m, understanding progressive failure mechanisms in rock slope stability becomes increasingly important. At these slope heights, the failure mode is less likely to be structurally controlled and more likely to develop through internal shearing of the rock mass and progressive failure. Eberhardt et al. (2004) describe progressive failure as the weakening and strength degradation accompanying the slope's response to incremental stress increases. These stress increases promote localised slip along non-persistent fractures and shearing of the rock mass that, in turn, gradually weakens the rock slope, leading to its progressive failure.

The relationship between stress changes and deformation responses, for example, the increases in pit slope displacement seen with the mining of each bench, can be used to calibrate a numerical model through back-analysis (Eberhardt et al., 2017). This allows the rock mass properties and constitutive behaviour to be inferred by matching the model outputs to observed deformations and failure, thus providing a powerful tool for design. However, accurate representation of progressive failure necessitates, among others, careful consideration of the geotechnical model and its level of detail and complexity (Stead et al., 2006).

The risks associated with progressive failure in rock slopes have been highlighted by failures experienced at the Afton mine in British Columbia, the Jeffrey Mine in Quebec, and the Chuquicamata mine in Chile (Sjöberg, 1996). Other notable examples include the 2013 Manefay slide at the Bingham Canyon mine (Ward, 2015), the deadly 2020 slide at the Carmen Copper mine in the Philippines (Petley, 2020b), the 2014 Mina Pecket slide in Chile (Petley, 2014), and the 1997 Betze-Post

Mine in the USA (Rose & Hungr, 2007). These incidents highlight the significance of identifying and accurately simulating progressive failure to reduce such risks.

Despite the many advances in geotechnical analyses and monitoring technologies (Mayne, 2015), mining operations worldwide are still prone to suffering large debilitating open pit slope failures (Froude & Petley, 2018). Therefore, by gaining more insight into the factors that affect progressive failure, modelling can lead to stability optimisation of the open pits and a safer and more profitable operation (Macciotta et al., 2020).

The effects of uncertainty and oversimplification in the geological model and corresponding rock mass characterisation and behaviour models, together comprising the geotechnical model, are critically important in the numerical modelling of rock slope stability, but their full effects are poorly understood. Existing research efforts have primarily focused on qualitatively demonstrating the importance of a well-defined geological model or emphasising the selection of appropriate constitutive behaviour models (e.g., Sakurai, 2017; Sazzad et al., 2015; Hoek et al., 2001; Brown, 2008).

This paper presents a methodology that provides insights into the effects of various geological modelling levels of detail and material behaviour complexity on the numerical modelling of progressive failure at a large scale for deep open pit slopes (over 500 meters depth, according to Li et al., 2022). An inter-ramp failure in a deep open pit copper mine is used for validation purposes, and the study further illustrates recommended methods for rock slopes in geologic environments consistent with those of the case study (e.g., porphyry deposits, intrusives, hydrothermal alteration, etc.). The analysis employs an equivalent continuum treatment of the rock mass using Itasca's FLAC3D software, which is suitable for simulating progressive failure (Itasca Consulting Group, Inc., 2019).

3.4 Case Study

The case study corresponds to a deep open pit slope (over 500 meters depth according to Li et al., 2022) that experienced an inter-ramp progressive failure, with a maximum extent of 3.9 km long, 2.7 km wide and 645 m deep, according to the MEC Mining (2022) and BHP (2012). This developed through a mining sequence that saw extraction proceed in a northwest direction, including a large pushback of the north wall adjacent to where the failure eventually developed. The initiation of the failure, which developed in the northeast sector of the pit, was first observed in 2007 and evolved as benching and mine excavation progressed. A panoramic plan view of the failure status in 2019, along with project location and cross-section views with excavation sequencing, are shown in Figure 3-1 and Figure 3-2.

Figure 3-1. Plan view of the open pit case study (modified from Google Earth, 2019). The failure appears as the disturbed area in the northeast corner of the pit, with the longitudinal section line A-A passing through the slide and the transversal section line B-B crossing the toe of the failed zone. The corresponding profiles are provided in Figure 3-2.

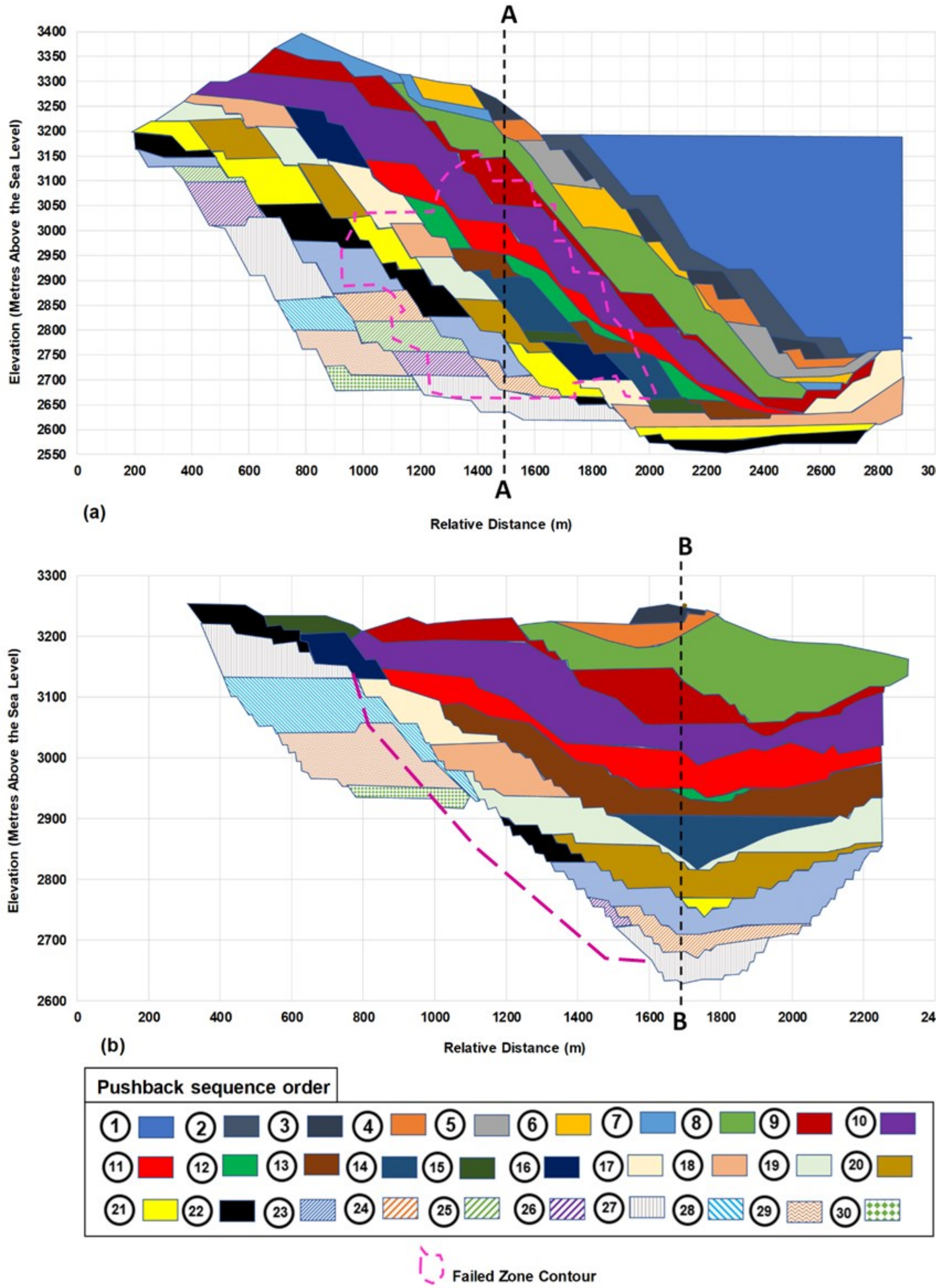

Figure 3-2. Mining and open-pit pushback sequence, shown for (a) Profile B-B (see Figure 3-1), which crosses NW-SE through the pit and provides a section through the pushback in the NW wall. The outline of the failed zone projected onto the NE wall is shown as a pink dashed line. (b) Cross profile A-A, provides a longitudinal section through the NE wall where the failed zone developed, as shown in Figure 3-1.

3.5 Geological Setting

The mine geology consists of igneous bodies in a subducting tectonic plate environment, where magma ascends and intrudes into older rocks. High pressure, temperature and the circulation of hydrothermal fluids have produced varying degrees of alteration, affecting the rock mass properties and controlling their strength behaviour.

3.5.1 Lithology

The on-site lithologies include Paleocene andesite (An), Palaeozoic andesite (PZ), quartz monzonitic-granodioritic-porphyritic stock (Stockwork, ES), and an intrusive body of Rhyolite (Rh). The stock has an elliptical shape with a maximum axis of 4.5 km long towards N 30^o-40^o W and a minimum axis of 2.5 km. The earliest intrusion phases comprise porphyritic rocks with similar characteristics, including phenocryst, vein continuity, and alteration intensity. The on-site rhyolite has a high content of quartz phenocrysts and altered feldspar phenocrysts (Hervé et al., 2012; Garza et al., 2001). Figure 3-3 (a) presents an isometric and cross-section view of the lithology.

3.5.2 Rock Mass Alterations

Hydrothermal alterations significantly impact the rocks' geomechanical characterisation. Argillitic (Ar), sericitic-chloritic (Ser-Chl), propylitic, quartzite-sericitic, quarzitic-sericitic, and potassic hydrothermal alteration types are present at the open-pit site. Andesite, rhyolite, and porphyry stock are all affected by argillitic alteration. Propylitic alteration has veins and veinlets with pyrite, chlorite, and common epidote. In intrusive rocks, quartzitic-sericitic alteration involves sulphides like chalcopyrite, pyrite, and molybdenite and is more active along fault zones. Alteration names and terminology follow Garza et al. (2001). Hydrothermal alterations are crucial to comprehend rock behaviour and geomechanical properties. Rimmelin and Vallejos (2020), after Hoek et al. (2000), present an example of the variation in intact rock strength and rock mass quality at the site, with lower strength values and decreased rock mass quality for the argillic alterations. Figure 3-3 (b) shows the previous alterations distributed across the open pit and specific to the failed area.

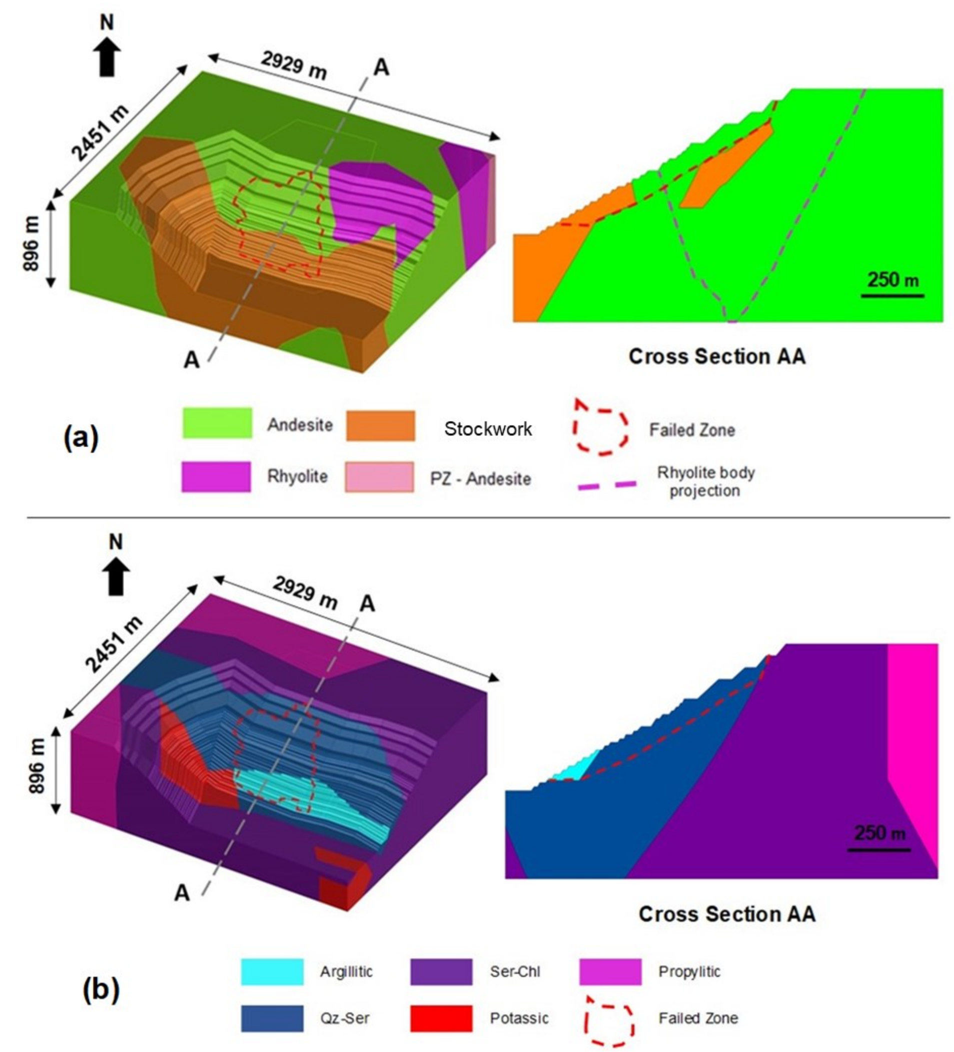

Figure 3-3. Site geology, including isometric and sectional views along A-A (see Figure 3-1), showing the distribution of (a) lithologies and (b) alteration types, as mapped in the open pit with the outline of the failed area shown by the dashed red line. (Data derived from Garza et al., 2001; model built using Rhinoceros 3D, V. 7.0., McNeel, R., & others., 2020).

3.5.3 Major Structural Features

The main fault systems in the pit are oriented N-S, NE-SW, and NW-SE. The oldest fault system is part of the longest and most important regional fault system (N-S) (Riveros et al., 2014). In contrast, the NE-SW faults are tensional structures and were responsible for the NW-SE fault vertical movement. The youngest system is related to the argillitic alteration advance and mineralisation emplacement process at the mine site. Variable infilling materials seal the N-S system. The NE-SW set comprises continuous faults with a thickness of 0.3 metres and fractured zones infilled with fault gouge. The NW-SE system is characterised by continuous wavy surfaces, with infill such as fractured rock, fault gouge, quartz-sericite, and other materials from high argillic alteration (Garza et al., 2001). Table 3-1 presents the major fault system characteristics.

Table 3-1. Major faults in the mine zone and its characteristics. (Data provided by the mine's operator, 2021).

System	Relative Age	Type	Mineralisation	Profile	Dip	Strike	Main Infillings	Persistence	Thickness
N-S	Oldest	Strike	Yes	wavy	70W - 78E	N20W - N20E	Fractured rock or gouge	about 1 km	0.5 m
NW-SE	Post-NS	Strike	Yes	wavy	65S - 70N	N40-75W	Gouge	about 1 km	< 2m
NE-SW	Youngest	Normal	No	-	60 - 70 S	N60-75E	Fractured clay gouge	greater than 2 km	0.5 m

3.6 In-Situ Stresses

The tectonic regime corresponds to a compressive environment typical of the Andes in Chile with, generally, higher stresses in the East-West direction. Galarce (2014) and Garza et al. (2001) have provided significant initiatives to characterise the in-situ stress state at the mine site, constrained by stress measurements on mining and civil tunnelling projects throughout Chile. These indicate that the horizontal to vertical stress ratio K, for the mine's depth range of about 550 metres, is expected to be greater than one. This study adopts a K value of 1.2.

3.7 Water Conditions

The pit has a thorough dewatering system, including drainage tunnels, horizontal drains, and pumping wells, which has maintained a relatively consistent water table level before and during the failure's development. According to the closest piezometer to the failed zone (a vibrating wire piezometer), the water table fluctuates between the 2750 and 2780 levels, which are below the failure surface. Therefore, pore pressures were not considered in the slope modelling.

3.8 Materials Parameter and Geotechnical Model

The initial material parameters were defined based on work by Rapiman and Sepulveda (2006) and Valdivia and Lorig (2001) from a project nearby. Missing parameters were taken from similar lithologies and geological conditions (Rimmelin & Vallejos, 2020; Lorig & Varona, 2013). Table 3-2 shows the average and standard deviation of strength and deformation parameters. Ranking the dominant lithologies from the most competent in strength and stiffness to the weakest and most deformable, these are the: Rhyolite, Stockwork, and Andesite. Correspondingly, a similar ranking of the alterations would be Potassic (K-Bt), Propylitic, Ser-Chl, Qz-Ser, and Argillic.

The FLAC3D model that incorporates these zones is shown in Figure 3-4 and the associated input strength properties are included in Table 3-2.

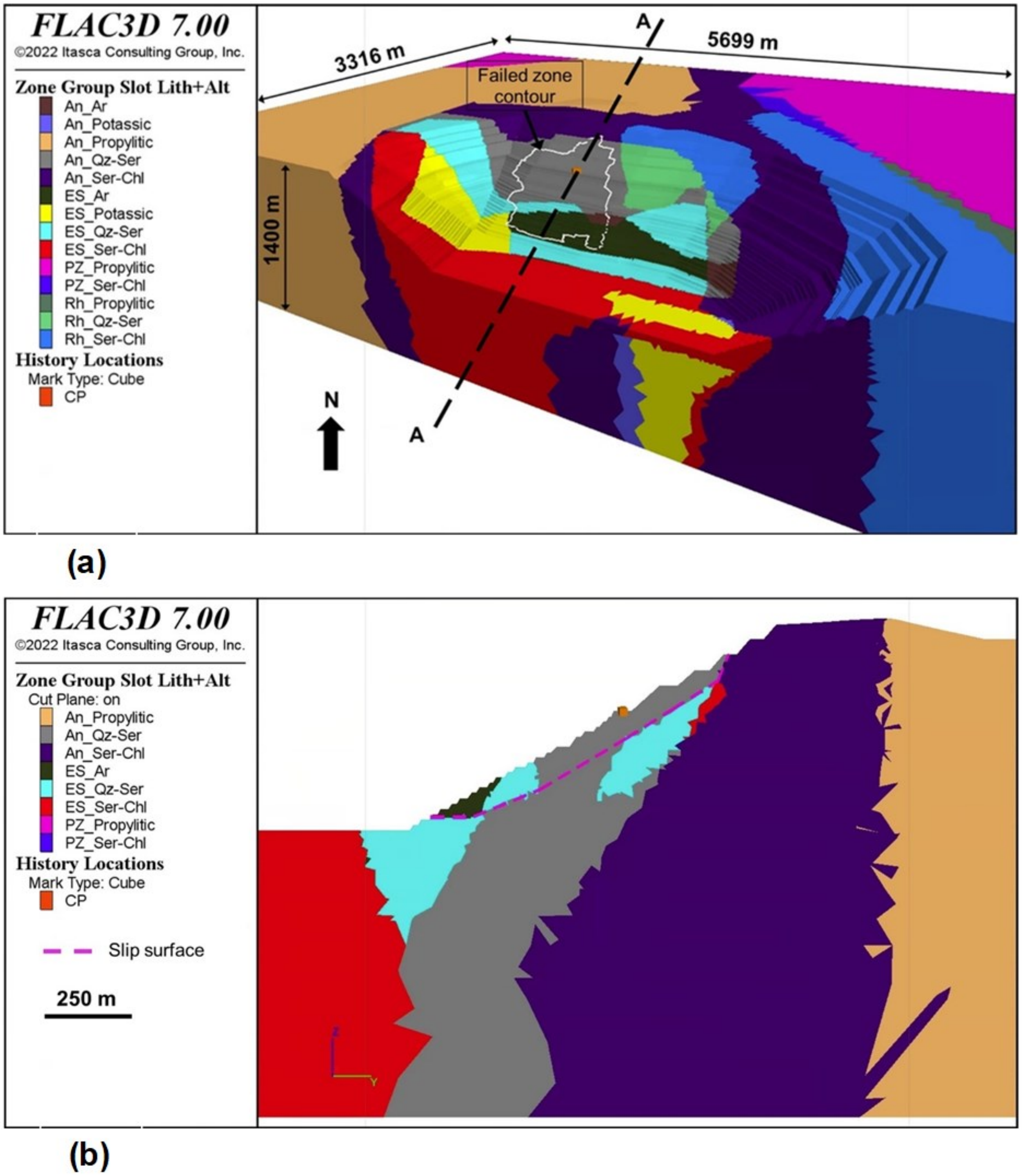

Figure 3-4. Geotechnical model showing the distribution of lithological and hydrothermal alteration units built into the numerical model and their relationship to the outline of the failed zone location, as seen in (a) isometrical view, and (b) along profile A-A. Model built using FLAC3D V. 7.0., Itasca Consulting Group, Inc. (2019).

Table 3-2. Geomechanical parameters compiled for the key rock mass domains in the modelled area of the mine, according to their lithology and alteration type.

	γ (kN/m³)		$\phi_{(P)}$ (o)		c (kPa)		ψ (o)		E_{rm} (GPa)		ν_{rm}		ε_crit	
	Avg.	StdDev.	Avg.	StdDev.	Avg.	StdDev.	Avg.	StdDev.	Avg.	StdDev.	Avg.	StdDev.	Avg.	StdDev.
Andesite														
Argillic	21	0	34	4	439	97	16	5	4.2	4.6	0.27	0.01	8E-02	1E-02
K-Bt	25	0	38	2	537	32	23	2	12.6	5.3	0.24	0.01	6E-02	7E-03
Qz-Ser	25	0	40	4	535	113	23	3	9.9	3.9	0.24	0.01	6E-02	7E-03
Ser-Chl	25	-	30	-	435	-	15	-	4	-	0.26	-	7E-02	-
Escondida Stock														
Argillic	21.3	1.3	39	10	394	244	20	4	3.6	0.8	0.26	0	7E-02	3E-03
Propylitic	25	-	38	-	526	-	20	-	6.1	-	0.25	-	7E-02	-
K-Bt	25.3	0.5	38	6	483	143	22	4	11.4	6.9	0.24	0.01	6E-02	9E-03
Qz-Ser	25	0.1	39	4	506	143	23	3	10.6	7	0.24	0.01	6E-02	7E-03
Ser-Chl	25	0	41	2	529	67	20	2	4.6	1.5	0.26	0.01	7E-02	5E-03
Rhyolite														
Argillic	21.3	-	43	-	1287	-	23	-	6.1	-	0.25	-	7E-02	-
Propylitic	25	-	45	-	689	-	26	-	9.8	-	0.24	-	6E-02	-
K-Bt	26	-	37	-	840	-	21	-	9.5	-	0.25	-	6E-02	-
Qz-Ser	24.9	0.1	43	4	592	98	27	3	14.7	6.1	0.24	0.01	6E-02	8E-03
Ser-Chl	25	-	45	-	689	-	26	-	9.8	-	0.24	-	6E-02	-

γ: Unit weight, $\phi_{(P)}$: Peak friction angle, **c**: Peak cohesion, ψ: Dilation angle
E_{rm}: Rock mass deformation modulus, ν_{rm}: Poisson ratio, **ε_crit**: critical plastic strain (plastic shear strain at which the strength transitions from peak to residual values).

3.9 Case Study Progressive Failure Event

Phase excavations and benching of the open pit have followed a NW direction that coincides with the longitudinal axis of the pit (see Figure 3-1). This includes a pushback of the NW wall for pit deepening that resulted in a vertical and lateral deconfinement of the NE wall (see Figure 3-2). From the beginning of the operation, the NE wall was identified as marginally unstable at the multi-bench scale. Large deformations and slow velocities have been detected and measured as smaller acceleration events as the failure has developed. It is noted that although the affected zone in the NE wall had already been deconfined since 2002, the first noticeable inter-bench cracks were not observed until 2007.

Displacement measurements for a prism located in the yielding mass (referred to herein as monitoring point "CP") are available between 2011 and 2017. Unfortunately, there was no data available for the earlier periods of slope initiation and movement (i.e., 2007-2011). Therefore, displacement estimates based on satellite imagery from Google Earth were used to complement the displacement record. For these estimates, the satellite images were all fixed to the same latitude and longitude ranges and eye-level altitude. On each image, approximately near and around the placed prism (CP), the horizontal separation between one of the failed bench edges and its undisturbed position was measured, as demonstrated in Figure 3-5.

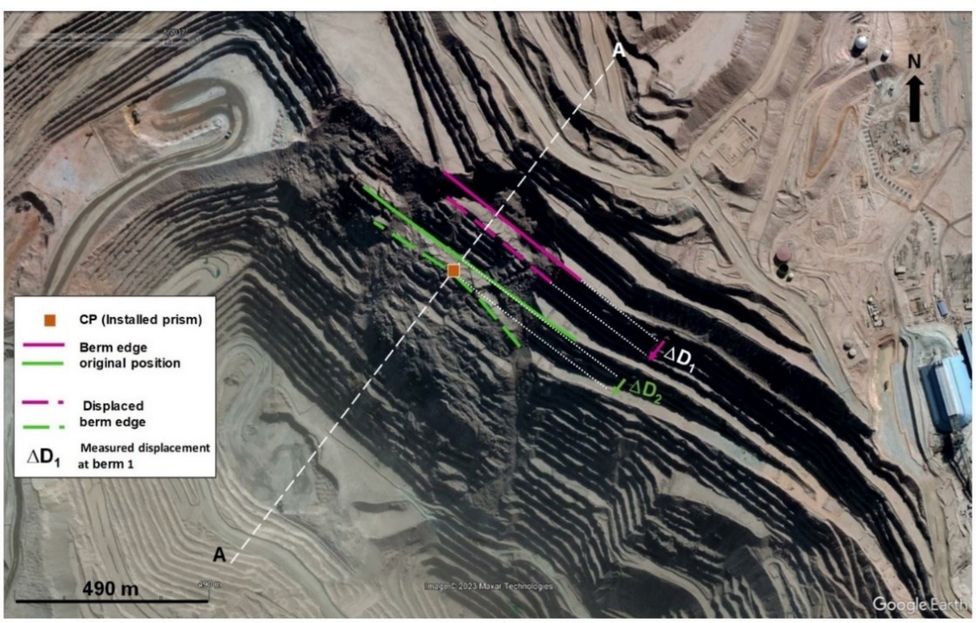

Figure 3-5. General procedure for obtaining displacement estimates for the period between the initiation of slope movements and 2017, when geodetic monitoring of the slope began. (Modified from Google Earth, 2017).

As a result, Figure 3-6 shows the history displacement plot with the site's images depicting the crack extension progress and prism location. This shows how the failure evolved from an initial inter-bench to a fully inter-ramp failure. The blue line is the displacement estimate, and the red line is the measured values based on the mine's monitoring system. The red dashed line depicts the measured data shifted upwards to start from the trend derived from the satellite image analysis based on the slope's previous movement history. The continuous blue and dashed red lines provide upper and lower bounds, respectively, for the numerical model calibration.

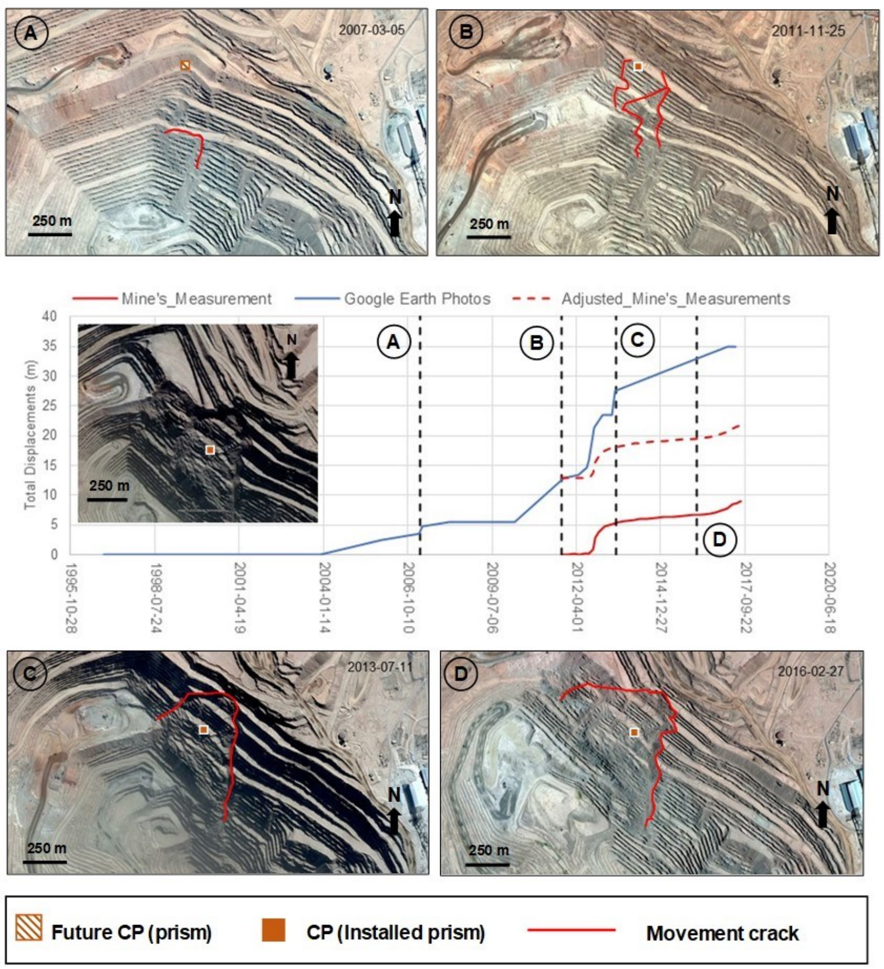

Figure 3-6. Cumulative displacement plot of a tracking point (CP) located on the failed mass and corresponding trend derived from satellite imagery. Also shown are images outlining the evolution of cracking coinciding with the boundary of the unstable area.
(Geodetic data provided by the mine's operator, 2021; imagery modified from Google Earth, 2007, 2011, 2013, 2016).

The history displacement plot depicts the complete movement kinematics, showing four (4) movement phases. Using the definitions of Broadbent and Zavodni (1982), these include a progressive phase between 2004 and 2006 (Phase A), a retrogressive phase between 2006 and 2010 (Phase B), another accelerated progressive phase up to 2013 (Phase C), and finally, a mostly deaccelerated retrogressive phase (Phase D). The failure kinematics was interpreted to be translational, with a slip surface dipping at 30 degrees and striking parallel to the slope face, and the mechanism involved rock mass shear rupture with minor sliding on structural elements. The failure's spatial attributes, such as the area extension onto the slope surface, the average depth, slip surface shape, and total length, are shown in Figure 3-7.

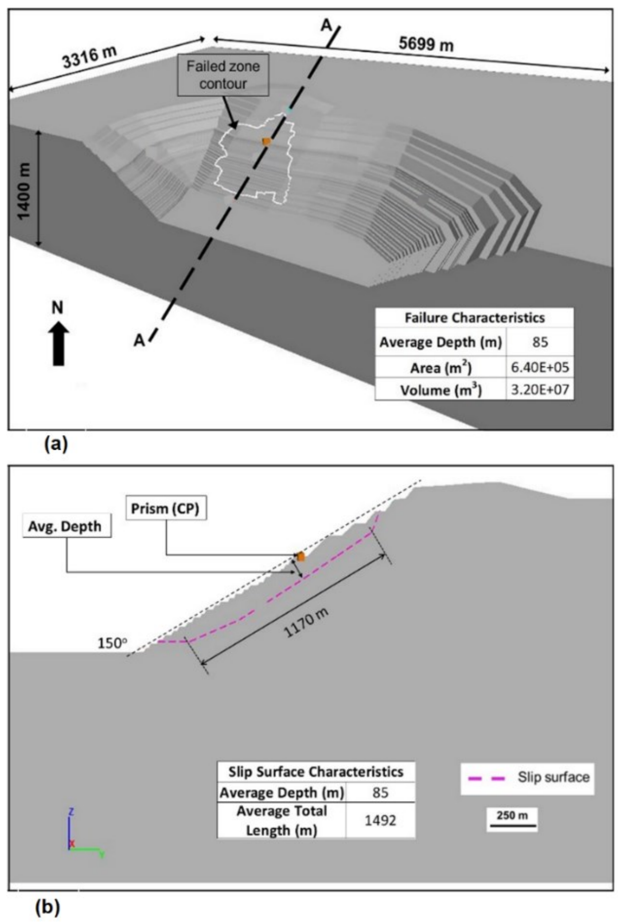

Figure 3-7. Slope failure spatial characteristics, as outlined relative to (a) an isometric view and (b) along cross-section A-A in the direction of slip movement. Model built using FLAC3D V.7.0., Itasca Consulting Group, Inc. (2019).

3.10 Modelling Process

Nine model variants were developed to assess the sensitivity and impact of varying the complexity in the geology representation and constitutive behaviour model, relative to the targeted validation against the spatial and temporal (i.e., sequencing) attributes of the pit wall failure. The geological complexity modelled considered a homogeneous domain (H), a representation with the three dominant lithology domains (G), and the inclusion of six domains that account for both lithology and hydrothermal alteration (A). The constitutive behaviour models implemented include a Linear Elastic assumption (LE), an Elastic-Perfectly Plastic assumption (EPP), and a Strain Softening treatment (SS).

The model geometry, including the geometry of the pushbacks, geology, and alterations, was built in Rhinoceros 3D V. 7.0., McNeel, R., & others. (2020), and meshed for compatibility with Itasca's FLAC3D V. 7.0., modelling software, using Griddle V. 2.0 (via Itasca's plug-in to Rhinoceros 3D), Itasca Consulting Group, Inc. (2019) and Itasca Consulting Group, Inc. (2020), respectively. The model calibration started from the input properties listed in Table 3-2. The linear elastic models were inspected for coherence in terms of stress and strains before moving on to the elastic-perfectly plastic and strain softening models, following Lees (2016). The EPP and SS models were compared against the displacement history in Figure 3-6. The modelling procedure and comparative analysis matrix comprising geological complexity and behaviour model levels are shown in Figure 3-8.

Figure 3-9 details the necessary input data, software, and operations to build a satisfactory FLAC3D model file to begin the calibration step. The calibration procedures are detailed in Figure 3-10. The latter shows how the initial elastic runs were used to verify an adequate "coherent" stress-strain behaviour was being obtained, to detect model geometry, meshing and other setup errors, and how comparing the field data to the plastic simulation results was used to calibrate the input parameters to reproduce the observed failure characteristics. A "coherent" stress-strain behaviour implies that the model shows no stress concentrations or excessive deformations. Additionally, stress distributions should align with pre-mining conditions, increasing with depth, being redistributed by the excavation sequencing, and showing deformations where material has been removed.

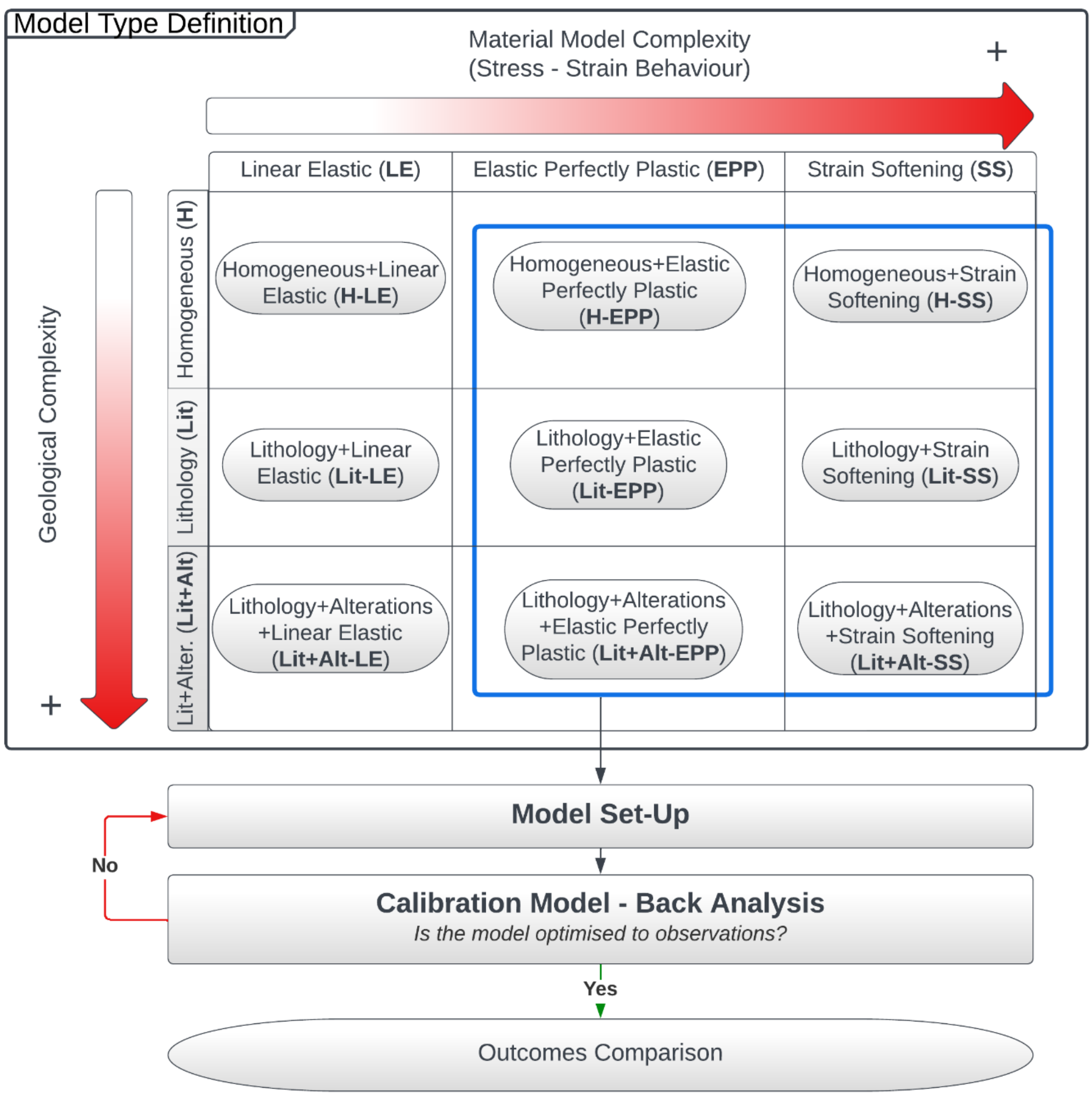

Figure 3-8. Flowchart showing the modelling procedure and consideration of geological and behaviour model complexity levels.

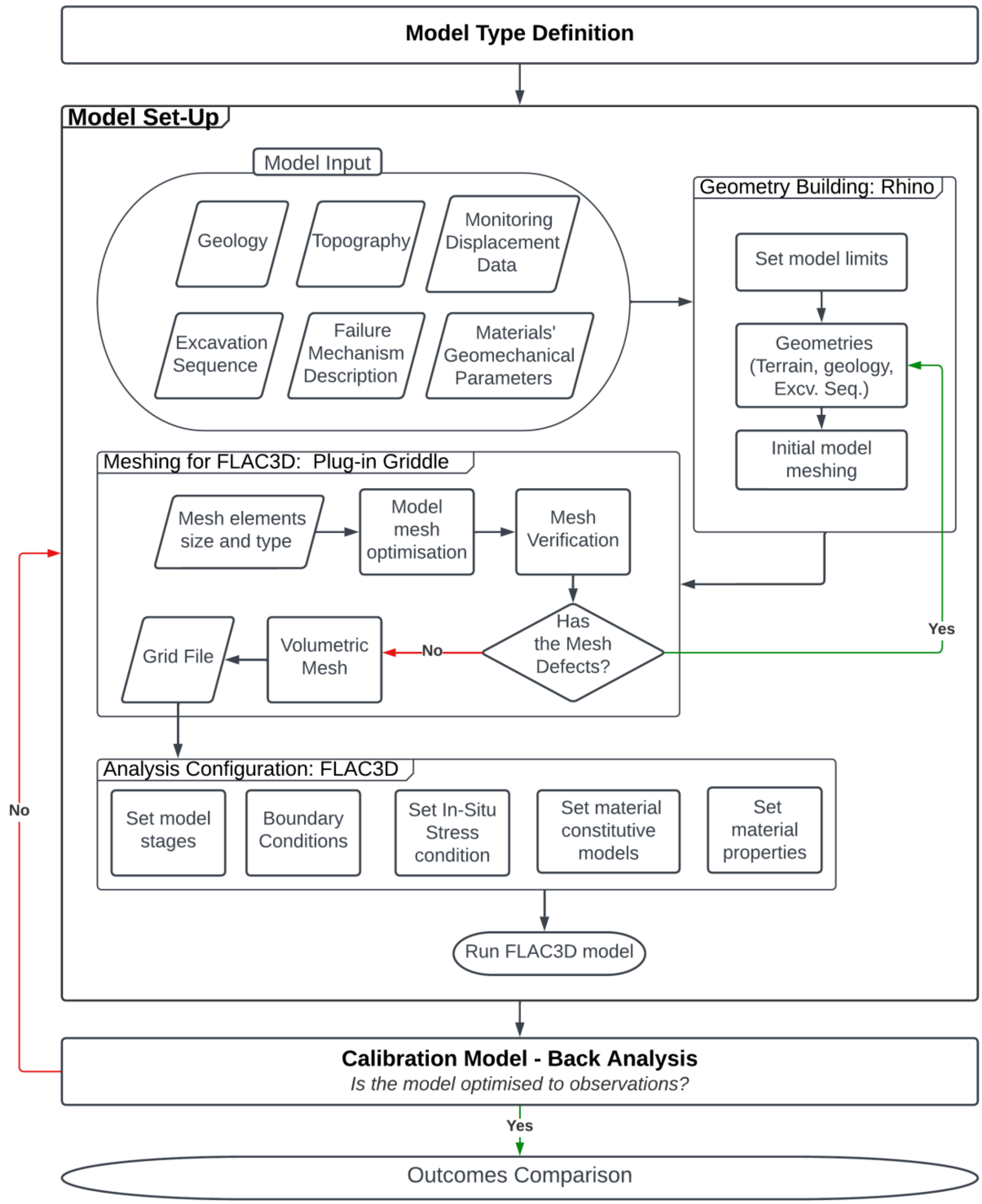

Figure 3-9. Flowchart detailing the model set-up process.

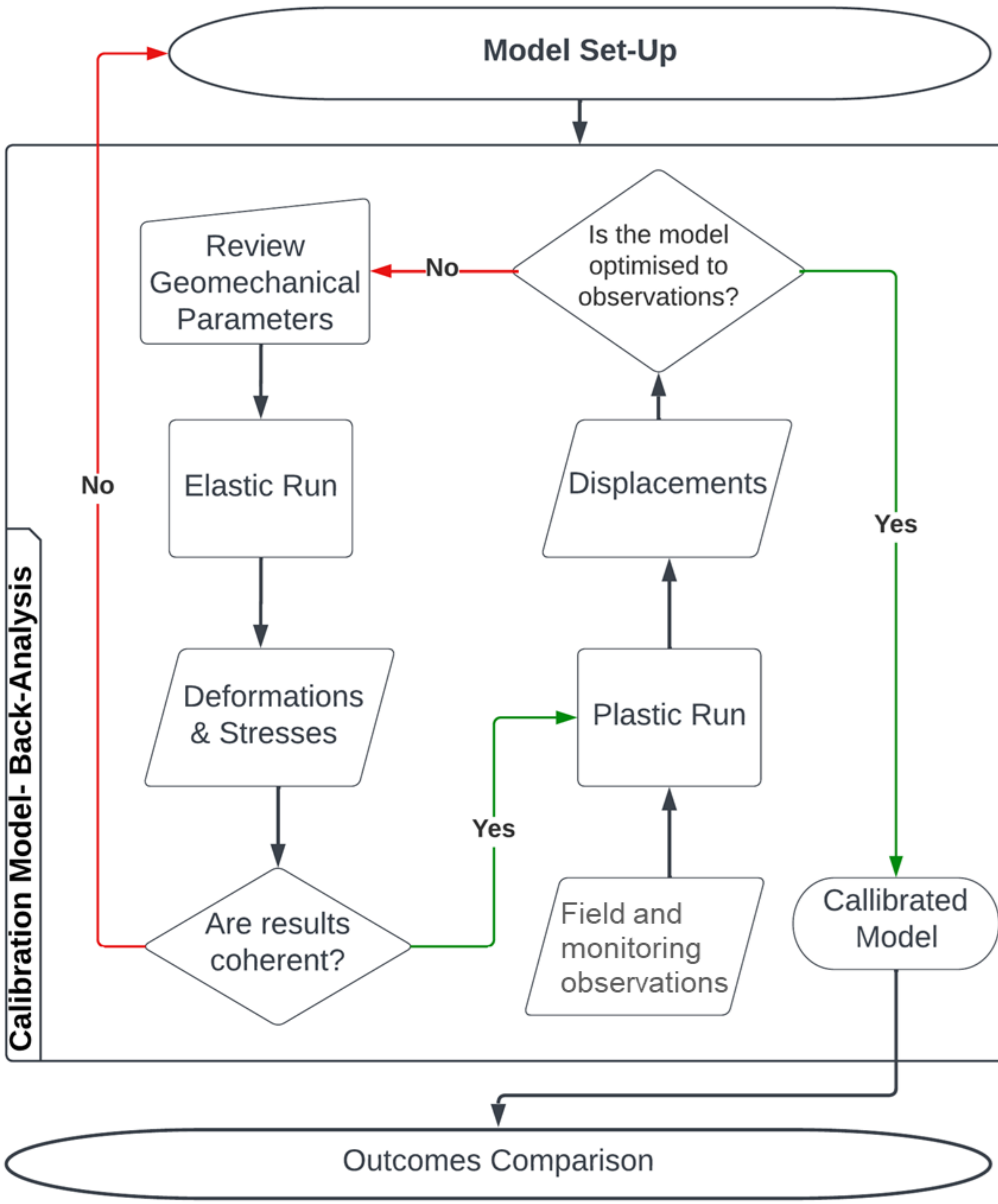

Figure 3-10. Flowchart illustrates the sub-routine followed to calibrate the models through back analysis of the case study failure.

3.10.1 Model Characteristics and Assumptions

The final model geometry and mesh are depicted in Figure 3-11 and Figure 3-12 respectively. Several important insights were gained from the model construction, testing of the mesh quality and modelling procedure developed. These, together with other key model assumptions include:

- Detailed topographical features do not significantly impact the numerical analyses. Original pre-mining terrain, open-pit, and pushback surface shapes can be simplified.
- Despite having the pit's topographic data from 1996 to 2021 (via open-pit shells), which encompass more than 30 stages in the NW pushback, we found that those in the outer regions away from the slope failure do not directly influence or prevent the reproduction of the failure mechanism. Therefore, the pushback sequences were reduced from 30 to 19 (see Figure 3-11).
- It is not necessary to represent the full detail of the actual shape of the pushback wall. Continuous slope faces without benches were used to represent the upper sections of the pushback and slope faces.
- The model's block dimensions ensure no interference between mechanical boundary conditions and pushback-induced stresses; thus, a smooth transition from disturbance by excavation sequence to the initial stress field can be observed.
- The model uses tetrahedral elements ranging in size from 100 m at the model's outer boundaries and edges to 25 m within the volume of interest (Figure 3-17). This prevents erroneous findings caused by element interlocking prevalent in coarse meshes (Lin et al., 2020; Oberhollenzer et al., 2018).
- The numerical analysis does not explicitly consider the major fault systems or discontinuities. Instead, these are treated implicitly in the assessment of the geomechanical parameters, which account for rock mass defects such as veins, veinlets, fissures, joints, and minor faults in the Mohr-Coulomb rock mass shear strength

parameters (c and ϕ).

- The rock mass deformation and strength parameters were not adjusted to account for the effects of excavation blast damage. Slope relaxation effects were accounted for explicitly in the strain-softening models. Blasting is reported to affect rock mass in extreme cases up to 55 meters behind newly created open pit mine faces (benches), according to McIntyre and Hagan (1976). The previous leads to the failure of thin slices when compared with the case study failure scale (inter ramp scale).
- The rock mass deformation modulus was assumed to be constant, independent of stress or strain.
- The pre-mining in-situ stress ratio of K = 1.2 was assumed to act uniformly across the model and with depth.
- The residual strength parameters were determined following the procedure recommended by Cai et al. (2007), who suggest a reduction in GSI between 37% and 51%. The reduced GSI value is then used to calculate the residual rock mass cohesion and friction from the residual Hoek-Brown parameters relative to the confining stress corresponding to the pit slope height, as per the procedures in Renani and Martin (2020b).
- The strain softening model used assumes a simple linear degradation of the Mohr-Coulomb strength parameters, as commonly adopted in slope stability analyses (e.g., Renani & Martin, 2020a; Mohammadi & Taiebat, 2013; Conte et al., 2010; Troncone, 2005; Potts et al., 1997). Figure 3-13 illustrates the linear degradation approach and plots an example from this work.
- A satisfactory calibration process was determined by following the criteria listed in Table 3-3.

Table 3-3. Criteria used to establish whether a model can be calibrated, with increasing level of fit.

ID	Description
C1	Either no failure or excessive displacements compared to those at timestamp (A) in Figure 3-3.
C2	The model shows a total displacement like those measured by the mine after the 2007 pushback, involving approximately 2.5 to 4.0 metres at the mid-height of the failing rock mass along Section A-A in Figure 3-1.
C3	Once movement reaches the C2 displacement amount and begins to accelerate, the outline of the maximum shear strain contours should match the depth of the slip surface as projected on section A-A and the slide area as seen in the isometric view (see Figure 3-4).

- The models were judged as reaching an equilibrium state when the mechanical ratio between the balanced and unbalanced forces in the model was between 1E-6 and 1E-4, and history graphs of the displacements, stresses, and velocities attained a constant value. This was usually accomplished after approximately 3000 cycles (see Itasca Consulting Group, Inc. 2019a, for the cycling procedure).
- The monitoring points embedded in the model (see Figure 3-14), other than to calibrate the models (using point CP), mainly served to check the displacements (points: MP-1, MP-3, MP-1E, and MP-2E), displacement rates (MP-2 and MP-4), and stress states (points: MS-1, MS-2, and MS-3) within the failed mass.

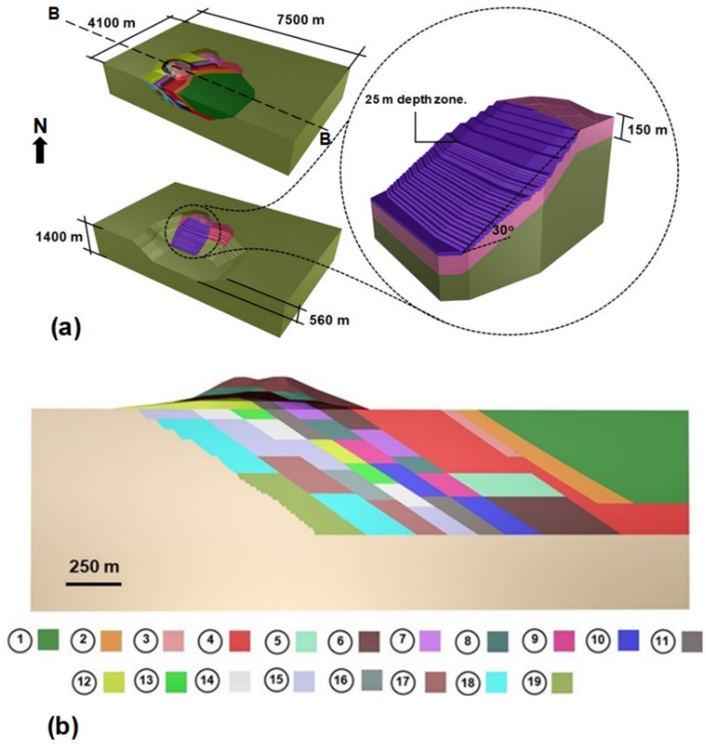

Figure 3-11. Geometric locations of the material zonation used in the model, relative to: (a) an isometric view showing the overall model size and detailing of the failed zone, and (b) section B-B with the simplified excavation sequencing.

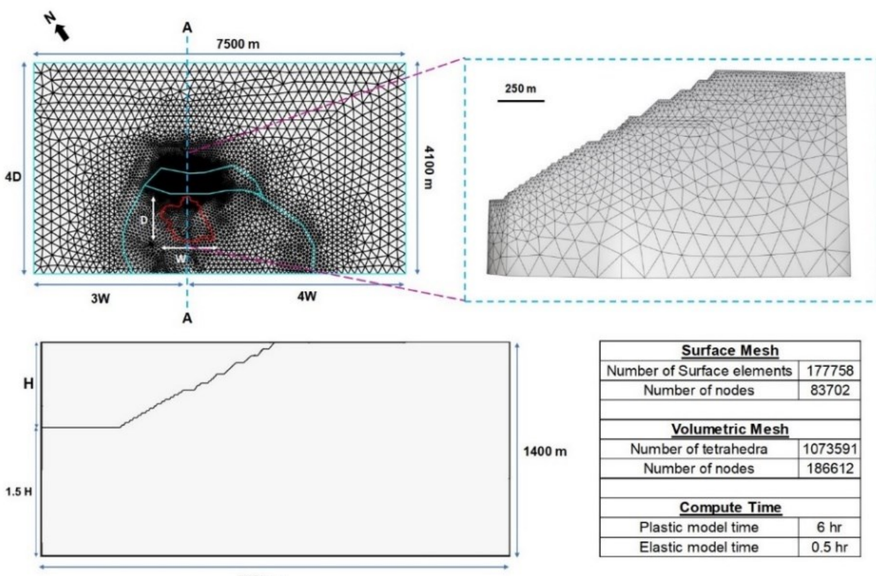

Figure 3-12. Mesh and model characteristics. Model built using Rhinoceros 3D V. 7.0., Griddle V. 2.0., McNeel, R., & others. (2020), and Itasca Consulting Group, Inc. (2020), respectively.

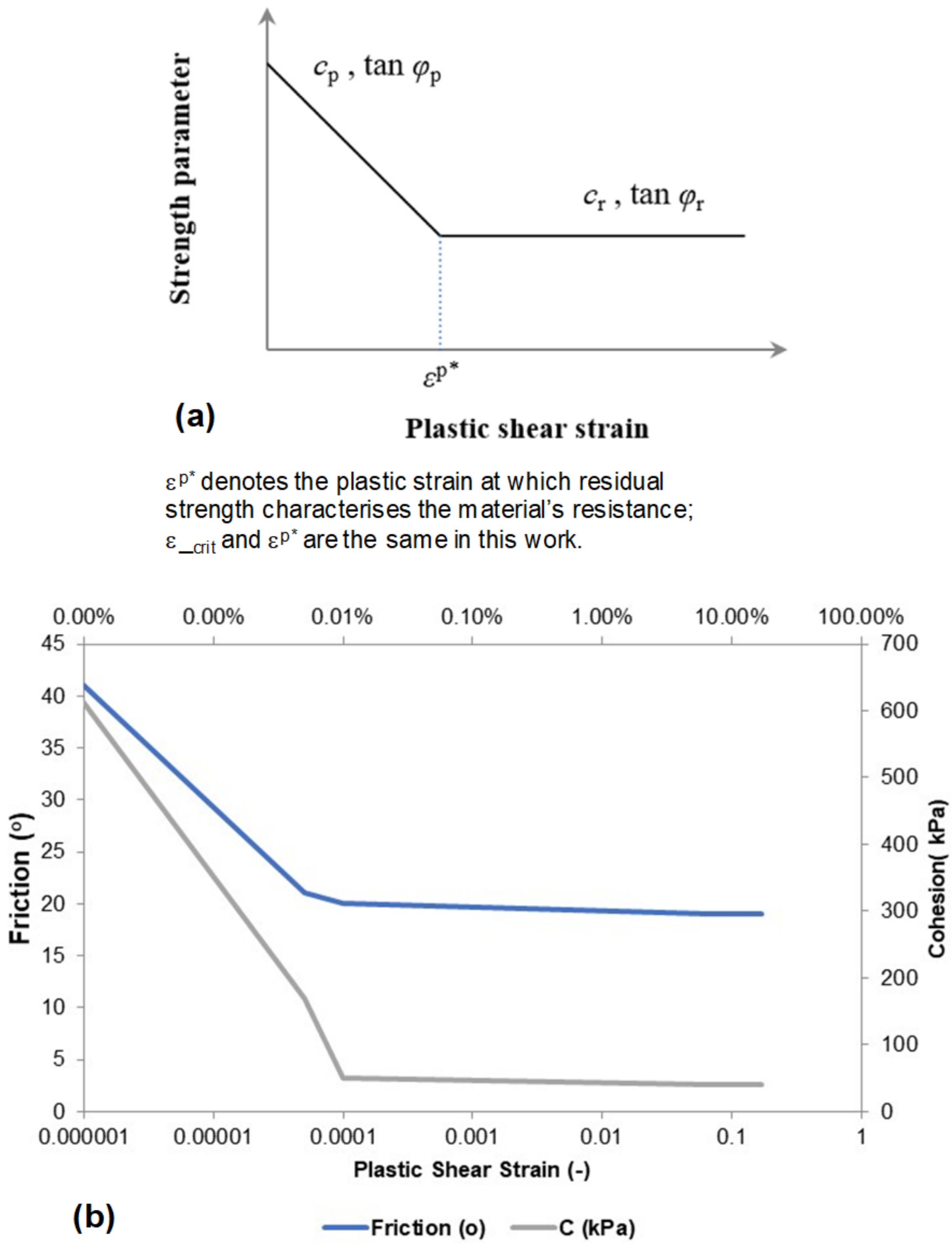

Figure 3-13. (a) Illustration of the strength degradation curve concept for strain softening, with typical shape for slope stability analyses as proposed by Renani and Martin (2020). (b) Example of a strength degradation curve used in this work.

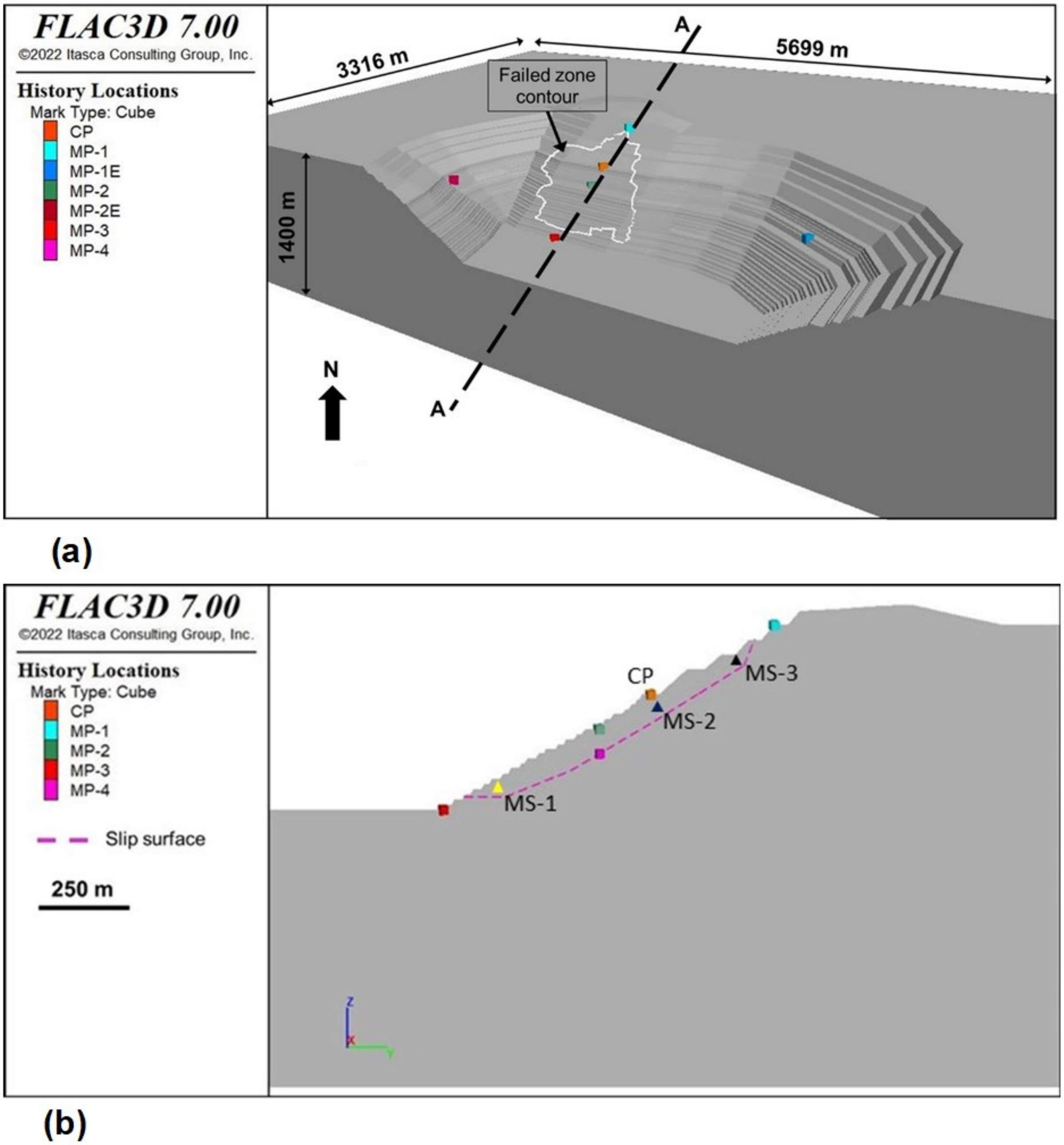

Figure 3-14. Monitoring points incorporated into the model to track the model responses. (a) Isometric view with monitoring points within and external to the failed zone, and (b) cross sectional view showing the monitoring points at surface and depth.

In addition to the above regarding the modelling process and its assumptions, the **Appendix: Details about the calibration process** offers more insights and one illustrative example of how the calibration was done for this work.

3.11 Results

Across the parameter space tested, the best match was achieved when adopting a Mohr-Coulomb with strain softening behaviour model applied to a geological model that included both the dominant lithologies and their alterations (Lit+Alt-SS). This represented the highest level of complexity modelled in this study. Figure 3-15 compares the effects of increasing geological complexity for the elastic-perfectly plastic versus the strain softening behaviour models. Validation against the pit slope failure case study indicates that the more complex models produced better results and fit the actual failure zone. Figure 3-16 compares displacement outcomes for different complexity levels, where the more complex model (Lit+Alt-SS) matches the failure depth and shape (lateral and vertical extents). The tendency to achieve a better match between the higher complexity model results and actual failure is also observed in Figure 3-17, where the Lit-EPP, Lit+Alt-EPP, and Lit+Alt-SS model displacements reproduce the history of measured displacements. However, only the Lit+Alt-SS model complies with all the criteria in Table 3-3, by also matching the observed surface area, failed volume and slip surface depth. Table 3-4 shows the results for failure area, depth, and volume for each model type and the other open-pit walls (NW, NE, SE) where failure did not occur. This in itself provides additional validation, as some models incorrectly predict large failures approaching or greater than one million cubic meters for the other pit walls. Again, only the strain softening model with lithology and alteration (Lit+Alt-SS) reproduces a good match with the actual failure, while also not predicting a large failure for the other pit walls that were observed to be stable. Figure 3-18 presents the results in Table 3-4 as bar charts to visually compare the model results and actual mine site measurements and observations.

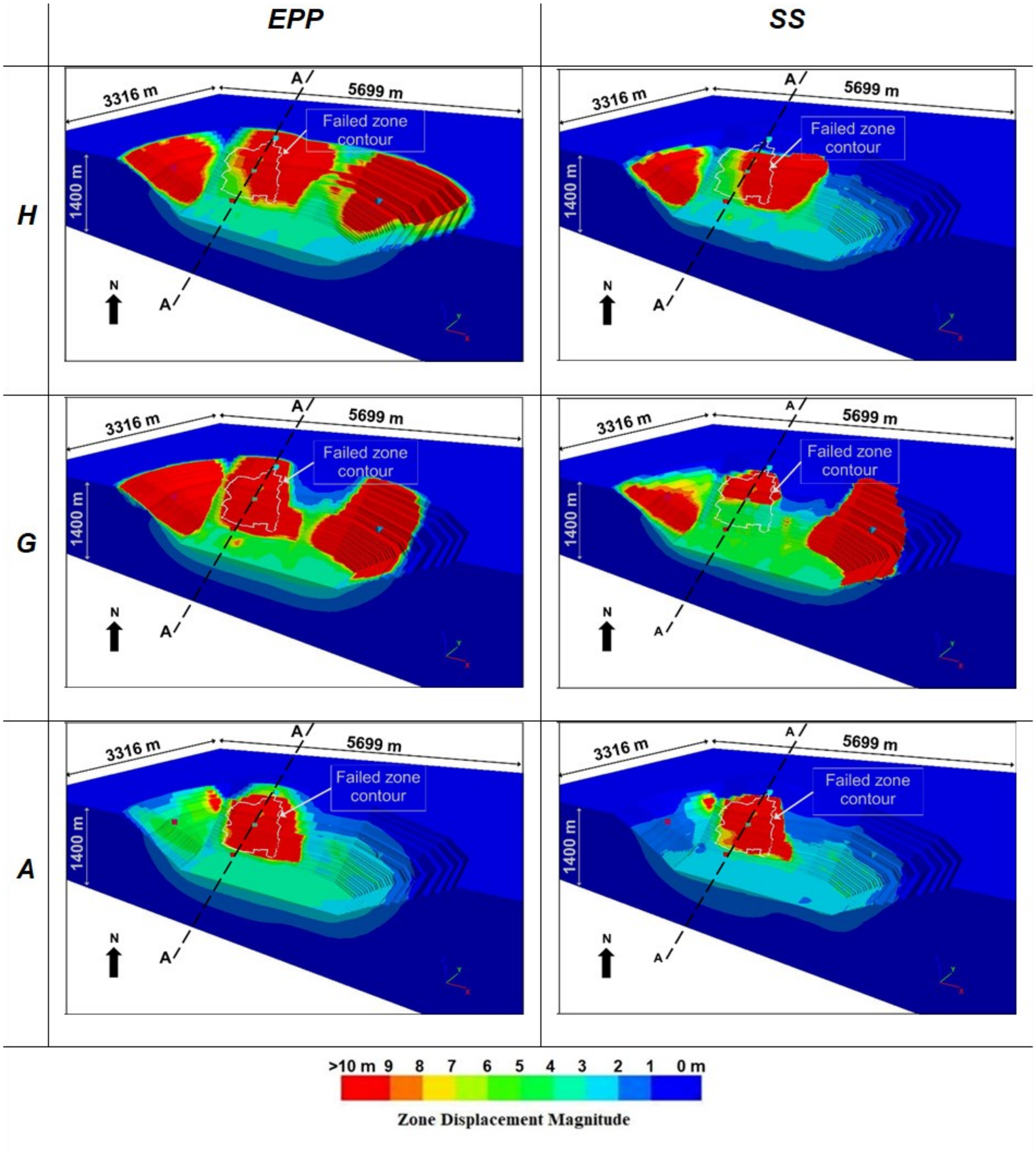

Figure 3-15. Isometric view showing the slope displacement contours (at the surface) after the final pushback excavation sequence, as a function of increasing complexity in the geological model (homogeneous, H → with lithology, G → with lithology and alteration, A) and assuming an elastic-perfectly plastic (EPP) and strain softening (SS) model. Superimposed on the results is the outline of the slope failure. Results from model built on FLAC3D V. 7.0., Itasca Consulting Group, Inc. (2019).

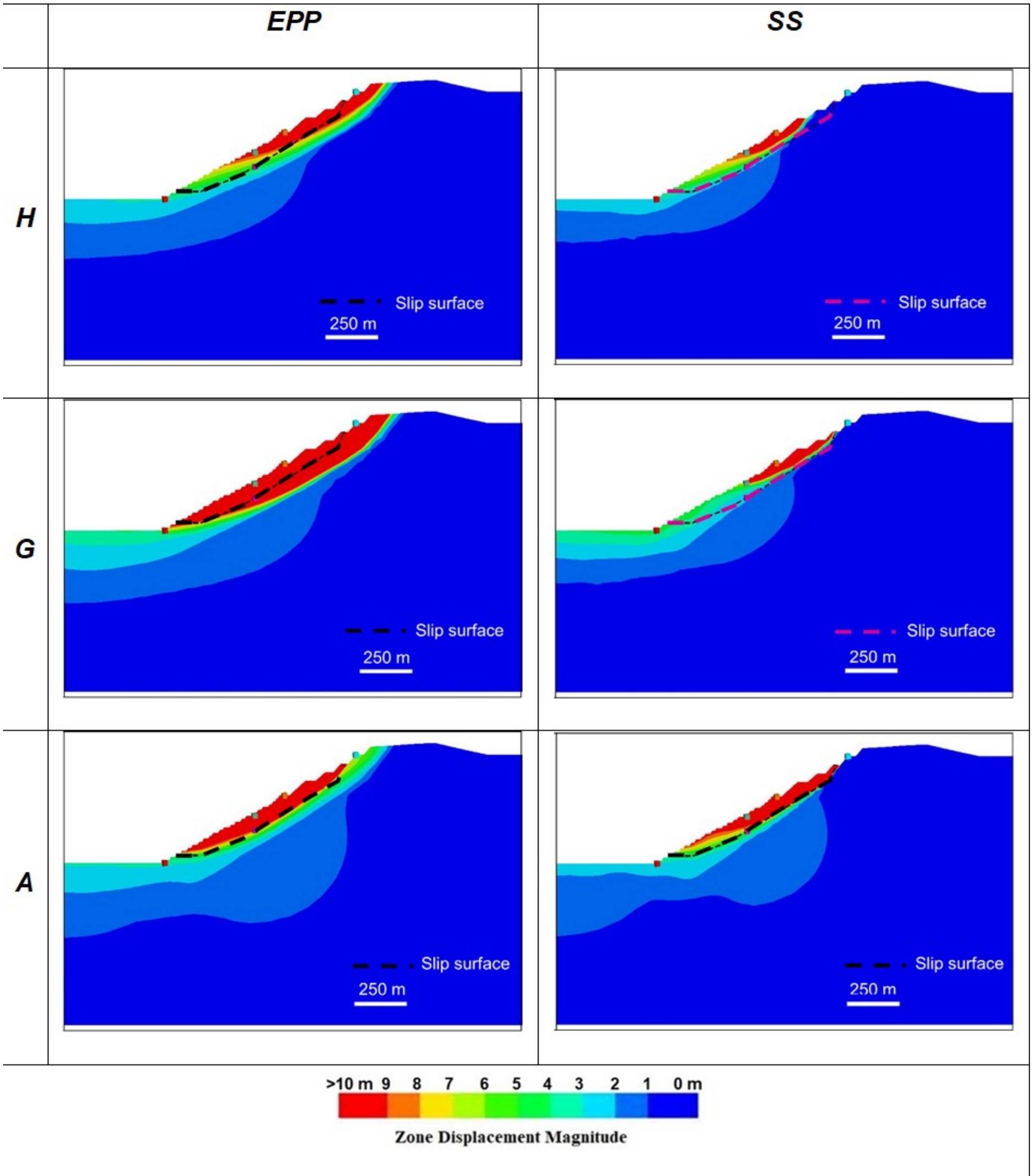

Figure 3-16. Cross section view A-A showing the slope displacements with depth for the final pushback excavation sequence, as a function of increasing complexity in the geological model (homogeneous, H → with lithology, G → with lithology and alteration, A) and assuming an elastic-perfectly plastic (EPP) and strain softening (SS) model. Superimposed on the results is the outline of the slope failure. Results from model built on FLAC3D V. 7.0., Itasca Consulting Group, Inc. (2019).

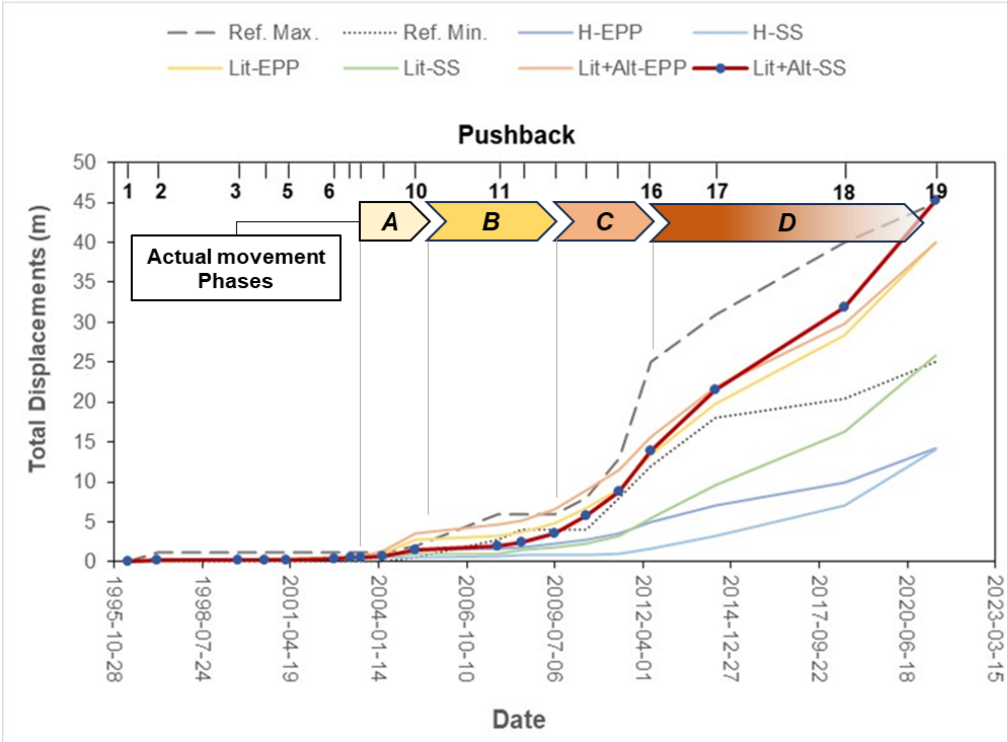

Figure 3-17. Time history of displacements for the different model types compared to the reference measured slope displacements.

Table 3-4. Failure characteristics of the NE wall, and the other walls where failure did not occur, compared to the results for the different model types.

Wall	Failure characteristics							
	NE						NW	SE
Model	**D (m)**	**Var. (%)**	**A (m²)**	**Var. (%)**	**V(m³)**	**Var. (%)**	**A (m²)**	**A (m²)**
H-EPP	101	18%	1.3E+06	105%	7.7E+07	142%	9.3E+05	1.8E+06
H-SS	65	-24%	1.1E+06	76%	4.2E+07	34%	7.2E+05	0
Lit-EPP	145	71%	1.4E+06	116%	1.2E+08	269%	1.2E+06	1.9E+06
Lit-SS	61	-28%	4.0E+05	-38%	1.4E+07	-55%	6.0E+05	1.8E+06
Lit+Alt-EPP	106	25%	1.0E+06	60%	6.3E+07	99%	7.6E+04	0
Lit+Alt-SS	84	-1%	8.7E+05	36%	4.3E+07	35%	3.5E+04	0

D = Slip surface average depth, A = Failure area on slope surface, V = Volume of the failed mass, Var. = Variation of the modelled values (A, D, or V) relative to the actual values (see Figure 3-7)

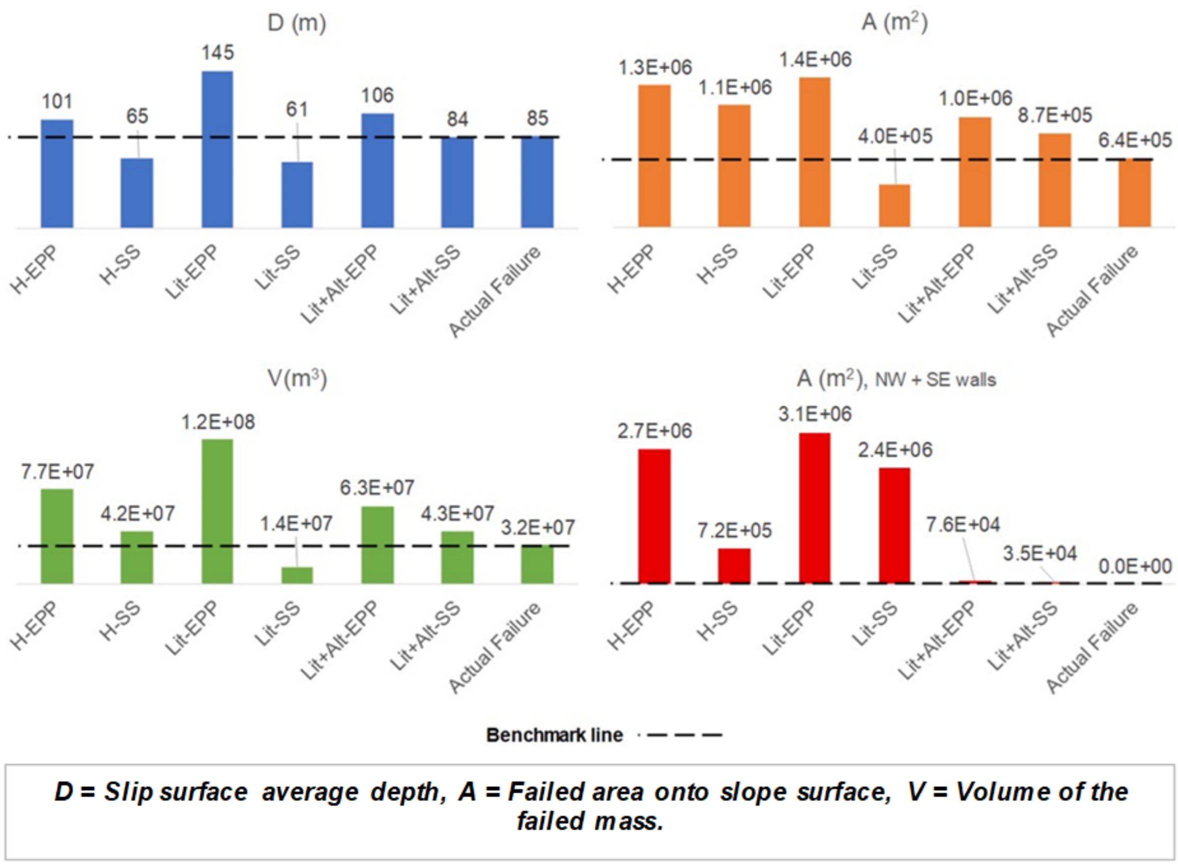

Figure 3-18. Bar charts comparing the modelled failure characteristics for each model type to the actual failure values shown by the black dashed line.

Figure 3-19 shows the plastic strain versus time for the monitoring point (CP); see Figure 3-14, according to the date of when each pushback sequence was completed. Figure 3-19 demonstrates that the higher degree of geological and behaviour complexity achieves a significantly better validation fit against the four different movement phases identified for the actual failure kinematics (from Figure 3-6).

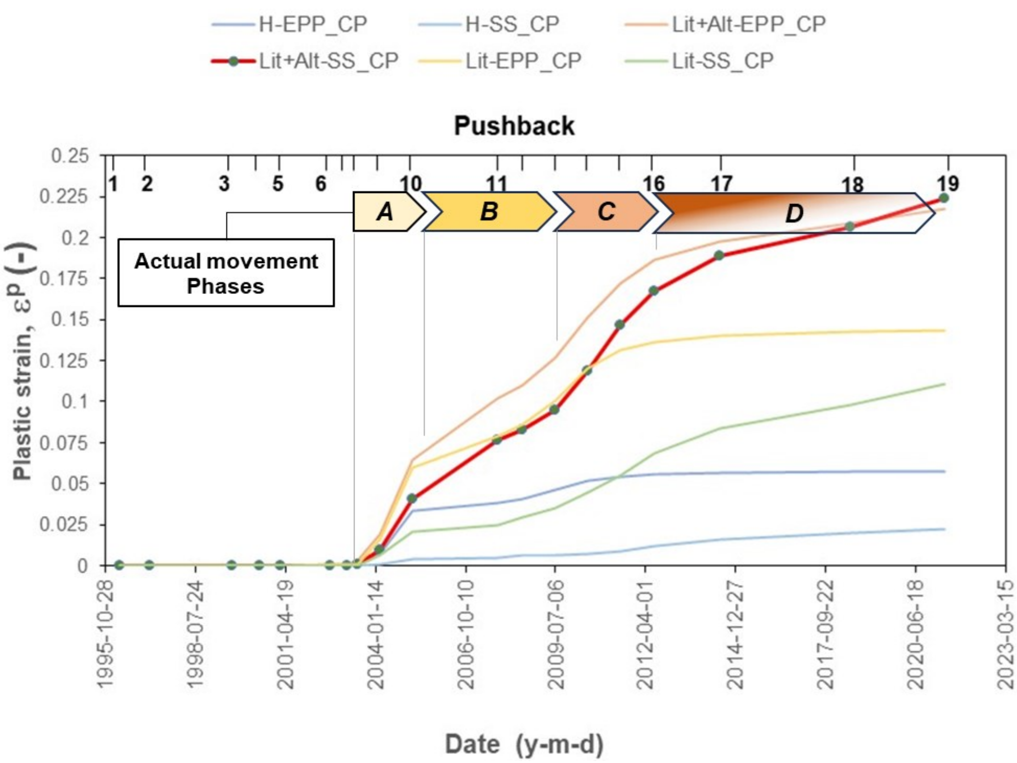

Figure 3-19. History plot of the plastic strains versus time for the different model types.

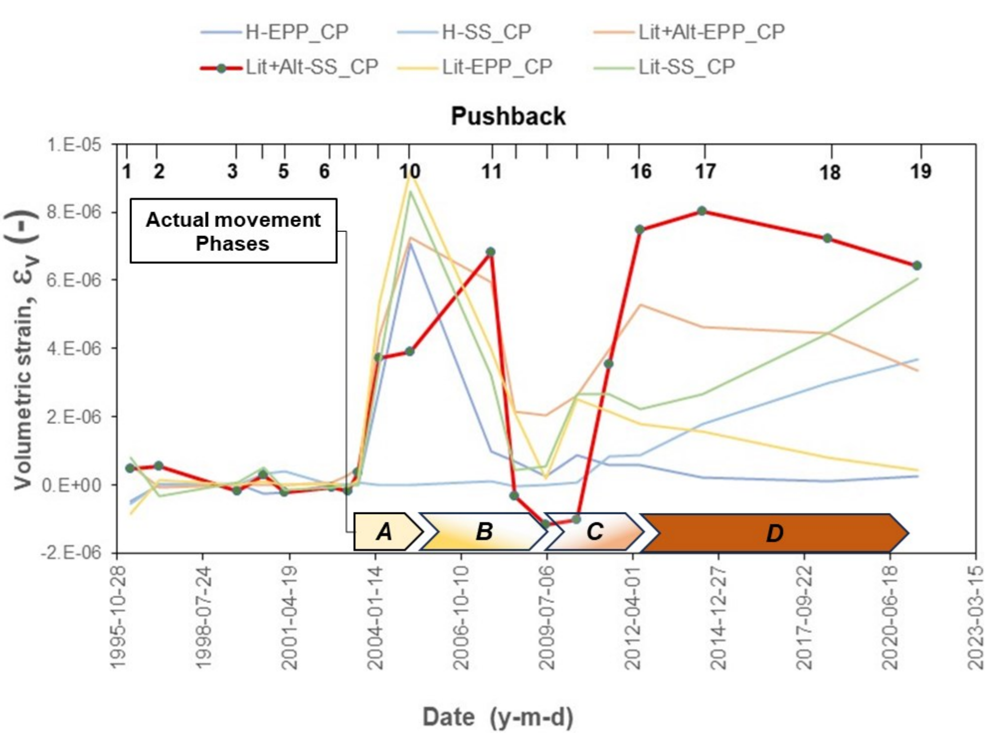

Figure 3-20. History plot of the volumetric strains versus time for the different model types.

Figure 3-20 shows the volumetric strain for the same models and monitoring point. This figure shows a dilative behaviour between pushback sequences seven (7) and eleven (11) when the plastic strain initiates. The material then shows substantial contraction as plastic strains continue, followed by another episode of dilation to develop a constant strain behaviour associated with the slide mass reaching a residual strength state. Figure 3-21 depicts the maximum shear strain rate over time. When the plastic strain initiates, the shear strain rate increases between pushback sequences seven (7) and eleven (11), decreasing towards a constant rate and equilibrating as residual strengths are reached.

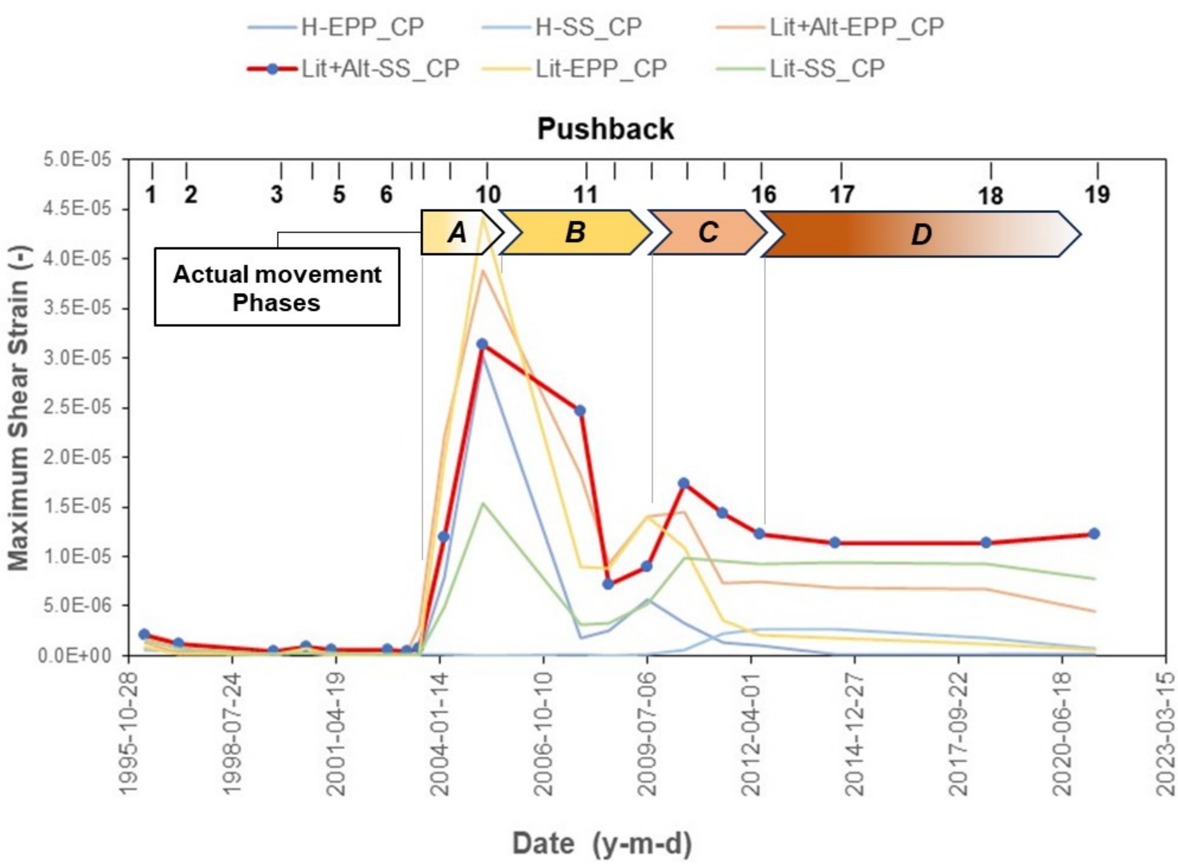

Figure 3-21. History plot of the maximum shear strain rate versus time for the different model types.

The results of the back analyses with respect to the calibration of the best fit strength and strain parameters (c, ϕ, ε_crit) are presented in Table 3-5 and Table 3-6 for the EPP and SS models, respectively. The best set of parameters to reproduce the failure (for the Lit+Alt-SS model) is achieved by using a peak cohesion between 400 and 700 kPa and peak friction between 35 and 45 degrees, and ε_crit of 6.8E-02, with a residual cohesion between 40 and 60 kPa and residual friction angle between 20 and 25 degrees.

Table 3-5. Geomechanical parameters back analysed for the EPP type models. The domains that were involved in the observed failure are identified by an asterisk.

Model Type	**EPP**			
Material	**$\phi_{(p)}$ (o)**	**$c_{(p)}$ (kPa)**	**ψ (o)**	**$\sigma_{t\text{-}rm}$ (kPa)**
Homogeneous	24	50	12	5
Andesite	22	45	11	10
Escondida Stock	21	90	11	10
Rhyolite	35	225	17	10
PZ-Andesite	20	55	10	10
An_Ar	20.4	132	10	13.2
An_Potassic	22.8	161	11	16.1
An_Propylitic	22.2	152	11	15.2
***An_Qz-Ser**	20	50	10	5
***An_Ser-Chl**	22.8	166	11	16.6
***ES_Ar**	19	45	10	4.5
ES_Potassic	22.8	145	11	14.5
***ES_Qz-Ser**	25	70	13	7
ES_Ser-Chl	24.6	159	12	15.9
PZ_Propylitic	22.2	152	11	15.2
PZ_Ser-Chl	22.8	166	11	16.6
Rh_Propylitic	27	207	14	20.7
Rh_Qz-Ser	25.8	178	13	17.8
Rh_Ser-Chl	27	207	14	20.7

$\phi_{(P)}$: Peak friction angle, **c**: Peak cohesion, ψ: Dilation angle, $\sigma_{t\text{-}rm}$: Rock mass tensile strength.

Table 3-6. Geomechanical parameters back analysed for the SS-type models. The best fitting parameters for the Lit+Alt-SS model is enclosed in a red rectangle. The domains that were involved in the observed failure are identified by an asterisk.

Model Type	SS									
Material	$\phi_{(p)}$ (o)	C $_{(p)}$ (kPa)	ψ (o)	σ_{t-rm} (kPa)	$\phi_{(r)}$ (o)	C $_{(r)}$ (kPa)	ψ (o)	σ_{t-rm} (kPa)	$\varepsilon_{\_crit}$ (-)	$\varepsilon_{\_95\%}$ (-)
Homogeneous	36	518	18	52	20	50	0	10	6.8E-02	2.5E-03
Andesite	35	507	21	43	20	40	0	10	7.0E-02	1.0E-04
Escondida Stock	39	491	25	76	20	90	0	10	6.6E-02	1.0E-04
Rhyolite	45	662	27	165	35	200	0	10	6.0E-02	5.0E-02
PZ-Andesite	40	585	24	91	20	50	0	10	6.9E-02	5.0E-02
An_Ar	34	439	17	43.9	25	40	0	10		1.0E-04
An_Potassic	38	537	19	53.7	20	40	0	10		1.0E-02
An_Propylitic	37	506	18.5	50.6	20	40	0	10	7.0E-02	1.0E-02
***An_Qz-Ser**	41	612	28.7	61.2	19	40	0	10		1.0E-04
***An_Ser-Chl**	38	553	19	55.3	20	40	0	10		1.0E-02
***ES_Ar**	44	512	30.8	51.2	19	45	0	10		1.0E-03
ES_Potassic	38	483	19	48.3	25	60	0	10		1.0E-04
***ES_Qz-Ser**	41	520	28.7	52	26	60	0	10		1.0E-04
ES_Ser-Chl	41	529	20.5	52.9	25	60	0	10		1.0E-02
PZ_Propylitic	37	506	18.5	50.6	25	60	0	10	6.6E-02	1.0E-02
PZ_Ser-Chl	38	553	19	55.3	25	60	0	10		1.0E-02
Rh_Propylitic	45	689	22.5	68.9	25	60	0	10		1.0E-02
Rh_Qz-Ser	43	592	21.5	59.2	25	60	0	10		1.0E-02
Rh_Ser-Chl	45	689	22.5	68.9	25	60	0	10		1.0E-02

$\phi_{(P)}$: Peak friction angle, **c**: Peak cohesion, ψ: Dilation angle, σ_{t-rm}: Rock mass tensile strength, $\varepsilon_{\_crit}$: Plastic critical strain where the peak strength values begin to transition to residual values, $\varepsilon_{\_95\%}$: Plastic strain at which the peak strength has decreased to 95% of the difference between the peak and residual values.

Figure 3-22 presents the parameter data from Table 3-5 and Table 3-6 as bar charts to visually compare the differences in the calibrated values as a function of increasing model complexity level. As previously noted, the homogeneous model (H) represents the lowest level of geological complexity, followed by the inclusion of the dominant lithologies only (Lit), and the highest level of complexity includes both the lithology and alteration domains (Lit+Alt). The main observations are:

- The EPP model parameters show slight differences between the average parameters for different geological complexity levels. There is a subtle increase in averages in cohesion values.
- The SS peak strength values produce similar cohesion trends as the EPP models, but with a slight increase in the average parameters with geology complexity level.
- In contrast, the SS residual strength values tend to remain around an average constant value, except for the dilation parameter, which conceptually reduces to zero.

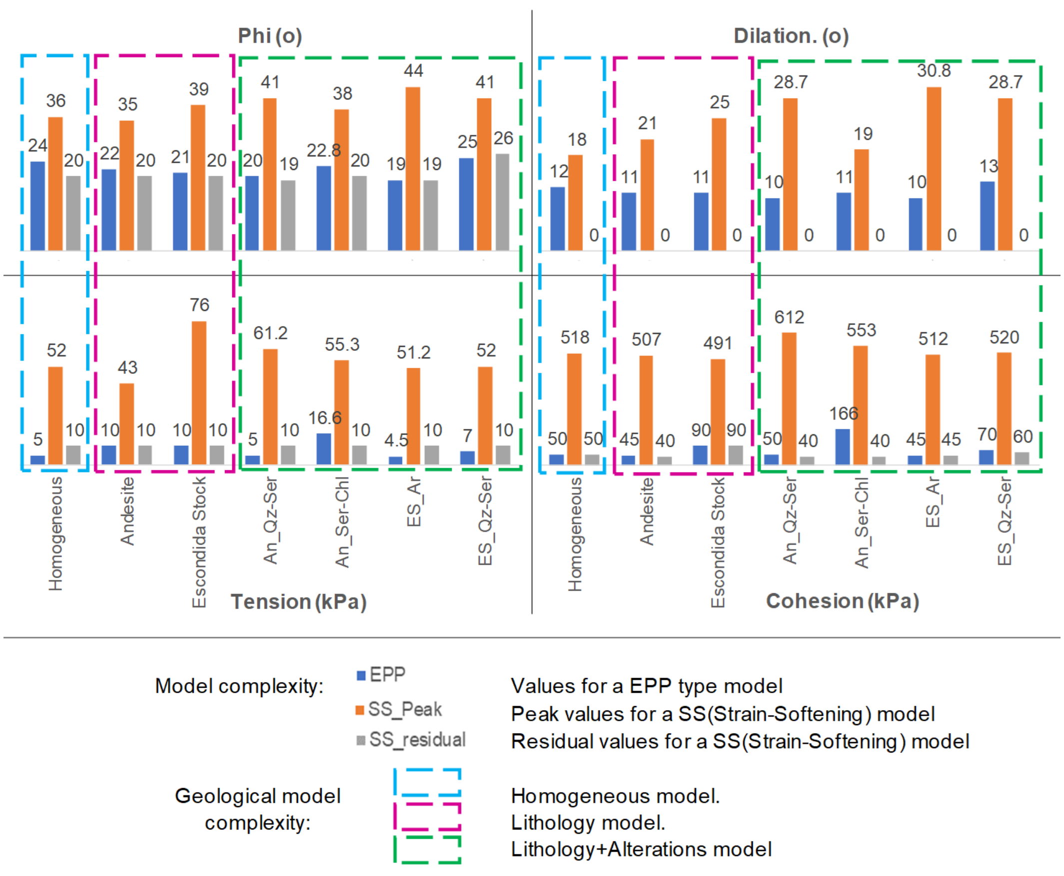

Figure 3-22. Bar charts presenting the change in the rock mass strength parameters as a function of geological and behaviour model complexity for the domains involved in the failure.

The slope failure could not be identified in the elastic models (i.e., using elastic displacements) regardless of the lithological or alteration feature complexity. The perfectly plastic models could reasonably reproduce some observed failure features, such as the timing of accelerations (orange and yellow colour curves in Figure 3-17). However, the EPP models overestimate the extent and depth of failure (Figure 3-18 and Figure 3-19, respectively) and underestimate the peak strength parameters compared to the best-fit model.

The back analysed parameters are plotted in Figure 3-23 together with those from other back analyses involving porphyry deposit lithologies according to Wyllie and Mah (2017) and Hoek and Bray (1981). The best-fitting model results (lithology and alteration with strain softening model; Lit+Alt-SS) show that the calibrated peak strength parameters plot among the typical values for porphyry lithologies (green, orange, and magenta areas in Figure 3-23). The residual parameters are consistent with values for rock discontinuities and soil materials. These observations support the adequacy of the process followed and back analysed parameters.

Figure 3-24 plots the model outputs in terms of plasticity indicator (element tensile or shear failure), maximum shear strains and displacement progression as the pushback excavation advances for the model Lit-Alt-SS. The subscripts n and p in this figure represent the new tensile or shear yielding that occurs in the corresponding pushback sequence and those that accumulate from previous pushback stages, respectively. This diagram shows how the failure initiates and propagates in the model. Before pushback 7, only superficial failure is noticed. These then deepen and localise as the pushback moves towards and reaches its final state. This is compatible with the behaviour of displacements and plastic strains seen in Figure 3-17 and Figure 3-19.

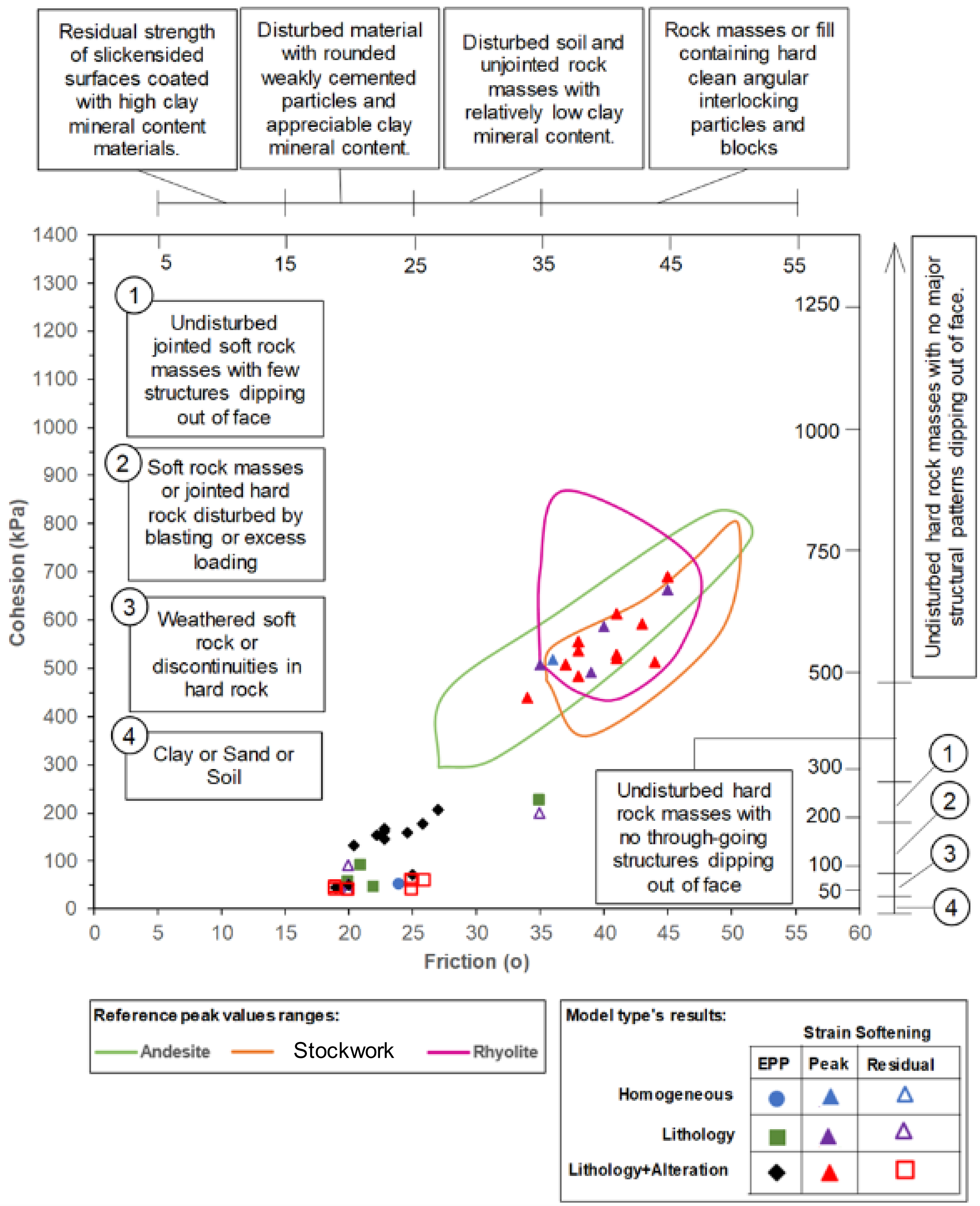

Figure 3-23. Summary plot comparing the back analysed peak and residual strength parameters for the different model variants and typical values obtained in previous studies involving porphyry deposit lithologies (modified from Wyllie & Mah, 2017 after Hoek & Bray, 1981).

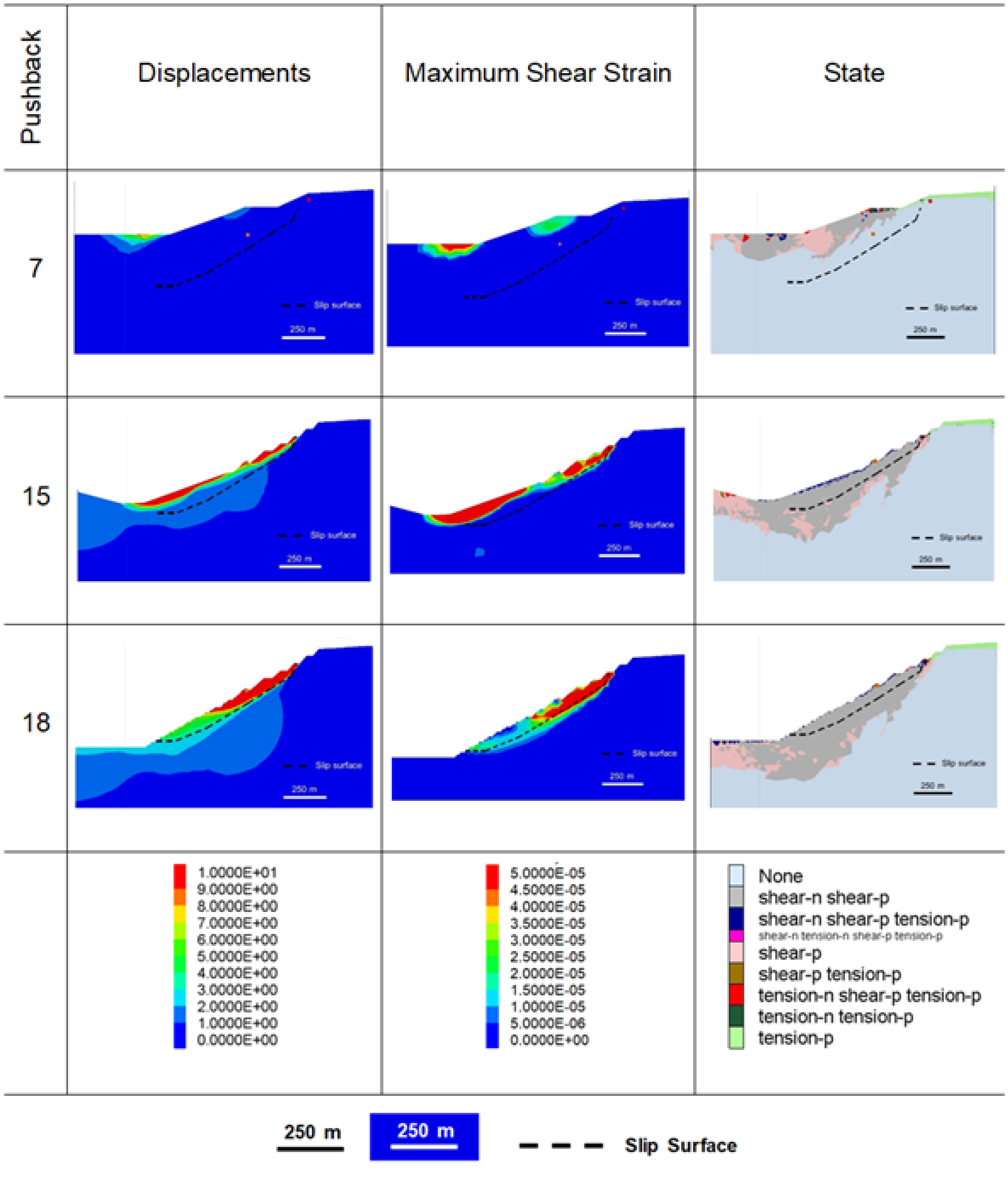

Figure 3-24. Element failure type (shear versus tension) at different key stages in the pushback sequence for the best fitting model (Lit+Alt-SS). Results from model built on FLAC3D V. 7.0., Itasca Consulting Group, Inc. (2019).

Figure 3-25 tracks the principal stress changes (i.e., stress paths) for points MS-1, MS-2, and MS-3 (from Figure 3-14), which correspond with the toe, middle, and crest of the failure area, respectively. The stress trajectories were also compared with their corresponding peak and residual failure envelopes. Note how the stress states reach the peak strength envelopes and how stresses in the failed mass are redirected towards the residual strength envelopes. Before reaching the peak resistance, the materials mainly exhibit deconfinement ($\sigma 3$ loss). After yielding and while softening, they redistribute the $\sigma 1$ and $\sigma 3$ magnitudes, and once residual resistance is mobilised, the trajectories are extensional. Thus, relative to cross-section A-A, representing a longitudinal section through the slide (see Figure 3-14b), it is possible to see that plastic yielding first starts at the crest (following the eighth pushback sequence), which would manifest as tension cracks. The development of tension cracks was the first indicator for the mine site's geotechnical staff that the slope was starting to move. Next, the yielding moves to the middle of the slope and then connects with the toe, after sequence stages 9 and 10. The plastic yielding, localisation of the slide and transition to a residual strength state coincide with the results presented in Figure 3-24.

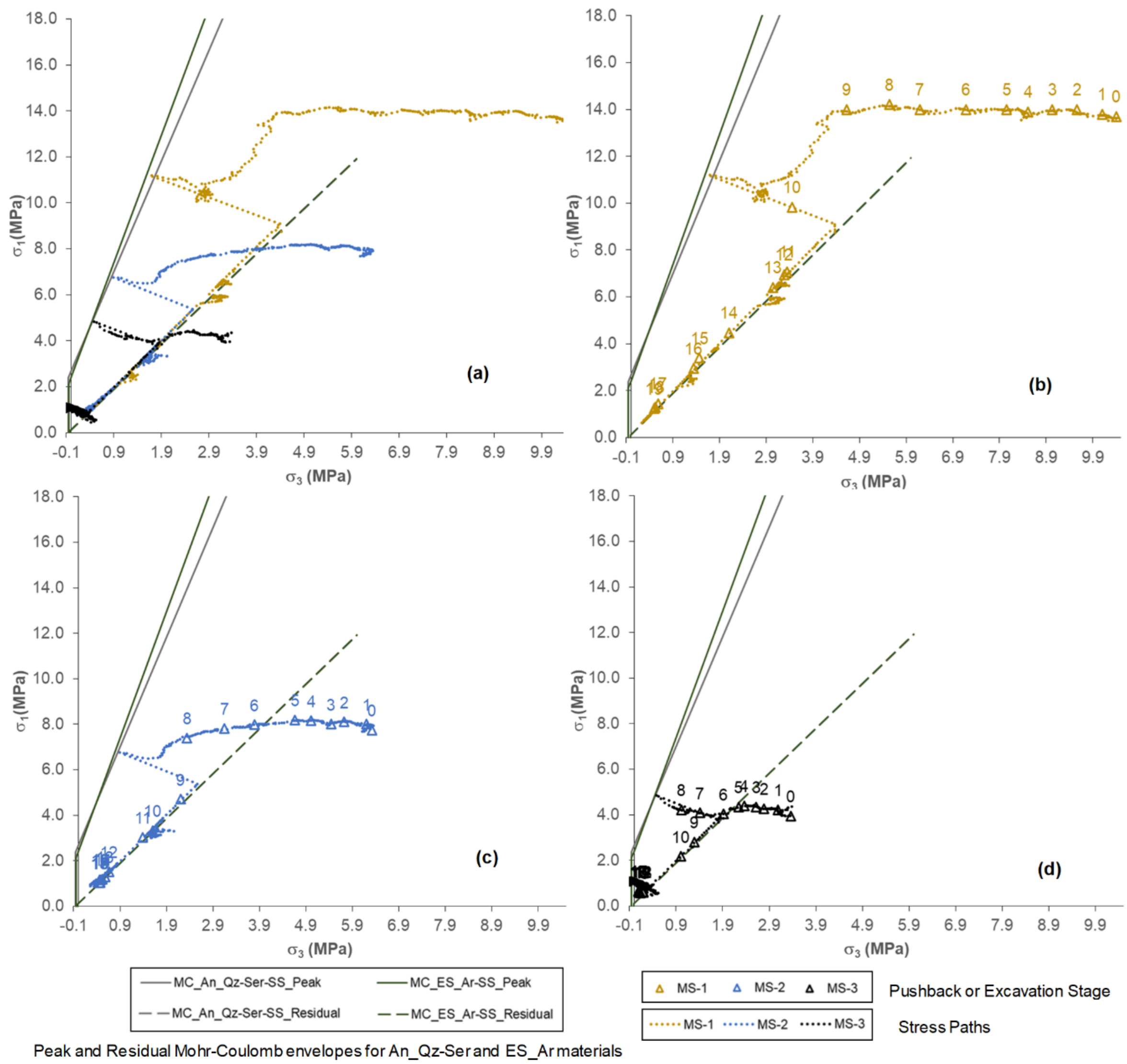

Figure 3-25. Comparison between the different model type stress paths and Mohr-Coulomb peak and residual strength envelopes, assuming homogeneous model strengths for simplicity: (a) Stress path comparison for the slope toe, middle and crest. (b) Detailed stress path for MS-1 (slope toe). (c) Detailed stress path for MS-2 (slope middle. (d) Detailed stress path for MS-3 (slope crest).

3.12 Discussion

The linear elastic models (H-LE, Lit-LE, Lit+Alt-LE) only registered displacements typical to elastic rebounds as the pushbacks exposed the open-pit walls and bottom floor. Elastic rebound depends on the materials' elastic deformation input parameters and is proportional to the distance between the open pit's floor and the model's bottom boundary (Lees, 2016). This model, by design, is not capable of reproducing plastic behaviour. Hence, no speculative signs of failure were observed throughout the excavation process. As the geological model becomes more complex, observed total displacements increase due to lower deformation moduli associated with the more complex domains (e.g., the hydrothermally altered units are less stiff than the unaltered zones).

The EPP and SS models were both able to reproduce observed failure indicators for the northeast wall. The more detailed the geological model, the more accurate the movement prediction regarding the failed zone location and extent on surface (as seen in the isometric views). However, only the Lit+Alt-SS model incorporated sufficient detail to reproduce all validation aspects of the failure, such as the failed mass location, shape on surface, and depth (as seen in the section A-A view). It was observed that the EPP models predicted a more extensive and generalised movement zone than the SS models because the back analysed strength parameters that allowed failure resemble those reported for weathered soft rocks (Wyllie & Mah, 2017; Hoek & Bray, 1981), leading to deeper plastic yielding.

Implementing a model considering lithological units with hydrothermal alterations and a strain softening strength behaviour (Lit+Alt-SS model) was crucial to reproducing the failure mechanism and spatial extent and depth observed. Figure 3-26 (a) presents how the detailed geological model contributed to constraining the extent of the failure, with the upper boundary of the failure coinciding with the An_Ser-Chl – An_Qz-Ser contact, the East and Southeast boundary with the Rh_Qz-Ser – An_Qz-Ser contact, and the toe of the failure with the ES_Qz-Ser – ES_Ar contact. Even though the convexity in the Northeast wall at the failure's northwest flank is an instability factor, the closeness to the North wall helped to mitigate and set limiting boundaries for the movement along the northwestern side of the failure. The pushback reduced the confinement along this lateral margin.

Figure 3-26 (b) shows the lithological contacts and how some match with the failure's slip surface, such as the nearly vertical contact between the An_Qz-Ser and An_Ser-Chl units at the wall crest, the stretched tabular body of ES_Qz-Ser at about 85 metres depth, and the sub-horizontal ES_Ar – ES_Qz-Ser material boundary at the wall's toe. The slip surface depth was controlled by both the spatial distribution of the lithology and alteration units, as well as the strength weakening captured in the strain softening behaviour model.

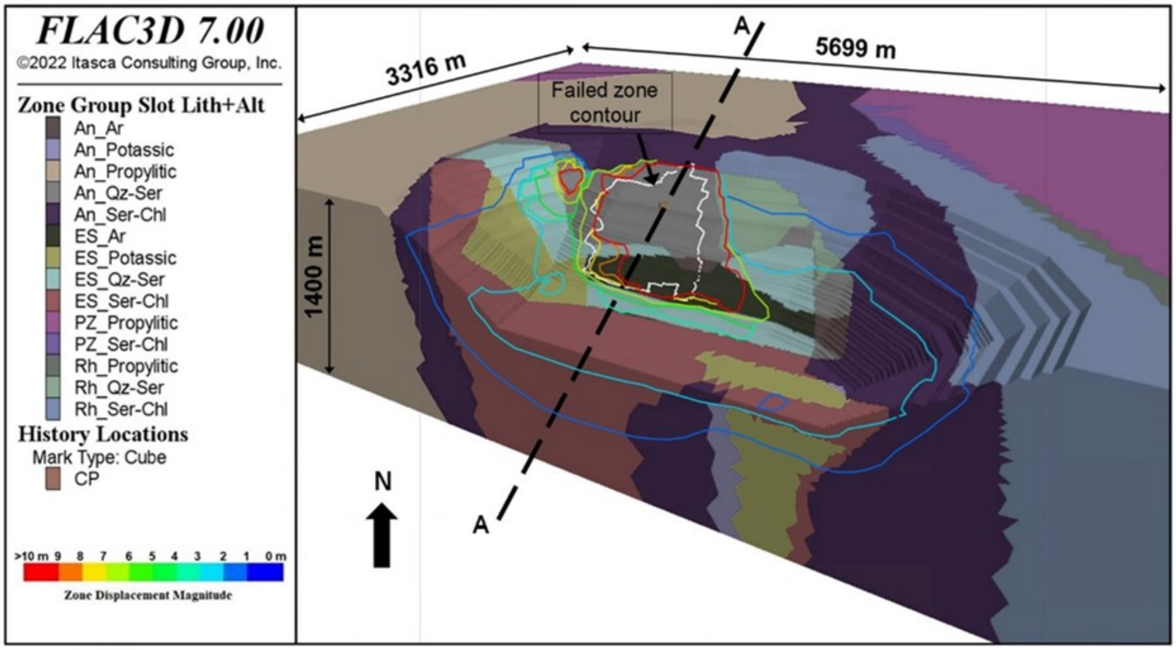

(a)

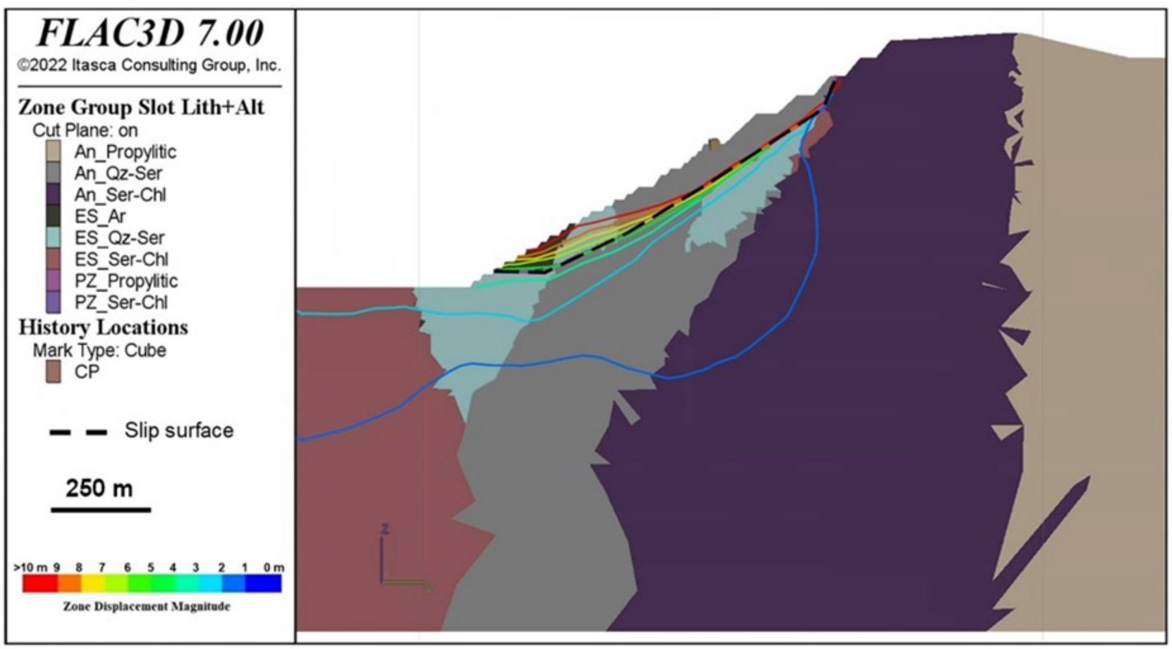

(b)

Figure 3-26. Displacement outcomes relative to the geological model domain contacts. (a) Isometric view and (b) cross section A-A, showing the model's geometrical boundaries, constraints related to the lithologic and alteration contacts, and total displacement contours. Results from model built on FLAC3D V. 7.0., Itasca Consulting Group, Inc. (2019).

The Mohr-Coulomb strength parameters (c and ϕ) reveal a rock mass degradation that is similar to progressive rock failure stress-strain curves by Martin and Chandler (1994), Alejano et al. (2017), Hoek and Brown (1997) and Trivedi (2010) for intact rock, a jointed rock mass, and a fully fractured rock mass, respectively. Figure 3-23, taken from Wyllie and Mah (2017), after Hoek and Bray (1981), shows materials starting from an upper bound of undisturbed hard rock masses or disturbed with block interlocking characteristics to a lower bound of strength parameters characteristic of rock discontinuities and soil material. Most of the degradation curves used in the back analysis for reproducing progressive failure in the rock mass exhibit a bi-linear shape with abrupt loss in resistance (about 95% loss between peak and residual strength) at plastic shear strains for brittle materials between 1E-4 (0.01%) and 1E-2 (1%), and then a slower reduction before reaching residual values at a strain of approximately 7E-2 (7%). The first interval of strength degradation follows that typically reported for brittle rock behaviour, following the cohesion weakening and friction strengthening (CWFS) model recommended by Renani and Martin (2018) for modelling brittle failure for in-situ applications. At the same time, the curve's transition just before the residual strength state is reached corresponds with degradation curves for rock mass discontinuities and their infilling, like those reported by Fereshtenejad et al. (2021) from experimental results for intact rock bridges and nonpersistent discontinuities. It appears that these approaches, as adopted in our study, adequately model the material progressive failure process of the case study.

c and ϕ residual strength parameters further control the back analysed failure shape and depth from the validation case study. This differed from the modelling of the timing of the failure initiation and its progressive development, which were closely related to the excavation sequencing and the corresponding induced stress increments relative to the strength degradation curve shape and thus the critical plastic strain threshold values. The higher the residual friction contribution, the more surficial the failure surface, whilst the higher the residual cohesion the deeper the failure surface.

Although the calibration shape achieved in the back analyses was judged to be satisfactory, it is noted that the more the mesh is distorted, the higher the inaccuracy of the displacement prediction. In this regard, the final displacement values are subject to increasing modelling uncertainty relative to the actual measured values. Moreover, it is known that progressive failure modelled using strain softening is highly dependent on meshing characteristics (Eberhardt, 2008). The ε_critic found in this study would not be unique, as warned by Sjöberg (2001) and other authors. The latter, however, is not expected to impact the values of the back analysed strength parameters significantly but result in changes in the extent and depth of failure.

Back analysis does not always result in a fixed set of parameters but rather in a range of values. As a result, while parameter and epistemic uncertainty are considerably reduced, some parameter uncertainty remains. Also, given the characteristics of the modelling scale, it should be noted that the back analysed parameters would be applicable to similar scale stability analyses.

Although the results depict a progressive failure, the stress redistribution propagation from the top to bottom of the eventual failure differs, in part, from some numerical modelling and parametric studies on strain-softening and brittle behaviour in rock slopes like those done by Zhang et al. (1989). It is believed that differences may arise due to differences in geology and the driver of progressive failure. Preisig et al. (2016) showed that progressive failure initiating at the toe of the failure can be driven by pore pressures concentrating at the toe and reducing the effective stresses in response to seasonal precipitation, in cases where the progressive failure is driven by hydromechanical processes. In this study, the failure case was driven by stress changes resulting from pit deepening and the loss of confinement owing to a specific excavation sequence related to a pushback.

3.13 Conclusions

This study has provided valuable insights into the numerical modelling of large-scale (Inter-ramp scale) progressive failure in rock slopes in the context of deep open-pit mining operations (over 500 metres depth according to Li et al., 2022). The study investigated the effects of geological and behaviour model complexity on the accuracy of predicting progressive failure behaviour against a validation case study of a large pit slope failure initiated in response to a pushback mining sequence. This scenario is typical of many open pit mine slopes.

Through meticulous back analysis, calibration and validation modelling, several significant findings have emerged:

1. **Complexity Matters:** The study proved that as geological and material model complexity grows, so does the accuracy of forecasts predicting progressive collapse. Models with more geological complexity and realistic material behaviour, such as strain softening, better match field measurements. This conclusion emphasises the need to invest in extensive geological surveys and accurate material characterisation for enhanced slope stability evaluations, as well as the use of numerical modelling analyses for stability evaluations as these allow for progressive failure in contrast to limit equilibrium analyses where rock mass strength is required to be constant.

2. **Model Calibration:** The study presented a viable methodology for calibrating progressive failure models with back analysis. Based on the present studies; to better represent a progressive failure mechanism, it is recommendable to start with linear elastic implementations (to validate the model construction) and then to move a

perfectly elastic-plastic model, adding complexity through geological features gradually until the spatial extents of the back analysed failure are approximated in plan view. Finally, the model should move towards a strain-softening constitutive behaviour to match the depth of the slip surface as observed in the field. The former scheme allows checking the model's numerical appropriateness, while bounding the residual strength values fitting the failure, while the latter allows for fine tuning and adjustment to fully calibrate and validate the model against the full spatial and temporal characteristics of the failure.

To match the observed field data, essential parameters such as rock mass cohesion, friction, and critical strain (ε_crit) are adjusted during calibration. The best-fitting model for the case study had peak rock mass cohesion values ranging from 400 to 700 kPa, peak rock mass friction angles ranging from 35 to 45 degrees, and a critical strain (ε_crit) of 6.8E-02, with residual cohesion values ranging from 40 to 60 kPa and residual friction angles ranging from 20 to 25 degrees. This data can help mining operations calibrate their models for similar scenarios in similar geological environments (e.g., porphyry deposits, altered intrusives, etc.). Note that it is important to provide ranges in parameters for which an adequate model response is observed over fixed values.

3. **Rock Mass Behaviour:** The study emphasises the need to capture actual material behaviour, particularly strain softening, to simulate progressive failure accurately. Models accounting for strain softening showed stages of slope acceleration and deceleration, corresponding to observed behaviour. Understanding the rock mass's response to loading is critical for forecasting the timing and extent of failure.

4. **Geological Detail:** Detailed geological models incorporating lithologies and their changes, especially with respect to hydrothermal alteration and its effect on the

rock mass properties, have proven critical for constraining the position and extent of failure. This is especially true in open-pit mining, where geological changes can substantially impact slope stability estimates.

5. **Meshing and Uncertainty:** The procedures developed recognise the importance of meshing quality in progressive failure modelling. The element size in the area of interest must be small enough to capture plastic strain localisation of the sliding surface as it develops but not too small to result in non-practical model run times. Mesh distortion can cause uncertainty in displacement projections. While back analysis can reduce parameter uncertainty, the results still carry some parameter uncertainty related to mesh quality.

6. **Stress Redistribution:** The study sheds light on the stress redistribution process during progressive failure. The behaviour of stress states approaching peak and residual envelopes and how stresses in the failed mass are diverted towards residual envelopes are critical parts of understanding failure mechanisms.

The findings of this study have practical relevance for deep open-pit mining operations, including mine closure where the long-term stability of the slope is susceptible to progressive failure (Carter et al., 2023). The modelling procedures presented provide a valuable framework for improving safety, production reliability and decision-making by enabling more accurate forward analysis modelling. Mining businesses can better assess slope stability and manage risks associated with rock slope failures by understanding the interaction of geological and rock mass behaviour complexity with respect to progressive failure. This study also provides a road map for calibrating and validating models and improving predictions of progressive failure behaviour.

3.14 Acknowledgements

The authors acknowledge the financial support and data made available for this study by the Large Open Pit (LOP) project (https://www.lopproject.com). They also thank Ashley Creighton and Rigoberto Rimmelin for their input and contributions to this work.

Chapter 4

Effect of Excavation Sequence in the development of Inter-Ramp Progressive failure in deep open pit slopes

4.1 Contributions made to this Chapter:

The M.Sc. Recipient carried out the work presented in this chapter, which includes a literature review, data collection, methodology, analysis, discussion of results, and writing of the text.

Dr. Renato Macciotta reviewed all parts of the work and guided the development of the methodology and its application. The other authors reviewed the text and provided edits and additional discussion recommendations.

A version of this Chapter is being prepared for submission to the Engineering Geology journal with the following citation:

Puerta-Mejía, A.F., Deisman, N., Macciotta, R., O’Neil, S., and Eberhardt, E. 2024. Effect of Excavation Sequence in the development of Inter-Ramp Progressive failure in deep open pit slopes. University of Alberta Geotechnical Centre [Unpublished].

4.2 Abstract

Several studies have examined, either empirically or indirectly, the impact of excavation sequencing on slope stability in open-pit mines, emphasising the need for slope design and maintenance. This research aims to understand better the complexities of the connection between excavation sequencing and at large scale slope stability in a deep open pit mine (over 500 meters depth according to Li et al., 2022). The case study depicts a multi-bench progressive collapse on a deep open-pit slope in the Andes mountain range. A numerical model was built using comprehensive data from the observed failure, including field observations, a literature review, and satellite imagery. The model was calibrated to represent the reported failure extent and deformation accurately. Five more excavation sequences were then simulated on the calibrated model to determine their effect on progressive failure and the development of slope instability.

The findings indicate that the excavation sequence considerably affects the timing and extent of failure. Steeper pushback faces and quicker excavation rates hasten the start of failure, resulting in more widespread and deeper failure. Flatter excavation sequences delay failure, but the impacted volume grows fast when it does occur. According to stress path analysis, shorter pathways to peak strength were associated with earlier and more severe failures (larger volumes).

Keywords: Deep open pit slope failure, progressive failure, rock slope engineering, numerical modelling, porphyry deposits, Excavation Impact, Stress Path Effect.

4.3 Introduction

Multiple research endeavours, whether utilising empirical methodologies or indirect approaches, have investigated the effects of excavation sequencing on slope stability in open-pit mines, stressing its significance in shaping slope design principles and ensuring effective maintenance protocols. This point is reinforced by recommendations published by Read and Stacey (2009), which specify key elements for open-pit slope design, and by Hryhoriev (2023), which emphasises the need for enhanced engineering procedures in open-pit mining design and planning. Furthermore, Li (2021) emphasises the need for proper side slope design in open pit mine production and development. These references highlight the necessity of adequate sequence planning in open-pit slope design. Particularly, in sequencing in numerical modelling to understand the behaviour of rock masses, Eberhardt et al. (2004) and Grämiger et al. (2017) used numerical models to investigate the progressive failure in natural rock slopes. Guo et al. (2018), Burlon et al. (2012), and Hou et al. (2007) investigated numerical assessments of ground response during excavation processes of tunnels, diaphragm wall construction, and a deep excavation adjacent to metro tunnels, respectively, and how construction sequencing affects excavation performance in civil applications.

In addition to numerical modelling, other research has focused on different aspects of open-pit slope failure. Geng et al. (2021) evaluated instability processes and deformation features, whereas Gong et al. (2019) used low-cost UAV imaging to study slope erosion during winter freeze-thaw cycles. Furthermore, contemporary monitoring technologies such as LiDAR, InSAR, and GPS have greatly aided our understanding of failure kinematics (Chen et al., 2022; Jaboyedoffet al., 2010). Dick et al. (2015) provided early warning analysis processes for open-pit mine slopes, while Du and Song (2021) used the inverse velocity method to estimate the failure time of open-pit coal mine slope failure.

The combination of numerical simulation and monitoring is well-established in open-pit slope stability studies (Eberhardt, 2008; Luo et al., 2004; Read & Stacey, 2009). These methods enable back-analyses, material model calibration, and forward analysis of pushback behaviour in open-pit slopes. Integrating numerical simulations with monitoring methods has been a leading research strategy (Yuan et al., 2022; Read & Stacey, 2009), with a current focus on numerical simulation analysis for backfill mining techniques (Hu et al., 2022). Despite advances in computational modelling and monitoring, the precise effects of staging sequences on increasing inter-ramp failure are unknown, especially in open-pit mining. Early pioneering efforts by Yu and Coates, 1979, aimed to simulate the effects of different excavation geometries, along with different lithological features (homogeneous, bi, or multi-layered elastic material models) and several pre-mining stresses over the slope stability in pseudo-3D models (axisymmetric models); however, no explicit mention to the excavation sequencing effects was made. Stacey et al. (2003), explicitly modelled the impact of excavation sequencing over slope stability of deep open pits and pre-mining stresses in a parametric study. However, due to such variations, their assessment was limited to determining the generated principal strain field in slopes for elastic materials. Both focussed on determining strain perturbations extension on hypothetical open pit cases. Thus, further work is required to understand the complexity of the interaction between excavation sequencing and slope stability in open-pit mining projects.

Given the lack of detail on the effects of the excavation sequencing on the development of progressive failure for deep open pit slopes, a working hypothesis portrayed in Figure 4-1 indicates a shorter stress path to failure in steeper excavation sequences as opposed to flatter ones. The hypothesis was developed as a framework to guide further analyses. This implies that variations in excavation sequence characteristics, such as the pushback inclination (from being flatter to steeper), the excavation rate (faster or slower ore extraction) or even the pushback orientation, could produce differences at which time progressive failure triggers (onset of failure).

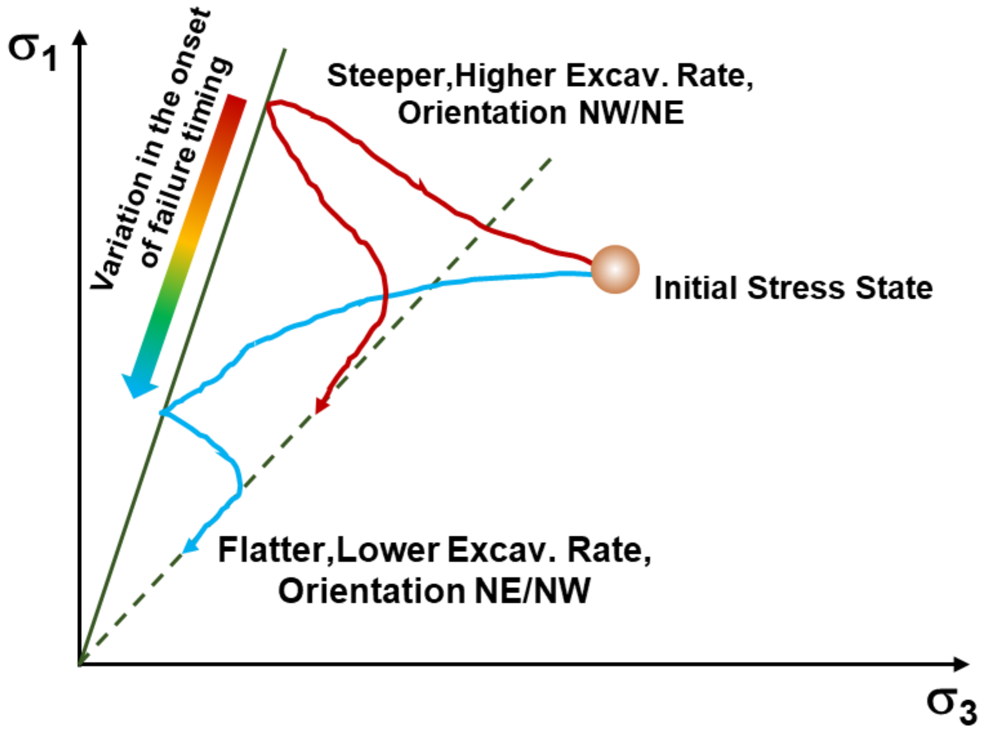

Figure 4-1. Hypothetical stress paths on a principal stress plane, that states that onset of failure timing depends on excavation sequence characteristics.

4.4 Case Study

The presented case study concerns a multi-bench progress failure in a deep open pit slope (over 500 meters in height, according to Li et al., 2022) in the Andes. The progressive instability was first identified in 2007. A panoramic plan view depicts the slope's status in 2019 (see Figure 4-2). The actual open-pit pushback sequencing is presented in Figure 4-3.

Figure 4-2. Google Earth's plan view of the open pit, with failure zone profiles and project location, modified from Google (2019).

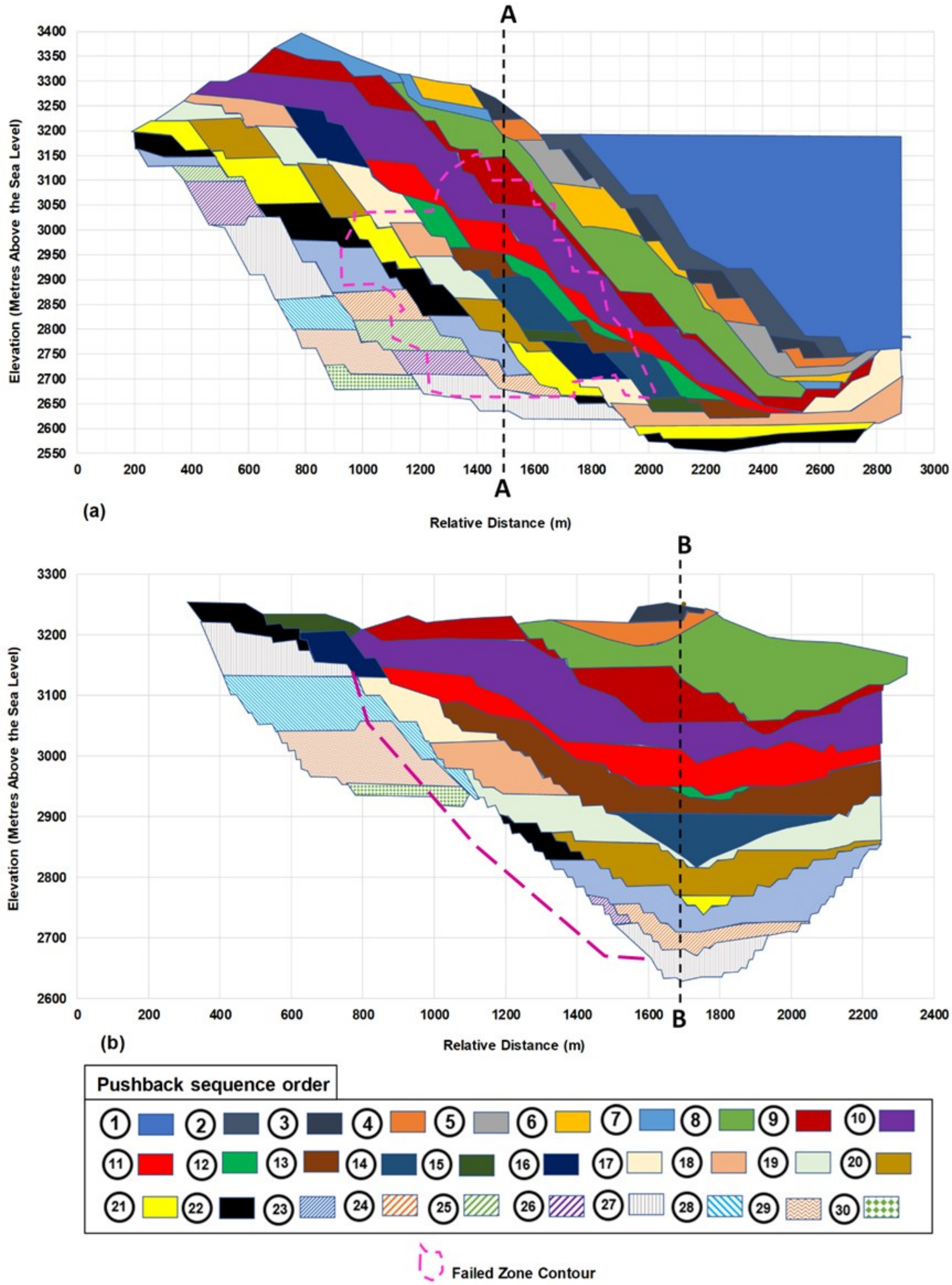

Figure 4-3. Actual open-pit pushback sequence (numbered colours in the legend), pit's transversal (A) and longitudinal (B) cross profiles (adapted from data provided by the mine operator, 2021).

4.4.1 Geological Setting

Site geology consists of igneous bodies in a subducting tectonic plate environment, leading to different degrees of alteration. Site lithologies include Palaeocene andesite, Palaeozoic andesite, quartz monzonitic-granodioritic-porphyritic stock (Stockwork), and a Rhyolite intrusive body. The stock is elliptical, with porphyritic rocks of similar properties. The rhyolite on-site is rich in quartz phenocrysts and altered feldspar phenocrysts. Figure 4-4 depicts the distribution of the at-site outcropping lithologies.

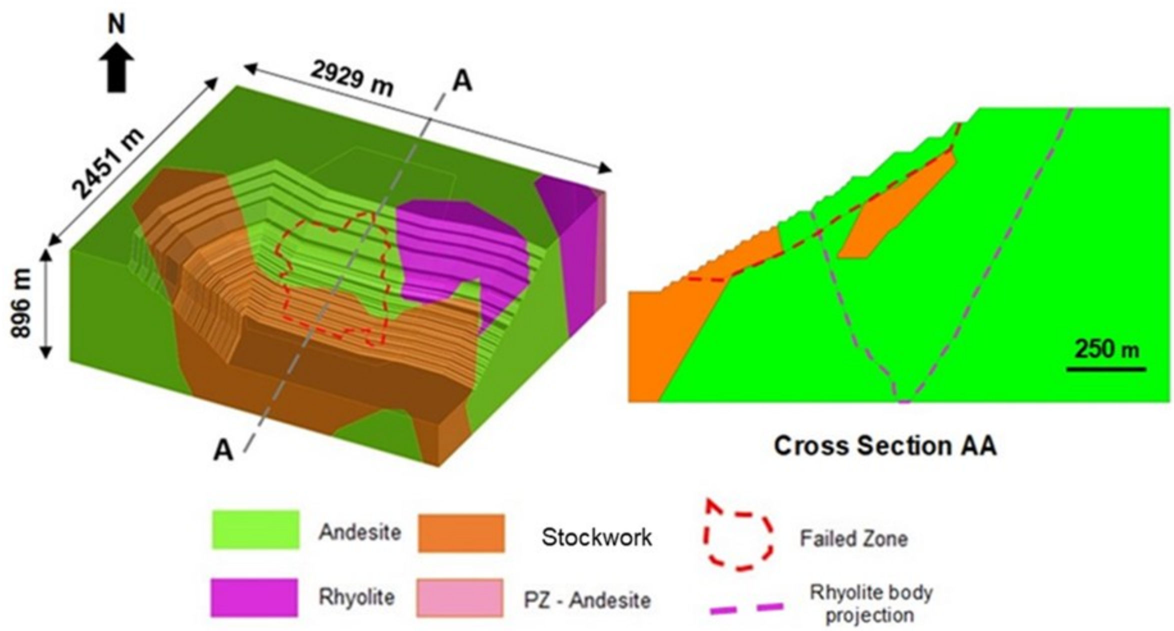

Figure 4-4. Isometric and cross profile views of the outcropping lithologies at the open pit failed area (Built from Garza et al., 2001 descriptions, using Rhinoceros 3D V.7.0, McNeel and others, 2020).

Hydrothermal alterations substantially impact the geomechanical behaviour of rocks, with diverse forms including argillitic, sericitic-chloritic, propyllitic, quartzite-sericitic, quartzitic-sericitic, and potassic. These alterations influence andesite, rhyolite, and porphyry stock. Propyllitic alteration has veins and veinlets containing pyrite, chlorite, and common epidote. Quartzitic-sericitic alteration is more active at fault zones in intrusive rocks. Figure 4-5 depicts the distribution of hydrothermal alterations in the open pit.

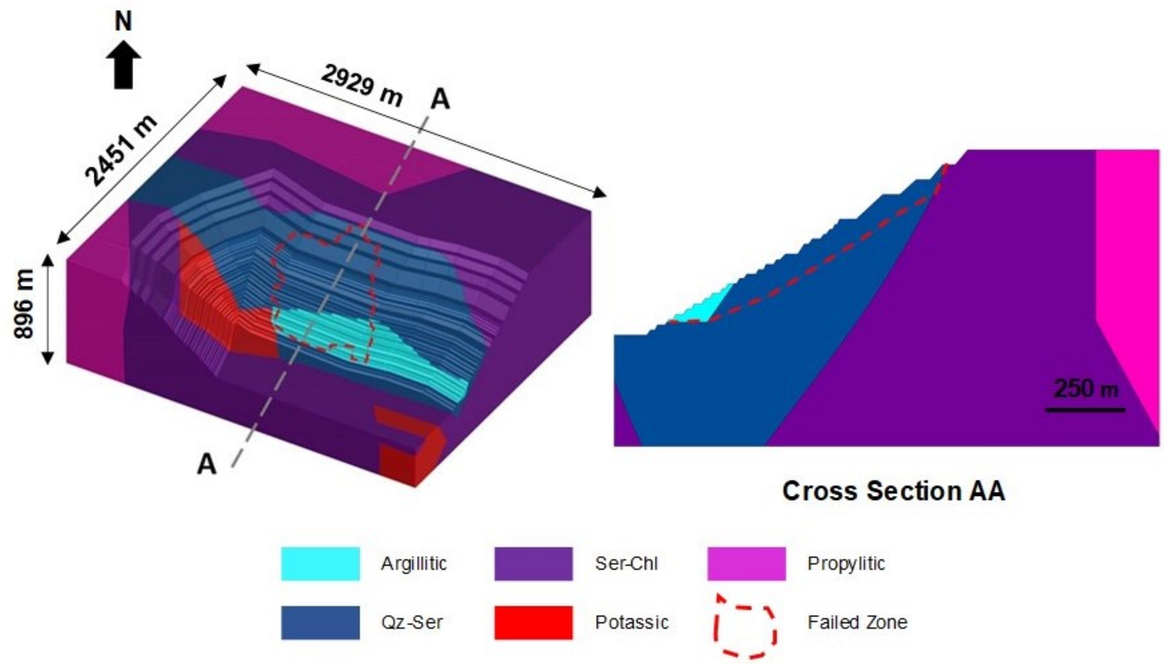

Figure 4-5. Isometric view and cross profile of the different alteration types at the open pit failed area (Built from Garza et al., 2001 descriptions, using Rhinoceros 3D V.7.0, McNeel and others, 2020).

4.4.2 Major structural features, In-situ stresses and Water conditions

The pit's main fault systems are N-S, NE-SW, and NW-SE, with the oldest being part of the Domeyko fault system. The NE-SW faults are tensional structures that cause NW-SE fault vertical movement. The youngest system is associated with argillitic alteration and mineralisation emplacement. Table 4-1 presents major fault orientations and system features.

Table 4-1. Major faults characteristics at the mine zone. (From mine's operator data, 2021).

System	Relative Age	Type	Mineralisation	Profile	Dip	Strike	Main Infillings	Persistence	Thickness
N-S	Oldest	strike	Yes	wavy	70W - 78E	N20W - N20E	Fractured rock or gouge	about 1 km	0.5 m
NW-SE	Post-NS	Strike	Yes	wavy	65S - 70N	N40-75W	gouge	about 1 km	< 2m
NE-SW	Youngest	Normal	No	-	60 - 70 S	N60-75E	Fractured clay gouge	greater than 2 km	0.5 m

The in-situ stress ratio for the mine site was estimated at K = 1.2 based on data from Galarce (2022) on mining and civil projects alongside the Andes region, some close to the case study open pit. The pit's drainage system controls the groundwater levels, with a changing water table between 2750 and 2780 metres (elevation), indicating a dry slope state for modelling purposes.

4.4.3 Material Parameters and Geotechnical Model

The study establishes material characteristics based on the work of Rapiman and Sepulveda (2006), as well as Valdivia and Lorig (2001). Rhyolite (Rh), Stockwork (ES), Paleocene andesite (An), and Palaeozoic andesite (PZ) are the predominant lithologies, and the most common alterations are Potassic (K-Bt), Propyllitic, Ser-Chl (sericitic-chloritic), Qz-Ser (quartzitic-sericitic), and Argillic. The full geotechnical model encompassing lithologies and their alterations is presented in Figure 4-6. Characteristic geomechanical parameters are presented in Table 4-2.

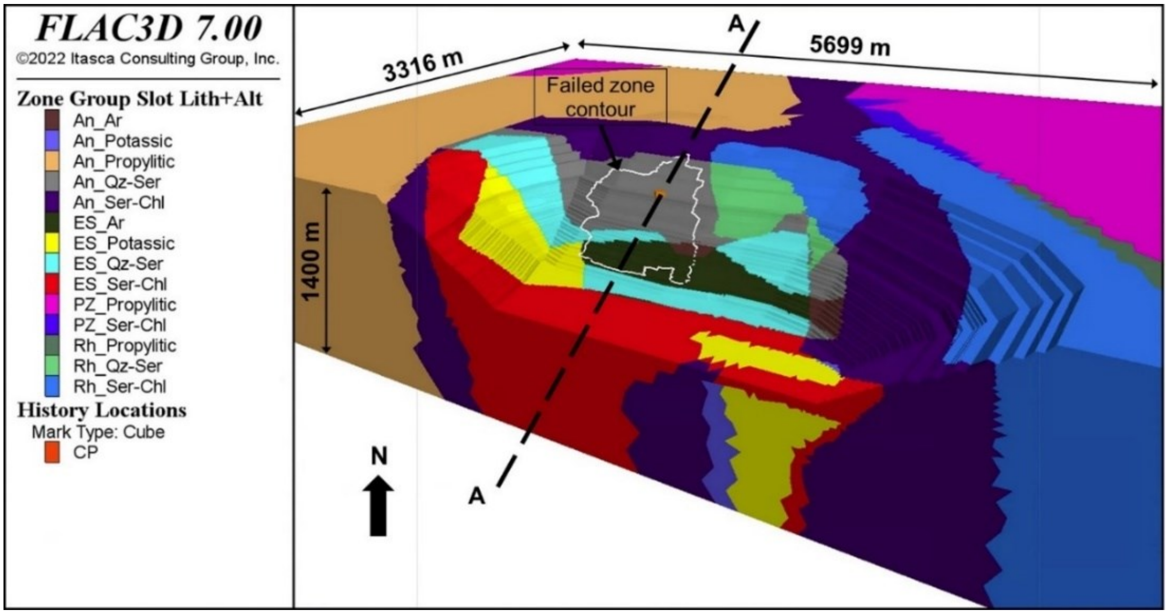

(a)

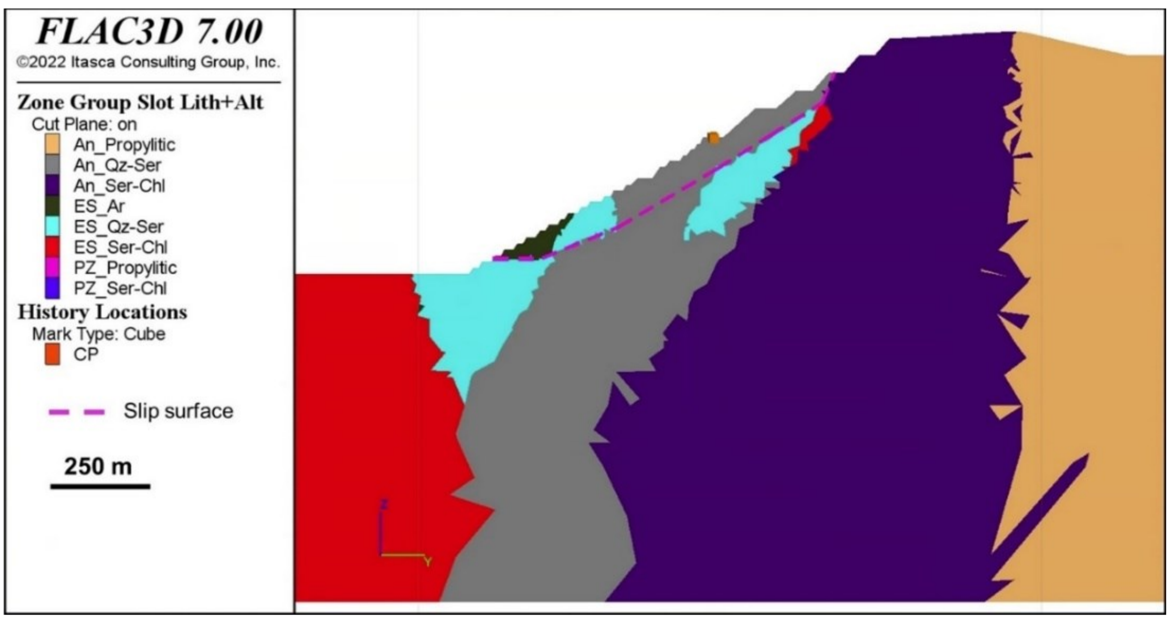

(b)

Figure 4-6. Geotechnical model summarising lithological and hydrothermal alteration materials' distribution and their relationship regarding failed zone location, (a) Isometrical view, and (b) profile A's view. An, ES, PZ and Rh correspond to the different lithologies Andesite, Stockwork, Paleozoic Andesite and Rhyolite, respectively. The alteration type is noted after a dash mark. Model built on FLAC3D V. 7.0., Itasca Consulting Group, Inc (2019).

Table 4-2. Geomechanical parameters compilation for the mine site outcropping materials, according to their lithology and alteration type. Rapiman and Sepulveda (2006) as well as Valdivia and Lorig (2001).

	γ (kN/m^3)		$\phi'_{(P)}$ (o)		C' (kPa)		ψ (o)		E_{rm} (GPa)		ν_{rm}		$\varepsilon_{\_crit}$	
	Avg.	**StdDev.**	**Avg.**	**StdDev.**	**Avg.**	**StdDev.**	**Avg.**	**StdDev.**	**Avg.**	**StdDev.**	**Avg.**	**StdDev.**	**Avg.**	**StdDev.**
Andesite														
Argillic	21	0	34	4	439	97	16	5	4.2	4.6	0.27	0.01	8E-02	1E-02
K-Bt	25	0	38	2	537	32	23	2	12.6	5.3	0.24	0.01	6E-02	7E-03
Qz-Ser	25	0	40	4	535	113	23	3	9.9	3.9	0.24	0.01	6E-02	7E-03
Ser-Chl	25	-	30	-	435	-	15	-	4	-	0.26	-	7E-02	-
Escondida Stock														
Argillic	21.3	1.3	39	10	394	244	20	4	3.6	0.8	0.26	0	7E-02	3E-03
Propylitic	25	-	38	-	526	-	20	-	6.1	-	0.25	-	7E-02	-
K-Bt	25.3	0.5	38	6	483	143	22	4	11.4	6.9	0.24	0.01	6E-02	9E-03
Qz-Ser	25	0.1	39	4	506	143	23	3	10.6	7	0.24	0.01	6E-02	7E-03
Ser-Chl	25	0	41	2	529	67	20	2	4.6	1.5	0.26	0.01	7E-02	5E-03
Rhyolite														
Argillic	21.3	-	43	-	1287	-	23	-	6.1	-	0.25	-	7E-02	-
Propylitic	25	-	45	-	689	-	26	-	9.8	-	0.24	-	6E-02	-
K-Bt	26	-	37	-	840	-	21	-	9.5	-	0.25	-	6E-02	-
Qz-Ser	24.9	0.1	43	4	592	98	27	3	14.7	6.1	0.24	0.01	6E-02	8E-03
Ser-Chl	25	-	45	-	689	-	26	-	9.8	-	0.24	-	6E-02	-

γ : Unit weight, $\phi'_{(P)}$: Maximum friction angle (Phi), **C'**: Cohesion
ψ: Dilation angle (Dil.), E_{rm}: Rock mass deformation modulus, ν_{rm}: Poisson ratio
$\varepsilon_{\_crit}$: Plastic critical strain.
Strain at which material's resistance reaches residual values.

The NE and SW pit walls were vertically and laterally deconfined following the phase sequencing of excavations in the NW direction. Because of non-daylighting planar and wedge blocks related to the NW and NW+NS fault systems, the NE wall has been unstable since 1991. In 2007, the first obvious inter-bench cracks were discovered, and since then, signs of instability continued at accelerated rates. Google Earth Satellite image analysis was employed to supplement and enhance the displacement record, especially between 2011 and 2017.

Satellite photos were locked to latitude and longitude ranges and eye altitude for displacement estimations based on aerial photographs. On each image and in the vicinity of the prism with available displacement data, the horizontal separation between failed bench edges and the interpreted undisturbed location was measured. Figure 4-7 portrays the estimation procedure.

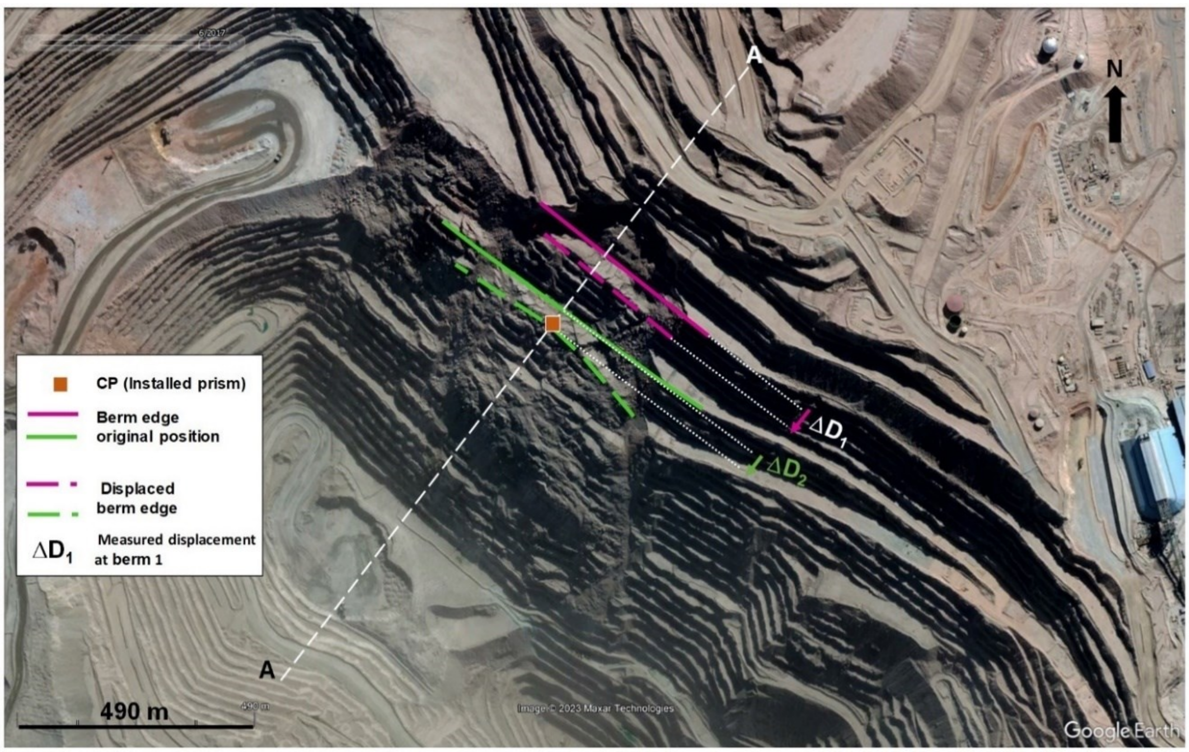

Figure 4-7. General procedure for obtaining displacement estimates. For example, the methodology application for June 2017 (modified from Google, 2017).

Figure 4-8 shows a history displacement plot of crack extension progress and prism location, indicating how the failure progressed from an initial bench-scale to an inter-ramp failure. The blue line is based on the displacement estimates from photographic information, the red line is survey point data, and the dashed red line is measured data shifted to match the estimated displacement from photographs at the start of measurement. Both dashed red and blue lines serve as upper and lower bounds for modelling calibration purposes.

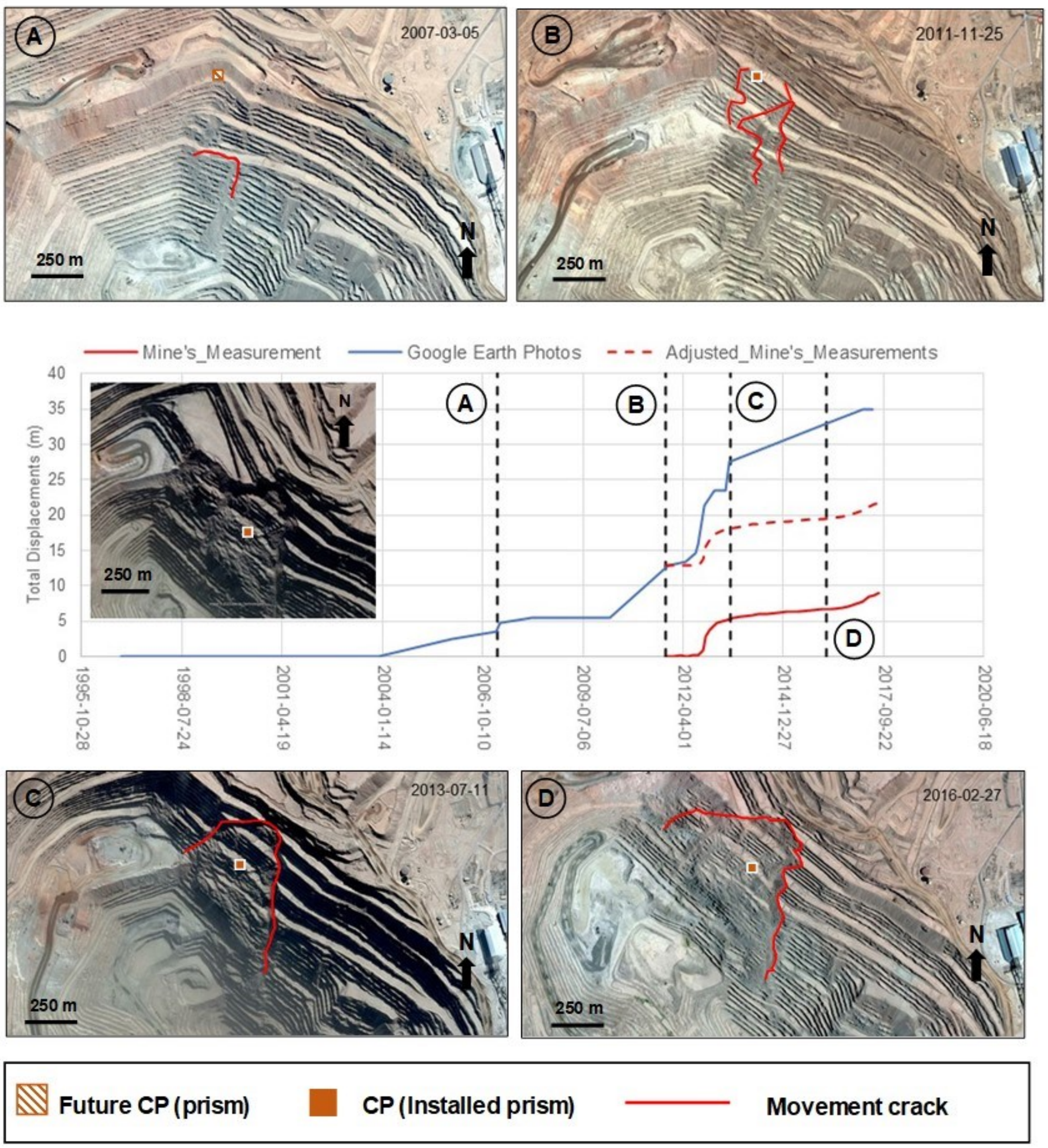

Figure 4-8. History plot of a tracking point onto the failed mass, and images showing cracking evolution (from data provided by the operator in 2021. imagery modified from Google, 2007 2011, 2013, 2016).

The history displacement plot depicts four movement stages: a progressive phase between 2004 and 2006, a retrogressive phase around 2010, and a third progressive phase until 2013. According to the open-pit operators, the failure mechanism was translational, with the slip surface 30 degrees parallel to the slope face. Figure 4-9 depicts the failure's main features.

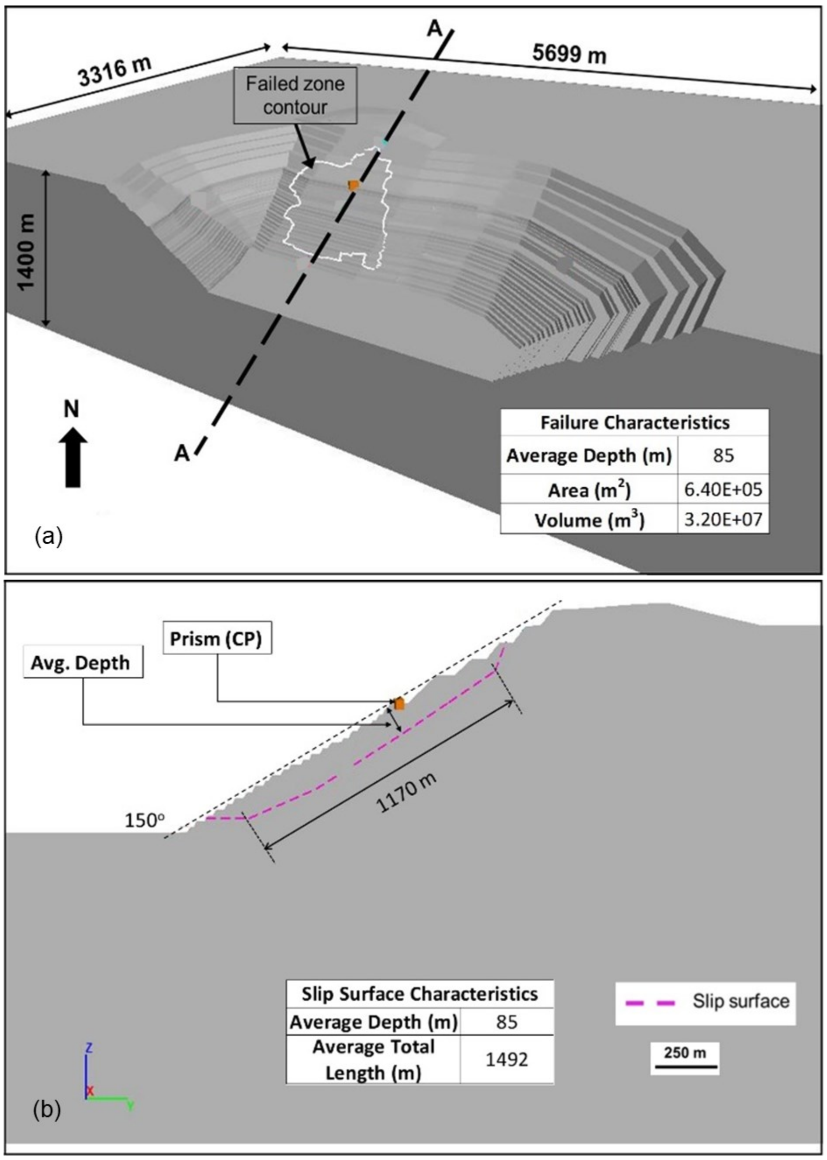

Figure 4-9. Failure characteristics: (a) Isometric view with movement extension, (b) Cross section A with slip surface features. Analysis model with data provided by mine operator (2021), and built on FLAC3D V.7.0., Itasca Consulting Group, Inc (2019).

4.5 Modelling Process

The entire process is visually represented in a flow chart in Figure 4-10.

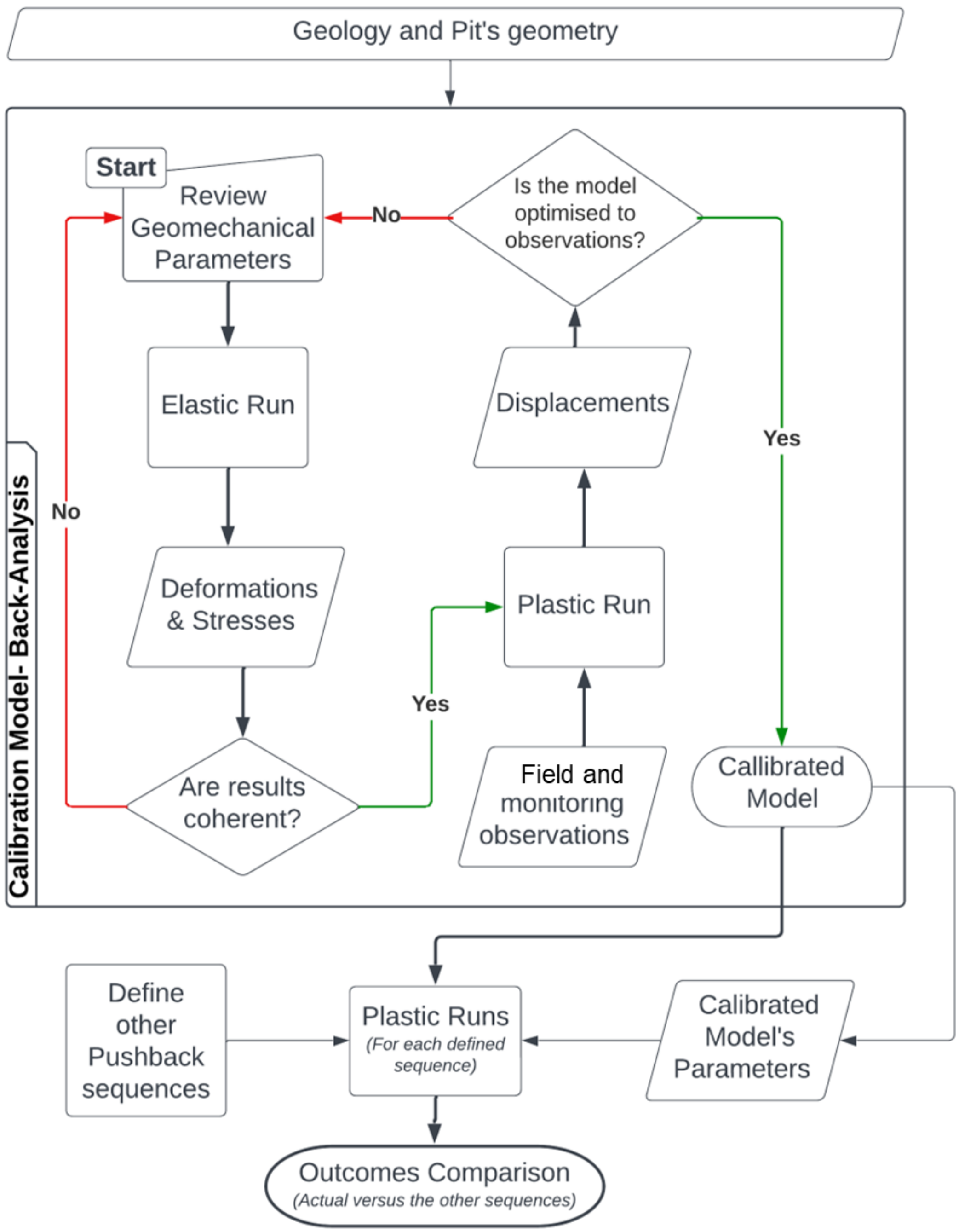

Figure 4-10. Flow chart showing the general procedures for analysing the excavation sequencing on modelling progressive failure in deep open-pit slopes.

The process began with calibrating the model to the observed failure extents and deformation. This initial model aimed to reproduce a specific open-pit slope failure observed with the actual open-pit excavation sequencing. The calibration involved iteratively adjusting model parameters from those in Table 4-2 until the simulation closely matched the observed outcomes, as in Puerta-Mejía et al., in press (chapter 3). The first step in this process involved gathering comprehensive data on the observed failure. This data, sourced from field observations, literature review, and satellite imaging, formed the basis for our computational model. The model's parameters were initialised using existing geological and technical data, Puerta-Mejía et al., in press (chapter 3).

The next step was to extend the analysis to simulate the response of the excavated slope under various excavation sequences. The rationale for the different pushback sequences is that we chose a reasonable but cautious and non-economic sequence that kept the phases' slopes as flat as possible instead of a very aggressive sequence that maximised the total slope, resulting in a very economical but dangerous configuration. Between those two extreme examples, distinct sequences exist. This involved conducting plastic runs for each excavation process. The results from these runs were thoroughly compared to identify any variations in failure mechanisms, failure surfaces, or displacement and stress fields.

The insights gained from this comparative analysis allowed us to conclude the impact of alternative excavation sequences on the stability of the open-pit slope. By employing this modelling approach, we created a robust tool for evaluating the stability implications of different excavation sequences.

4.5.1 Model's Characteristics and Pushback Sequencings

For the calibrated model, Figure 4-11 (b) simplifies the actual mine pushback sequencing shown earlier Figure 4-3. It illustrates other characteristics, such as the model's dimensions and mesh grading (Figure 4-11 (a)). Additionally, five (5) trial sequencings were created considering different geometrical features for pushbacks. Figure 4-12 Illustrates the above definitions and presents their characteristic geometrical parameters.

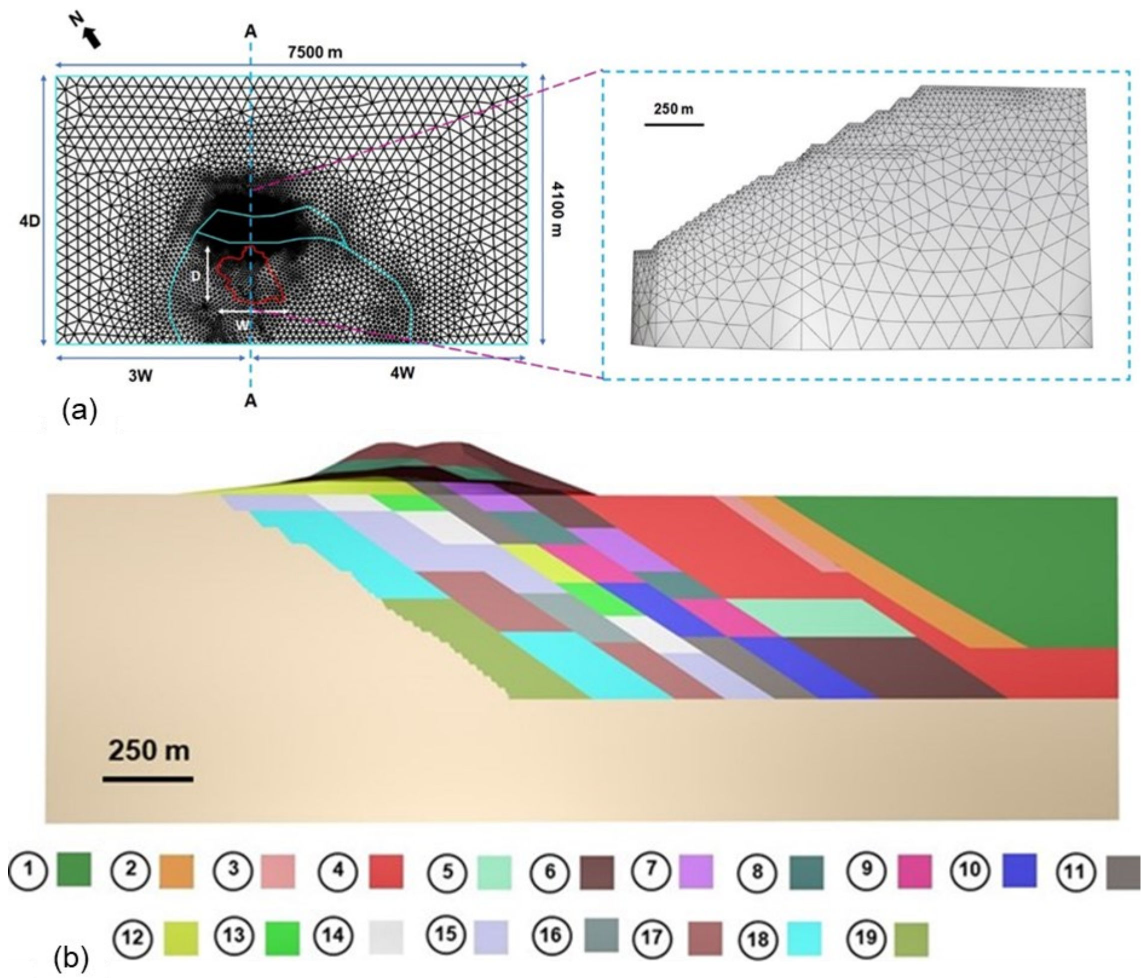

Figure 4-11. Base model characteristics (calibrated model): (a) Plan and cross profile views with overall model's dimensions and mesh grading, (b) Longitudinal cross profile (B) with the simplified actual mine's pushback sequence.

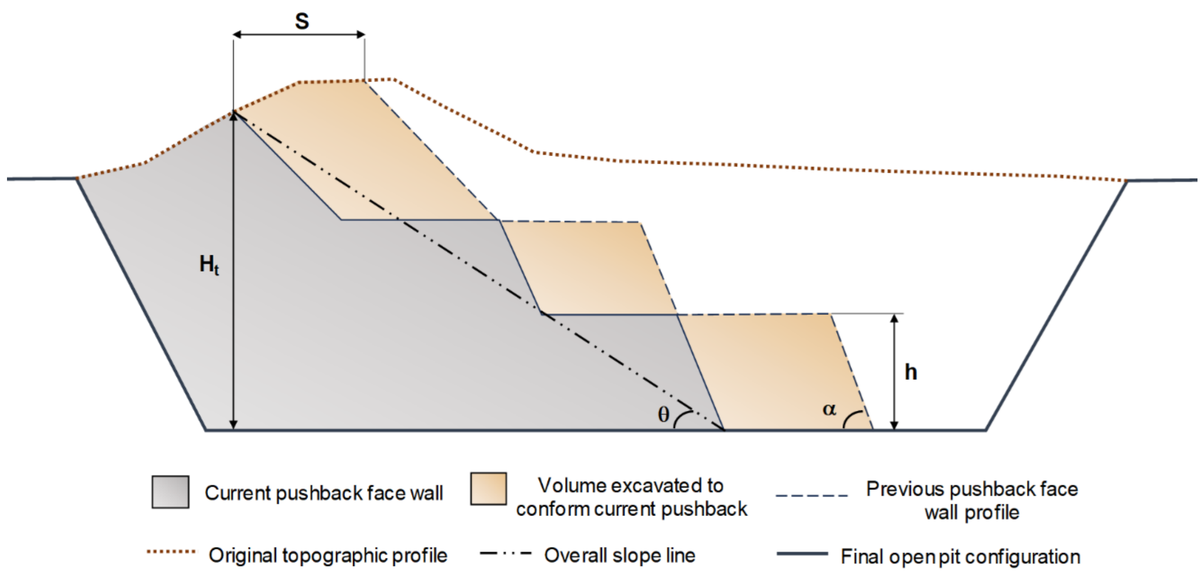

Figure 4-12. Schematic view of the cross profile (B) showing the geometrical parameters to define the modelling trial excavation sequences.

Variations of geometrical parameters such as the batter angle (α) and height (h) defined the geometry for the bench faces, the θ (overall slope angle), and the total height (Ht) for the overall pushback slope. Another geometrical parameter was the separation between successive pushbacks (S). Various combinations of the latter parameters permitted the creation of different trial sequences, each characterised by its unique set of parameters. These sequences could be adjusted to be either generally flatter or steeper, providing a range of scenarios for analysis. Figure 4-13 and Figure 4-14 present the values considered for these geometrical parameters for each pushback in the study. It is easy to observe that trial sequences comprised a range of geometrical features, such as pushbacks' slope total height between 50 and 800 metres, overall slope angle from 5 to 50 degrees, and separations ranging from a few metres to several metres. Trial sequencings also consider two pushback directions, NW and NE. Figure 4-15 presents those sequences indicating their overall inclination degree and mined-out block order.

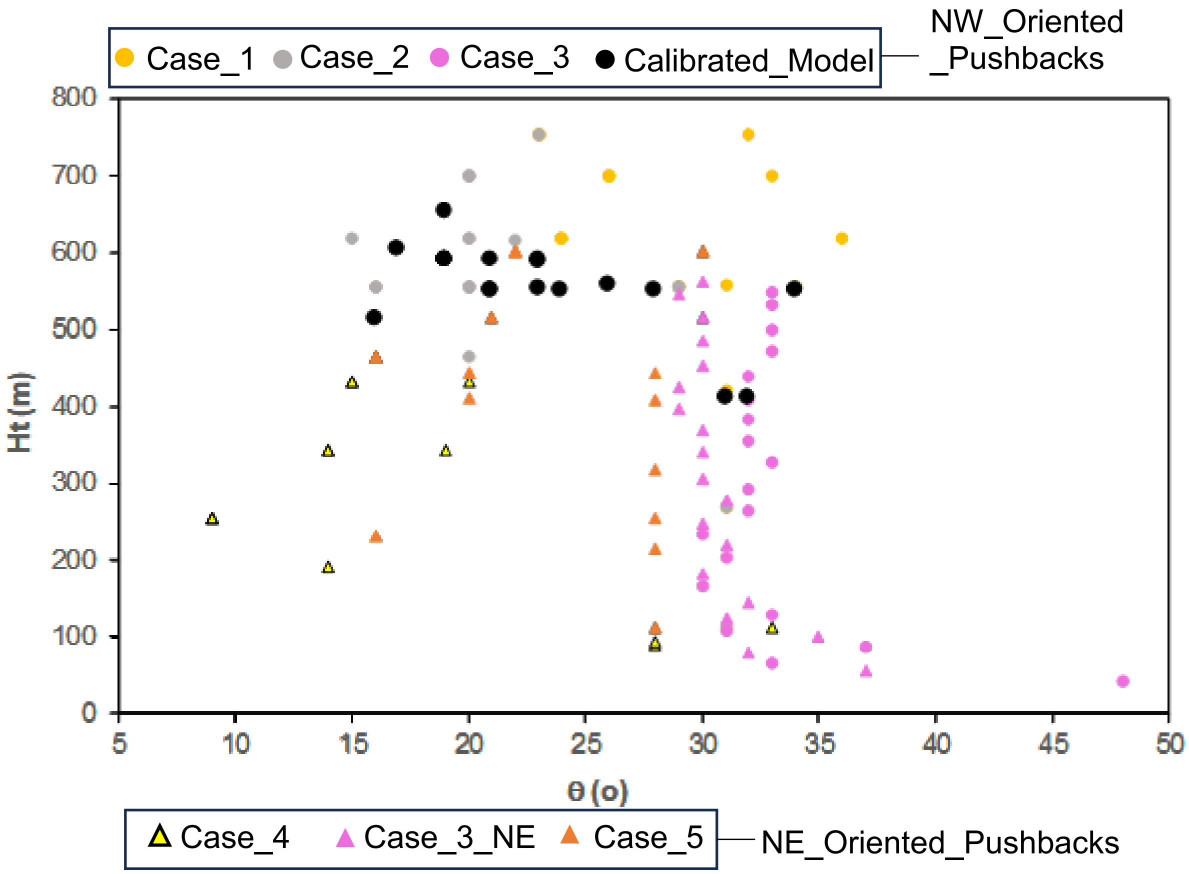

Figure 4-13. Example of the distribution of each theta, Ht pairs that represent individual pushbacks presented in Figure 4-15 for each excavation sequence (Case 1 to Case 5, and Calibrated model inclusive).

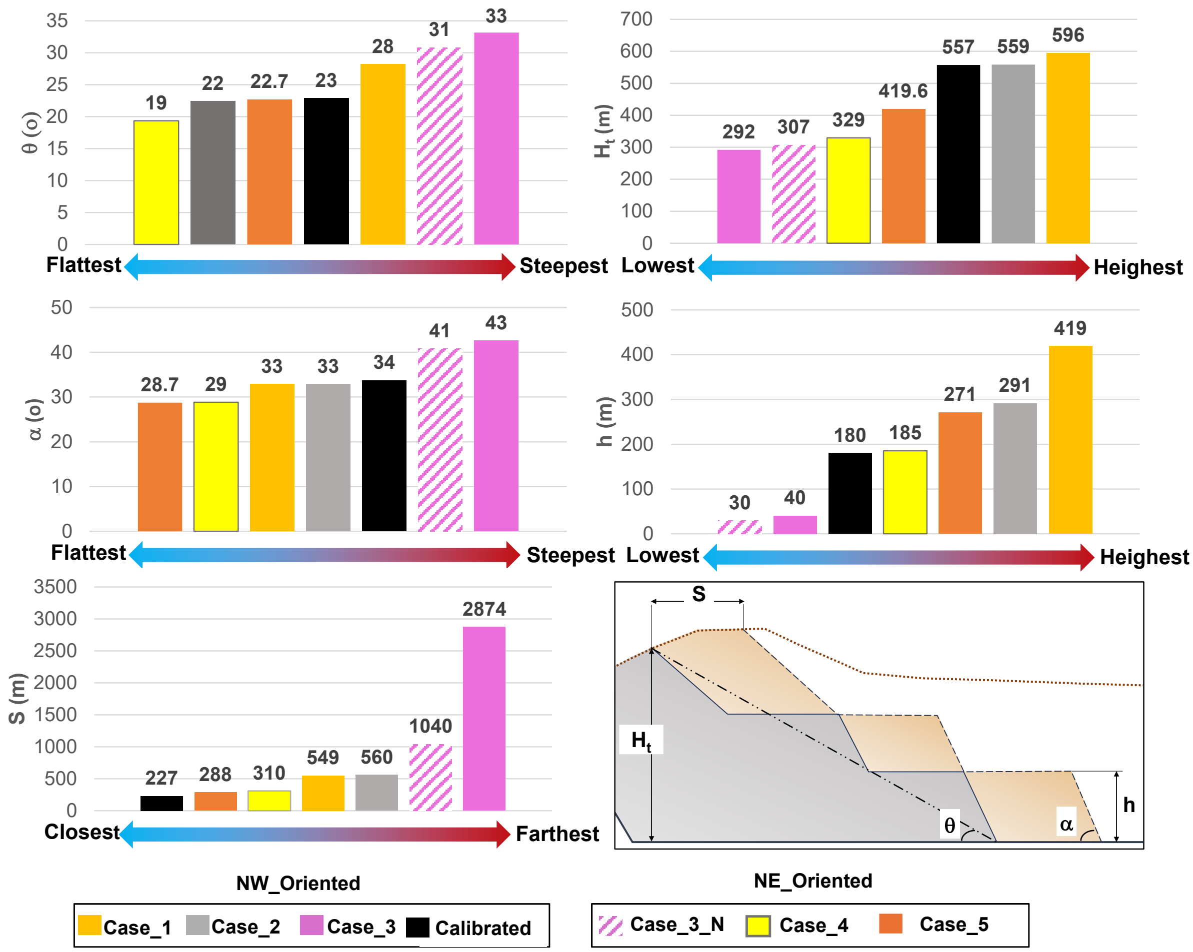

Figure 4-14. Average geometric characteristics for each excavation sequence defined in Figure 4-15.

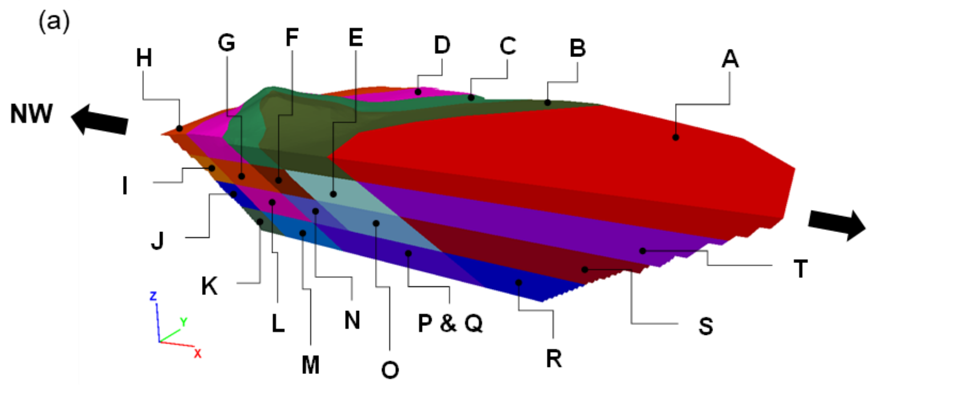

Push-Back	1	2	3	4	5	6	7	8	9	10	11	12	13	14	15	16	17	18	19	
Case_1	A	T	S	R	B	E	O	Q	C	F	N	P	D	G	L	M	H	I	J	K
Case_2	A	T	B	S	R	C	E	O	D	Q	F	H	N	P	G	L	M	I	J	K

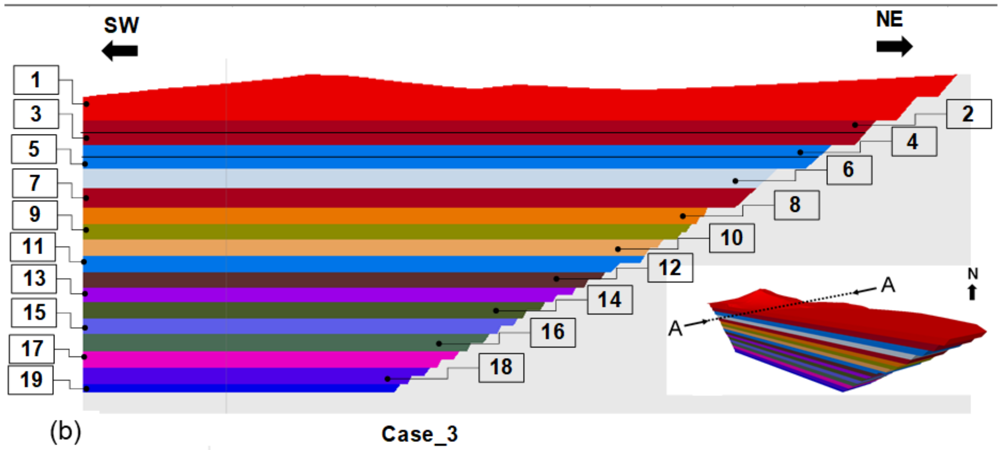

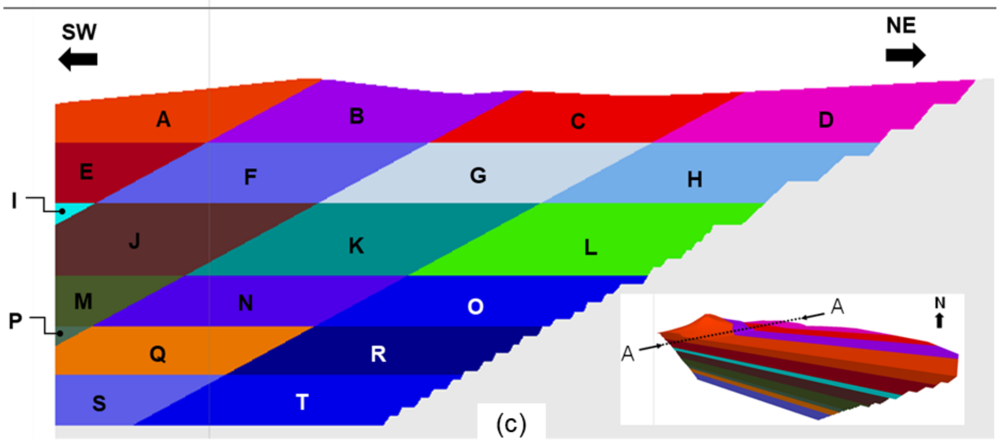

Push-Back	1	2	3	4	5	6	7	8	9	10	11	12	13	14	15	16	17	18	19	
Case_4	A	B	E	C	D	I	F	G	J	H	K	M	L	N	P	O	Q	R	S	T
Case_5	A	E	I	B	F	J	M	C	P	G	K	D	N	Q	S	H	L	O	R	T

Figure 4-15. Trial model sequencings, where excavation order is given by letters in the tables: (a) Isometric view for Case 1 and Case 2, (b) Cross profile and Isometric for Case 3, and (c) Cases 4 and 5. Models built on Rhinoceros 3D V. 7.0., McNeel, R., & others (2020).

4.6 Results and Discussion

As a product of the model calibration using the back-analysis technique to reproduce the failure event depicted in the case study section, the geomechanical (deformational and strength) parameters for the materials early mentioned that best reproduce actual failure are presented Table 4-3. The best failure representation is achieved using peak resistance parameters between 400 and 700 kPa for cohesion, friction between 35 and 45 degrees, and ε_crit of 6.8E-02. Residual strength is characterised by cohesion between 40 and 60 kPa and friction angle between 20 and 25 degrees.

Table 4-3. Geomechanical parameters from back analysis procedure in calibrated model. The failure got through those marked with an asterisk.

Material	Peak (P)				Residual (r)					
	$\phi_{(p)}$ (°)	$C_{(p)}$ (kPa)	ψ (°)	$\sigma_{t\text{-}rm}$ (kPa)	$\phi_{(r)}$ (°)	$C_{(r)}$ (kPa)	ψ (°)	$\sigma_{t\text{-}rm}$ (kPa)	ε_{crit} (–)	$\varepsilon_{95\%}$ (–)
An_Ar	34	439	17	43.9	25	40	0	10		1.0E-04
An_Potassic	38	537	19	53.7	20	40	0	10		1.0E-02
An_Propylitic	37	506	18.5	50.6	20	40	0	10	7.0E-02	1.0E-02
*An_Qz-Ser	41	612	28.7	61.2	19	40	0	10		1.0E-04
*An_Ser-Chl	38	553	19	55.3	20	40	0	10		1.0E-02
*ES_Ar	44	512	30.8	51.2	19	45	0	10		1.0E-03
ES_Potassic	38	483	19	48.3	25	60	0	10		1.0E-04
*ES_Qz-Ser	41	520	28.7	52	26	60	0	10		1.0E-04
ES_Ser-Chl	41	529	20.5	52.9	25	60	0	10		1.0E-02
PZ_Propylitic	37	506	18.5	50.6	25	60	0	10	6.6E-02	1.0E-02
PZ_Ser-Chl	38	553	19	55.3	25	60	0	10		1.0E-02
Rh_Propylitic	45	689	22.5	68.9	25	60	0	10		1.0E-02
Rh_Qz-Ser	43	592	21.5	59.2	25	60	0	10		1.0E-02
Rh_Ser-Chl	45	689	22.5	68.9	25	60	0	10		1.0E-02

$\phi_{(P)}$: peak friction angle, $C_{(P)}$: peak cohesion, $\phi_{(r)}$: residual friction angle, $C_{(r)}$: residual cohesion
ψ: dilation angle, ε_{crit}: plastic critical strain. Strain at which material's resistance reaches residual values, $\varepsilon_{95\%}$: plastic strain where strength presents a 95% loss between peak and residual values.

The model using the above parameters shows a valid response to the excavation sequence followed during operations. As Figure 4-16 shown, the total displacements for the point CP through actual pushback sequencing are within those measured by the mine operators and estimates presented (dashed lines).

Displacements calculated for each scenario pushback sequence reveal that the excavation sequence will influence the timing for initiation and the development of progressive failure, as depicted in the plot Figure 4-16. The curves' colours serve to indicate the overall obtained onset of failure order, from the first to the last: Red (1), Orange (2), Black (3), Yellow (4), Green (5), and Cyan (6).

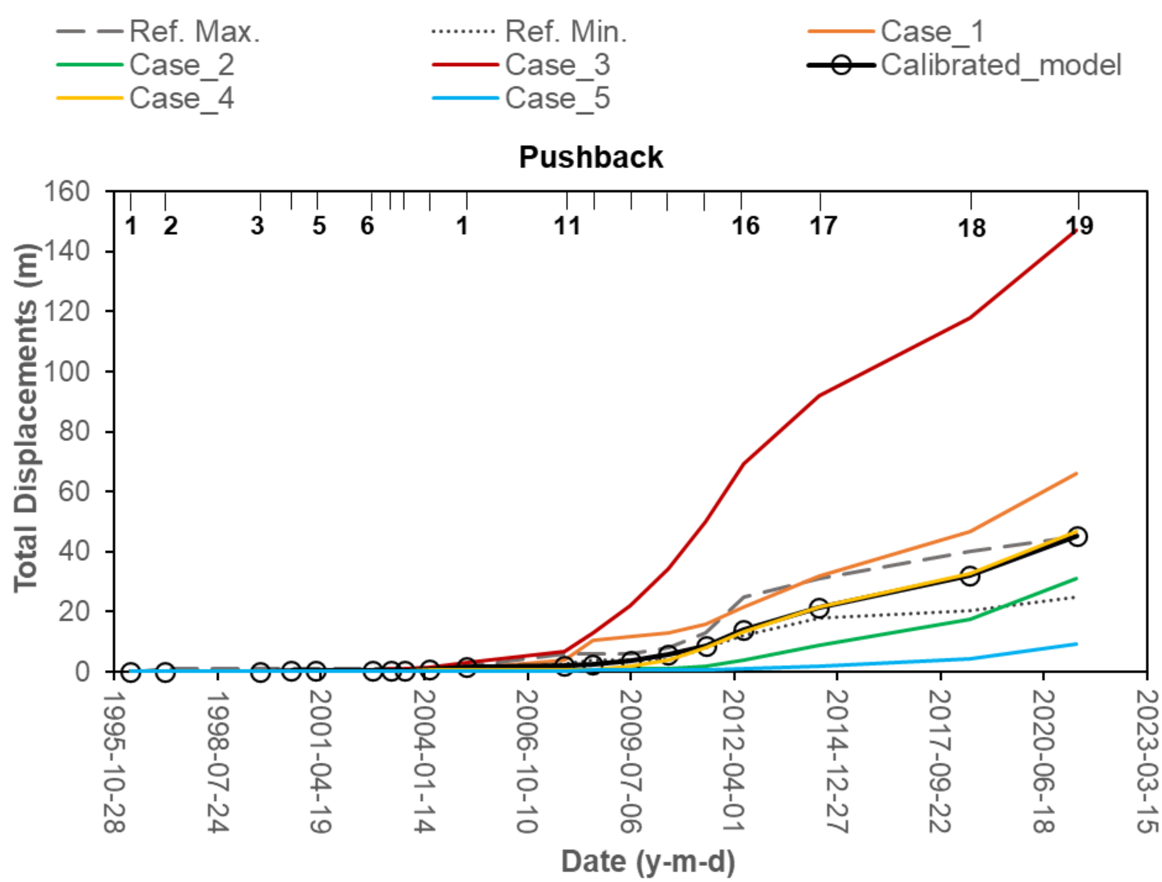

Figure 4-16. Comparative history plots of displacements in a monitoring point located onto failed mass and within failed contour for each pushback sequence model.

Cases one (1) and three (3), characterised by 28 and 33 degrees (the two most steep), accelerate the onset of failure, whereas two (2), four (4) and five (5), opposite to the first mentioned (flatter than the others), delay the occurrence of the failure in this case study.

The same effects are observed for failure magnitude; when the sequencing accelerates the failure occurrence, the surficial extension is larger than that modelled by the calibrated model. The opposite effect is observed when pushback sequencings produce failure delay concerning the calibrated case. Figure 4-17 and Figure 4-18 present the differences in failure magnitude for the different excavation cases, in isometric view and onto the cross profile (A) view, respectively.

Changes in the steepness of the pushback slope face also alter the volume of the affected area on the slope. This volume ranges from 1E+7 to 5.5E+7 m3 as the pushback faces become steeper, as shown in Figure 4-19. Additionally, models reveal for any sequencing; the required excavated volume must range between 70% to 90% of the open pit's total excavated material for failure to occur. This suggests that a minimum deconfinement and exposure of geological features are required to fail the excavation (Figure 4-20). Table 4-4 presents details for each excavation sequence and for the calibrated model, regarding onset of failure time, amount of pit's excavated material, the total volume that reaches the failed mass, overall slope angle in pushbacks, and pushbacks orientation.

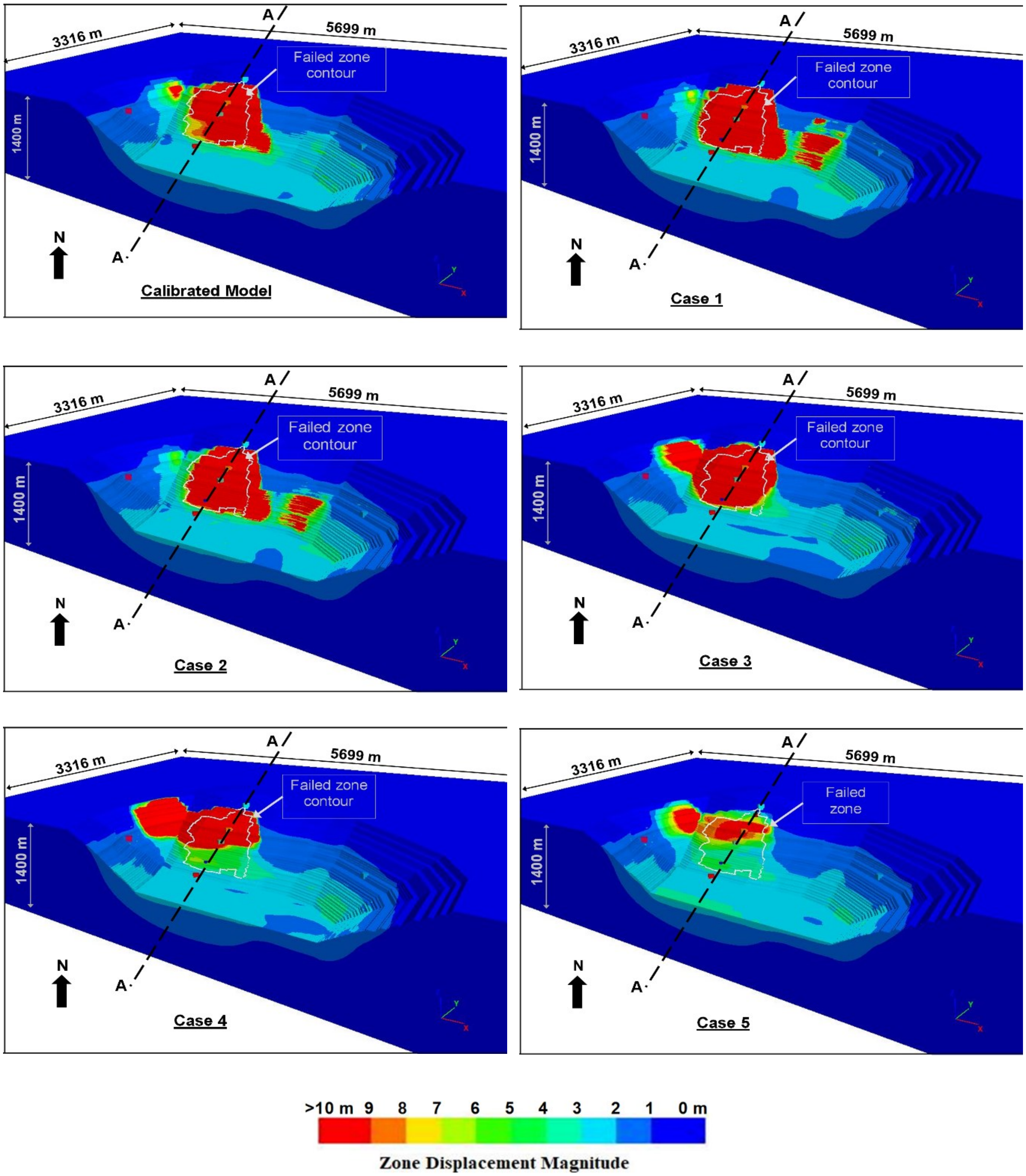

Figure 4-17. Isometrical view shows each modelled case's failure extension at the final stage (Pushback 19). Results from FLAC3D V. 7.0., Itasca Consulting Group, Inc (2019).

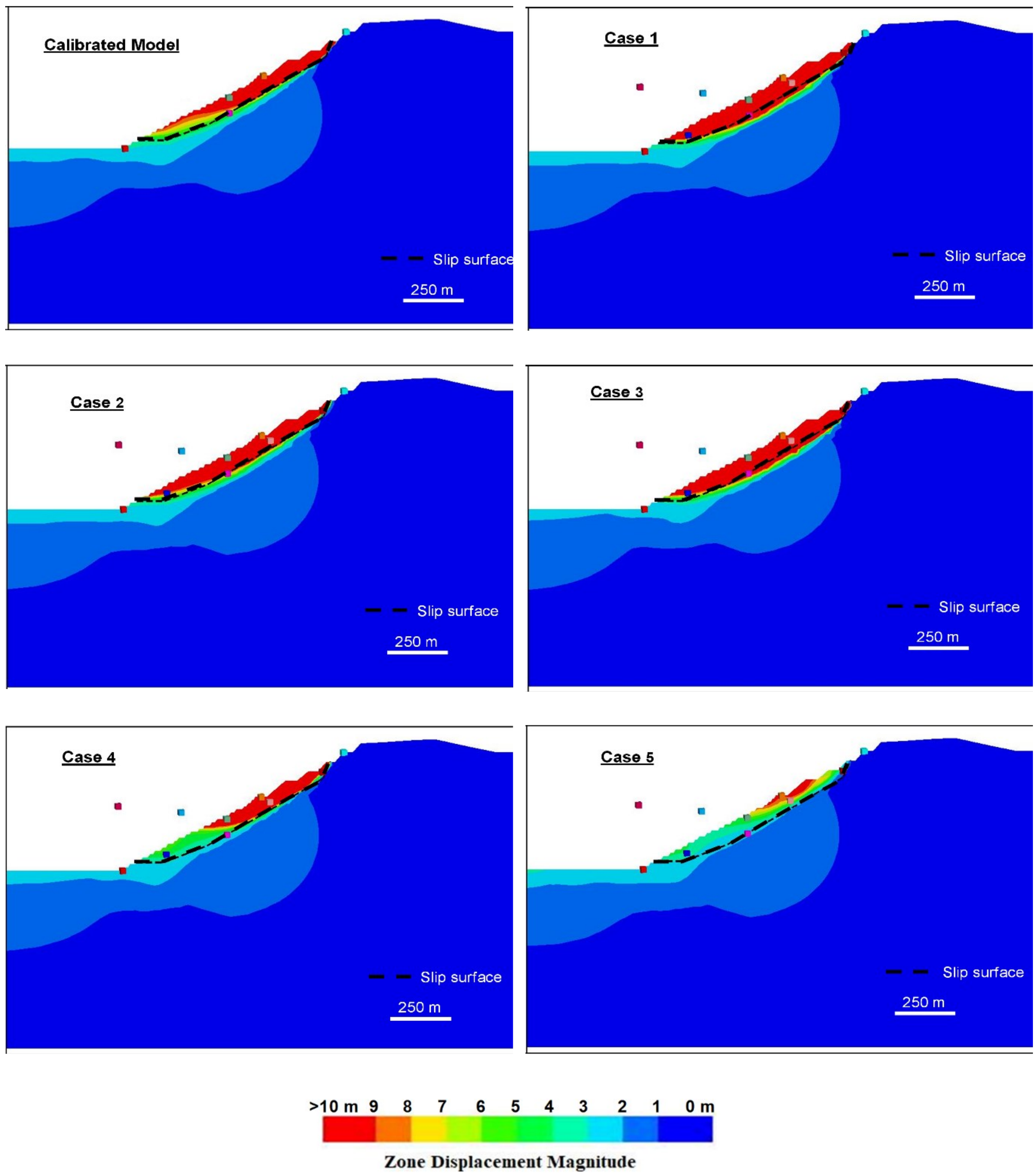

Figure 4-18. Cross profile (A) view showing the failure depth, extension, and shape achieved by each modelled case at the final stage (Pushback 19). Results from FLAC3D V. 7.0., Itasca Consulting Group, Inc (2019).

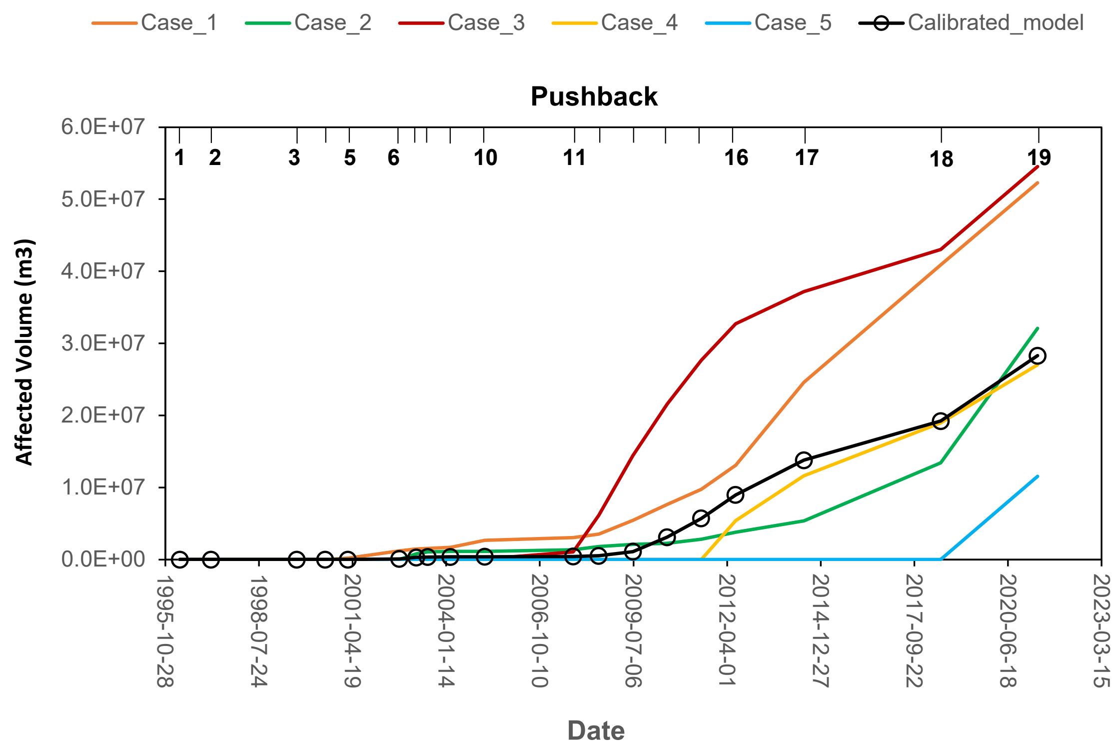

Figure 4-19. History plots of each excavation sequence case showing how the involved in the failure material at the actual failed site evolves throughout pushbacks.

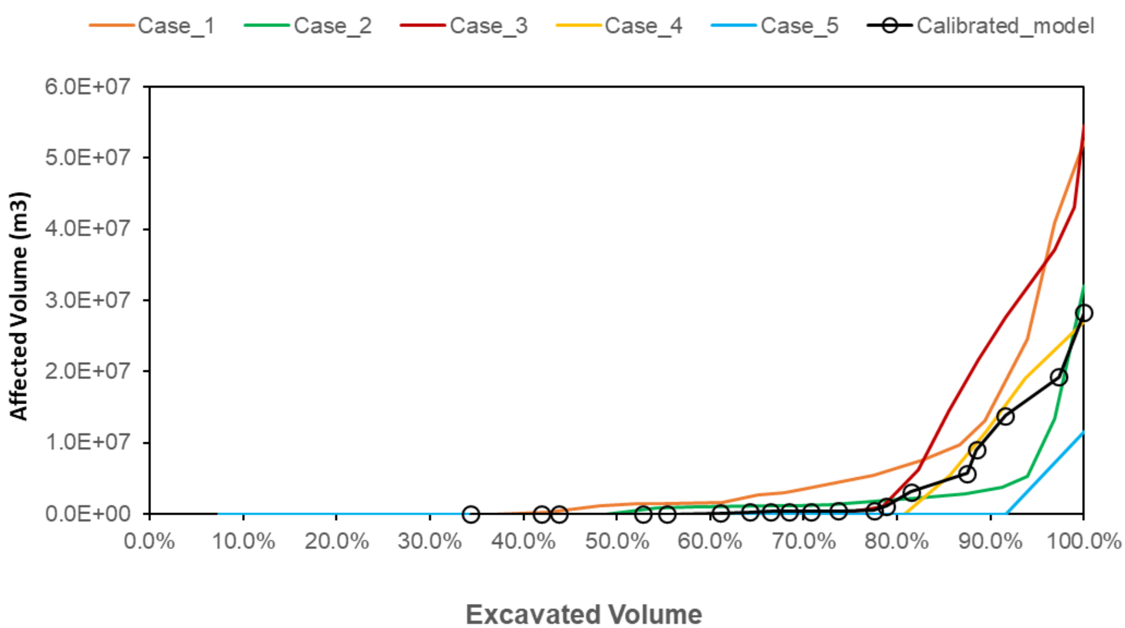

Figure 4-20. Comparative plots between the excavated material volume in percentage versus the unstable volume generated (affected volume) for each excavation sequence.

Table 4-4. Summary of results involving the onset of failure timing, the pushback orientation, pushback inclination degree, and comparatives between the required excavated material (ore extracting) to the onset of failure and the maximum involved volume in the failure.

Sequencing	Onset of failure date (Pushback number)	Excavated volume from total (%). at the onset time	Max. Involved in Failure volume (m3)	Average Pushback face angle (o)	Pushback direction
Case_1	7/1/2008 (12)	70	5.23E+07	28	NW
Case_2	7/1/2012 (16)	91	3.21E+07	22	NW
Case_3	10/1/2007 (11)	78	5.46E+07	31 for NE, 33 for NW	NE, NW
Case_4	7/1/2011 (15)	81	2.7E+07	19	NE
Case_5	7/1/2018 (18)	92	1.16E+07	22.7	NE
Calibrated_Model	7/1/2009 (13)	79	2.83E+07	23	NW

Figure 4-21 presents the pit's excavated volume history plots per excavation sequence and calibrated model inclusive and uses the same colour convection to depict the overall failure order. Coloured dots along with upper and lower horizontal axis, pushbacks, and date axis respectively, allow to identify the onset of failure time and order among all the analysed cases. Usually, the curves show a clear trend before reaching failure points: they start gently, then become steeper, and finally level off. Dashed lines mark parts of the curves where the slope is steeper, indicating faster excavation rates in cubic meters per day. The inset in the figure compares slopes of dashed lines and allows to stablish a relationship between excavation rate and the overall failure order already depicted in previous figures such as Figure 4-16.

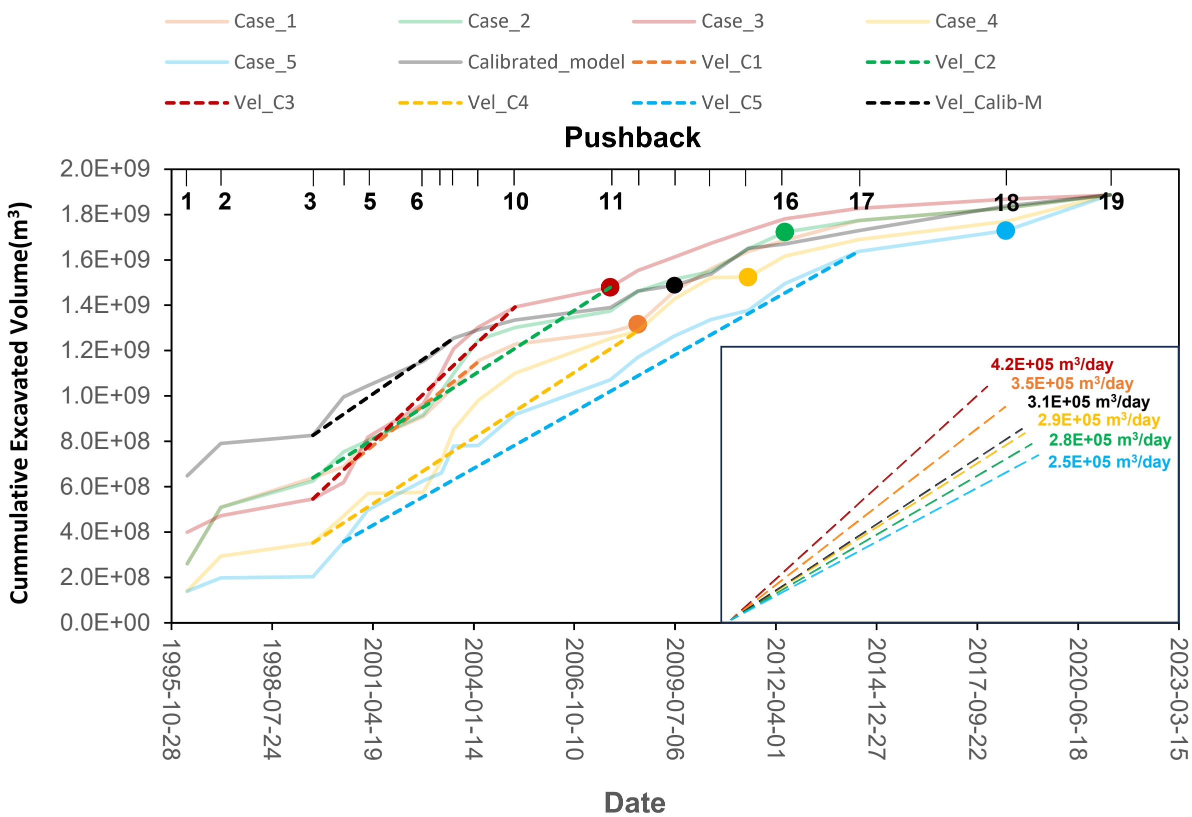

Figure 4-21. History plot of the excavated material throughout the nineteen (19) pushbacks for each excavation sequence defined in Figure 4-15, and their maximum excavation rate (dashed lines) before the onset of failure (dots).

As depicted by the same figure inset, faster excavation rates, like those for case 1 (orange dashed line) and case 3 (red dashed line), with paces of 3.5E+05 m3/day and 4.2E+05 m3/day, also contribute to the onset of failure at an earlier time.

The different excavation sequences also impacted the magnitude and distribution of stresses within the rock mass. Figure 4-22 portrays six (6) stress paths from a monitoring point (MS-2 point) within the failed mass throughout the nineteen (19) excavation stages (indicated as triangular dots, with the pushback number indicated). These paths are depicted on principal stress spaces for each case of excavation sequencing, with the inclusion of the calibrated model. Each plot incorporates the Mohr-

Coulomb shear strength peak and residual envelope for materials where the slip surface develops, denoted as An_Qz-Ser and Es_Ar.

The plots unveil that each excavation sequence case reaches the peak resistance envelope at distinct pushback stages. Before reaching that point, the lengths and shapes of the stress paths differ from case to case.

Table 4-5 shows that the order (from the earliest to the latest) at which each sequencing onset of failure occurs, is as follows: Case 3, Case 1, Calibrated model, Case 4, Case 2, and Case 5. Outcomes regarding the pushback direction significantly impact case study failure development. On the other hand, pushback faces geometrical parameters, such as the overall slope angle (θ) and the pushback's separation (S), shows an explicit relationship with the failure order. On average, the steeper the overall slope (θ), the faster and larger the failure develops. Excavation velocity also plays a crucial role in progressive failure acceleration and intensification, as the quicker ore body extraction, the more likely it is to affect progressive failure development.

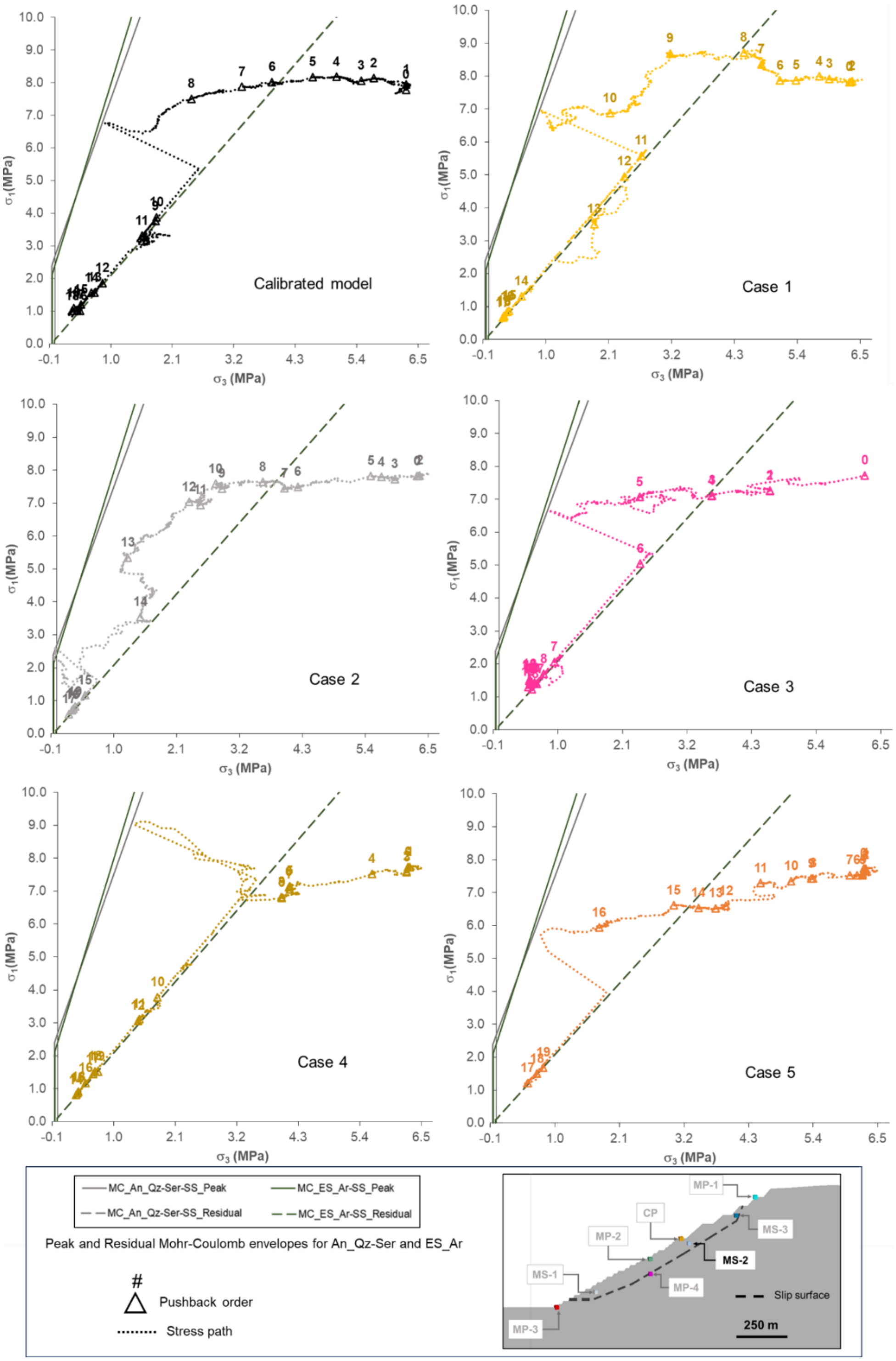

Figure 4-22. Stress paths from the MS-2 monitoring point across nineteen (19) excavation stages, displayed on principal stress spaces with pushback sequencing and a calibrated model. Each plot includes the Mohr-Coulomb shear strength envelopes for slip surface materials involved in failure.

Table 4-5. Summary of trial model geometrical characteristics with failure order (onset of failure).

Failur e order	Pushbac k Dir.	Average Values									
		NW					NE				
	Model	H_t (m)	θ (º)	h (m)	α (º)	S (m)	H_t (m)	θ (º)	h (m)	α (º)	S (m)
1	Case_3	292	33	40	43	2874	307	31	30	41	1040
2	Case_1	596	28	419	33	549	-	-	-	-	-
3	Calibrated	557	23	180	34	227	-	-	-	-	-
4	Case_4	-	-	-	-	-	329	19	185	29	310
5	Case_2	559	33	291	33	560	-	-	-	-	-
6	Case_5	-	-	-	-	-	420	23	271	29	287

Figure 4-23 shows all the excavation sequences' pushbacks in terms of their overall height and slope, and grouped in whether they produce instabilities (red colour) in the NE wall or not (green colour). Pushback direction is depicted by dots shape, where circular ones indicate NW direction and triangular shaped NE pushback direction. Points are distributed in such way that a dashed curve line fits in the boundary between unstable and stable points. The fitted curve is similar in shape to that from other authors, like for example the one from empirical work from Lutton (1970) and Hoek and Bray (1981), called stability line, from observed distribution of walls stability in cooper deposit pits according to their overall wall geometry; see black and hollow dots in Figure 4-23. As cited by Sjöberg (2001), Such stability charts almost never coincide with each another, as it is difficult to convey factors such as pore pressure, specific geological characteristics or structural control in these charts. Therefore, the use of general charts is not conservative, and it must be done on a site characteristics assessment basis.

Certain combinations of height and slope angle can lead to pushback faces that are either steeper or flatter. This can decrease support for certain parts of the northeast (NE) wall or expose weaker materials sooner, potentially leading to instability.

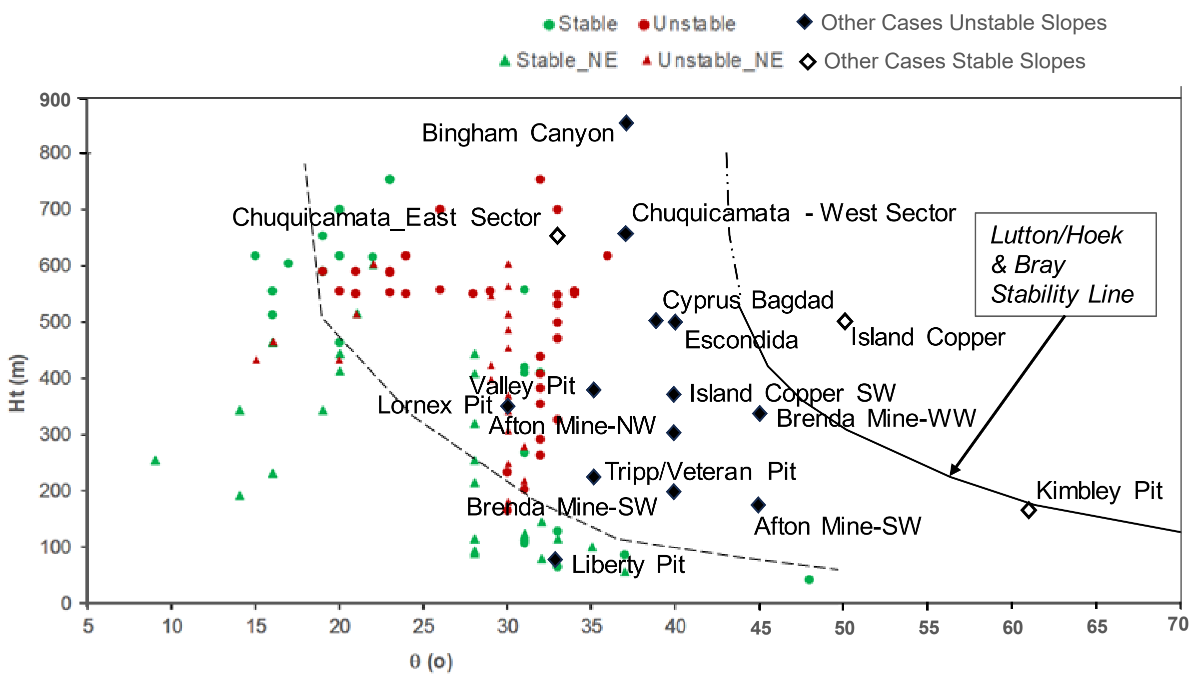

Figure 4-23. Distribution of excavation sequence cases pushbacks according to their overall height and slope (represented by dots), and group them according whether they inflict instabilities (red colour) on NE wall or not (green colour).

Figure 4-24 provides insights into the combinations of pushback height (Ht) and slope angle (θ) that resulted in the least and most NE wall material being involved in the failure. It is worth to remember that each dot in the figure represents individual pushbacks comprising the defined scenarios from case 1 to 5, and the calibrated model, and making a distinction between pushback orientation. Colours in Figure 4-24 (b) represent the generated failure volumes. The highest affected volumes are in the range of 450 m >Ht>600 m, and 30 > θ > 35. The majority of Ht and θ pairs that produce the most significant affectation in volume on the NE wall correspond to pushbacks of case 3, which has the higher average overall pushback slope angle and ore extraction rate (see Figure 4-14 and Figure 4-21). This suggests that these factors accelerate the onset of failure.

Additionally, consider that Case 3 involves a top-down excavation approach, fully exposing the northeast (NE) wall from its southeast (SE) to northwest (NW) ends. This means that weaker materials are visible earlier in the process compared to other excavation sequences. In simpler terms, there are more opportunities for plastic strain accumulation, especially with larger Ht values in Case 3. This clarifies why in Figure 4-24 (b), for the same θ value, as we increase Ht values from lower to upper ranges, the affected volumes initially increase, then decrease back to their previous levels. This indicates that the excavation geometry together with the location of weaker materials will define the timing and extent of failure, which can be best understood through scenario analyses of excavation sequences.

Figure 4-25 compares stress paths from the different sequencing scenarios. The principal stress space with the trajectories reveals that most sequence scenarios induced failure in the NE wall. A key observation is that the shorter the stress path distance before reaching the peak strength envelope, the sooner the NE wall develops a failure state (sooner in terms of the amount of deconfinement required, which is sequence-dependent). Furthermore, Figure 4-26 allows us to determine the onset of failure more precisely. We track stress states during excavation sequencing to pinpoint when the rock mass enters post-peak strength behaviour and experiences irreversible deformations. Figure 4-22 illustrated the timing of stress paths reaching the peak envelope in terms of excavation sequence. Figure 4-26 illustrates when failures occur during excavation stages and how they correlate with slope geometry characteristics. This figure compiles ranges of pushback numbers where failure onset happens, linked to key pushback sequencing characteristics: θ, Ht, and excavation rate. In this case study, correlations indicating failure onset are not tied to pushback sequencing orientation but are influenced by pushback geometry and site-specific factors, as shown in Figure 4-24.

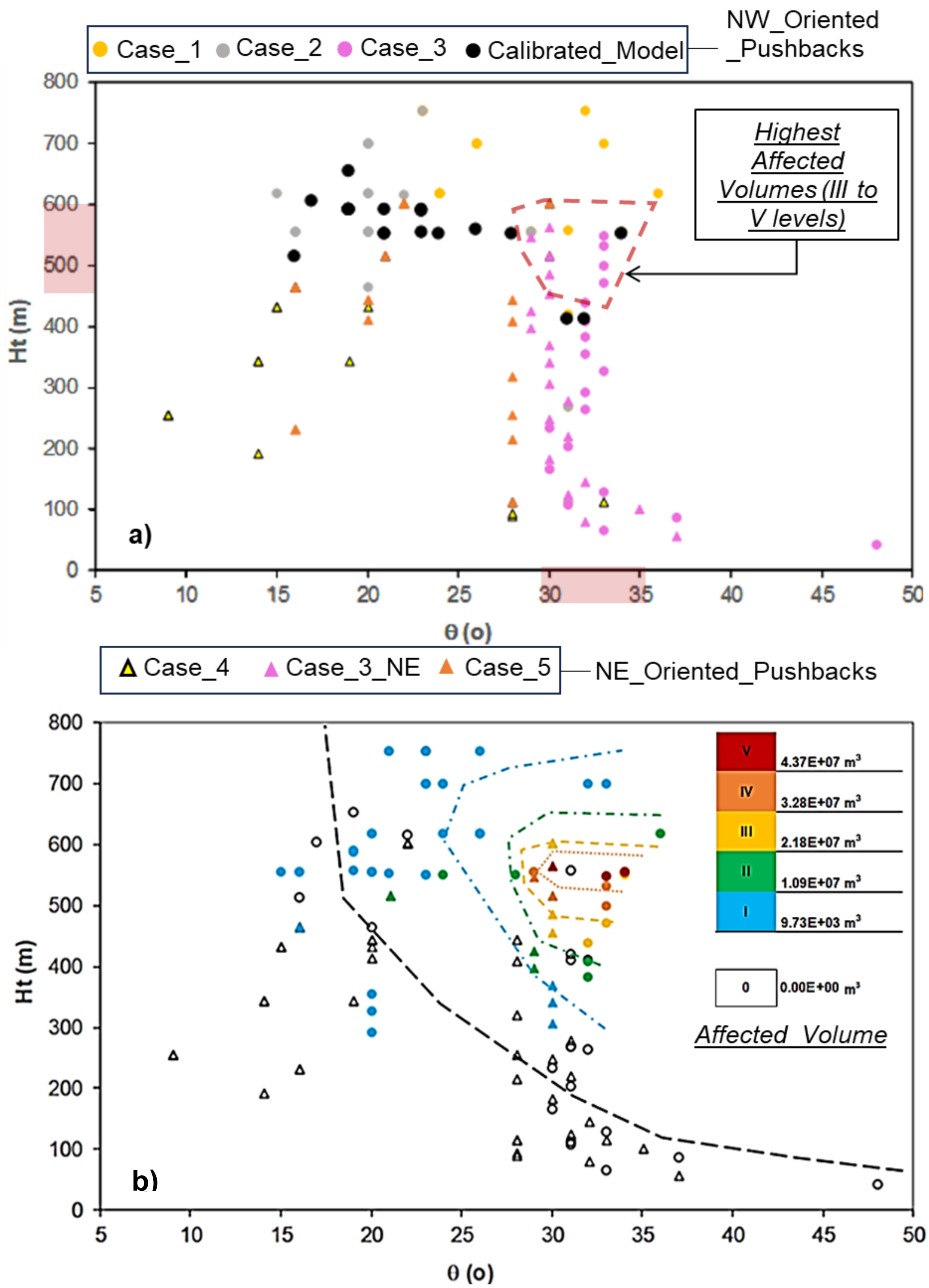

Figure 4-24. a) Ht and theta pairs according to case groups and pushback orientation, b) Ht and θ pairs distribution with affected volume on NE wall (colours) and stability line (separation between stable and unstable pushback individual cases).

Figure 4-26 supports the hypothesis from Figure 4-1, yet it does not clarify which factors hold greater influence. It's plausible to suggest that excavation sequences featuring steeper walls and benches, greater distance between pushbacks, and faster excavation rates are more susceptible to earlier and localised progressive failure when compared to those with opposite characteristics.

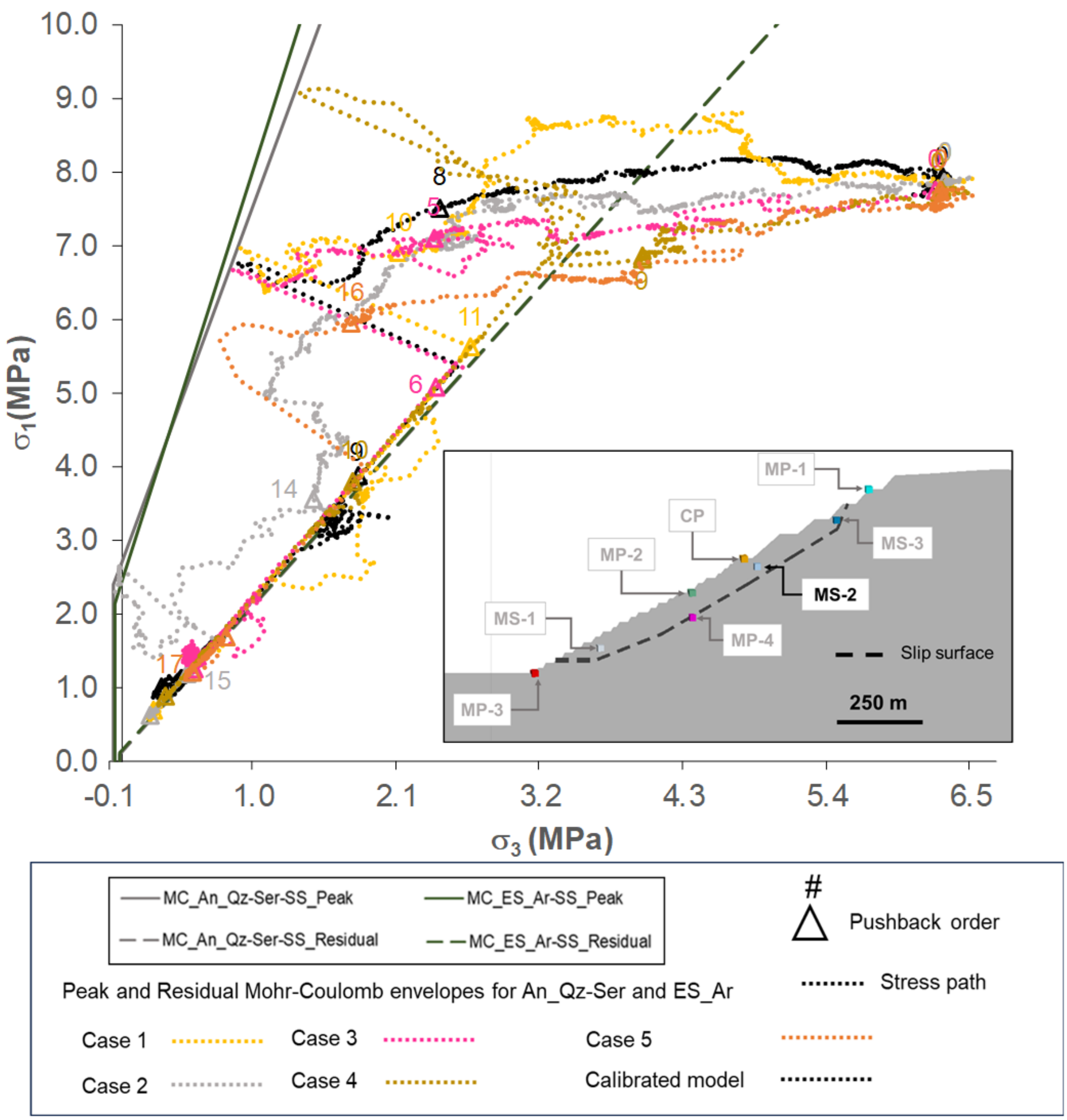

Figure 4-25. Stress path envelope for all the evaluated cases.

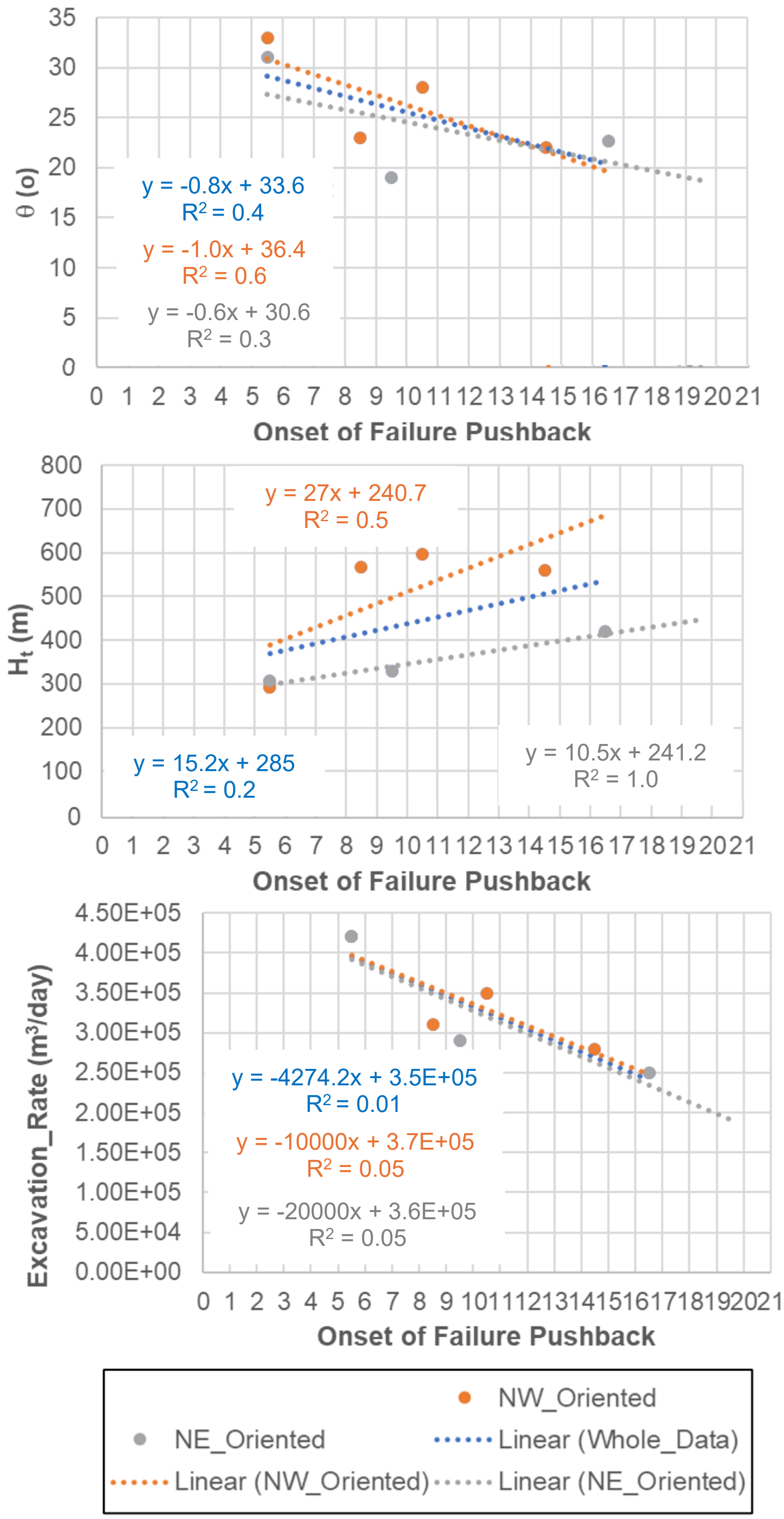

Figure 4-26. Effects of pushback average geometric characteristics (θ, and Ht,), orientation, and excavation sequence rate on the onset of failure order.

4.7 Conclusion

This paper presents a study on how excavation sequences influence large-scale progressive failure in rock slopes for a deep open pit mine (over 500 meters depth according to Li et al., 2022). The method presented can assess excavation sequences to reduce or delay the likelihood of slope failure and can inform decision-making regarding sequencing that considers access to the ore within a mine plan and slope management. The conclusions drawn from this study are:

- The geomechanical parameters calibrated through back-analysis provide an accurate representation of failure, with cohesion between 400 and 700 kPa, friction angle between 35 and 45 degrees, and ε_crit of 6.8E-02.
- Excavation sequencing significantly affects the timing and magnitude of progressive failure, with steeper sequences accelerating failure onset while flatter sequences delay it. This was expected; however, this work has quantified this influence for a case study.
- The excavation rate plays a crucial role, with faster rates contributing to earlier failure onset.
- Top-down excavation approaches, like Case 3, expose weaker materials earlier (in this case study geological setting), accelerating failure.
- Stress path analysis reveals that the timing of failure onset is closely linked to the length of stress paths before reaching peak strength, indicating the importance of excavation sequence in determining failure initiation.
- The study confirms the hypothesis presented in Figure 4-1, suggesting that excavation sequences with specific geometric characteristics and rates significantly influence the timing and localisation of progressive failures in rock slopes.
- Pushback geometry and orientation influence failure characteristics, with steeper walls and benches, greater distances between pushbacks, and faster excavation rates making slopes more prone to earlier and localised progressive failures, and potentially

leading to larger failure volumes.

This study illustrates the gains in conducting sensitivity studies on pit slope excavation sequencing to enhance the design and optimisation process, particularly for critical sectors of a pit operation. This study underscores the importance of considering excavation sequencing effects on slope stability in pit design and optimisation, providing valuable insights for mitigating progressive failure risks.

4.8 Acknowledgements

The authors would like to acknowledge the financial support from the Large Open Pit (LOP) project (https://www.lopproject.com).

Chapter 5

Conclusion and Future Work Recommendations

The presented thesis emphasises the relevance of Geological-Material Model Complexity Level and Excavation Sequencing in Numerical Modelling of large-scale Progressive Failure in Deep Open-Pit Slopes (over 500 meters depth according to Li et al., 2022) through a complete case study in a Porphyry Deposit Mine. The project examines how geological model complexity and excavation sequencing affect the accuracy of numerical modelling of progressive failure on large open-pit slopes.

Conclusions: Based on the extensive analyses performed in this study, the following conclusions can be drawn:

1- Geological-Material Model Complexity Level Impact: Incorporating geological complexity into numerical models is crucial for effectively anticipating progressive failure in open-pit slopes, according to the study's findings.

Among the numerous models examined, the Lit+Alt-SS model, which incorporates lithologies and their alterations, displayed the best-predicted accuracy.

The Lit+Alt-SS model reproduced not only the reported failure zone's position, form, and depth but also surface area, failed volume, and slip surface depth.

The calibrated strength and strain parameters for the Lit+Alt-SS model were consistent with typical values reported for porphyry deposit lithologies, confirming the modelling approach's suitability.

2- Excavation Sequencing Influence on Progressive Failure Development: The study emphasised the importance of excavation sequencing in determining the time and extent of progressive collapse in open-pit slopes.

Different pushback sequences accelerated or delayed failure initiation, with commensurate impacts on failure amplitude and extent.

The excavation sequence affected the stress distribution inside the rock mass, influencing the beginning and spread of failure down the slope.

Pushback geometrical characteristics, such as overall slope angle and spacing, demonstrated apparent connections with the beginning and development of failure. Steeper faces hasten failure, while longer separations delay it.

The study shed light on techniques to reduce slope instability hazards in open-pit mining operations by examining the interaction between pushback geometry and excavation sequencing.

Further research work:

a- Temporal Analysis of Progressive Failure: Investigate the temporal evolution of progressive failure in deep open-pit slopes by analysing historical data and monitoring systems. Explore the influence of excavation sequencing and geological-material model complexity on the timing and progression of slope instability events.

b- Effect of Hydrogeological Factors: Assess the impact of hydrogeological conditions on progressive failure in open-pit slopes. Investigate how variations in groundwater levels, pore pressures, and drainage systems influence the stability of slopes under different excavation sequences and geological settings.

c- Advanced Geomechanical Modelling Techniques: Develop and apply advanced geomechanical modelling techniques, such as coupled hydro-mechanical modelling or discrete element method (DEM) simulations, to enhance the accuracy of numerical modelling for predicting progressive failure in deep open-pit slopes.

d- Risk Assessment and Management Strategies: Develop comprehensive risk assessment methodologies and management strategies for mitigating progressive failure hazards in deep open-pit slopes. Consider factors such as uncertainty in geological data, operational practices, and the implementation of early warning systems.

e- Case Studies in Different Geological Settings: Conduct comparative case studies in diverse geological settings to evaluate the transferability and generalizability of findings from the initial case study. Explore how variations in geology, climate, and mining practices affect the predictability and management of progressive failure in open-pit slopes.

f- Influence of Blast Design and Excavation Techniques: Investigate the influence of blast design parameters, such as blast-hole spacing, drilling patterns, and explosive types, on the initiation and propagation of progressive failure in open-pit slopes. Evaluate the effectiveness of alternative excavation techniques in minimising slope instability risks.

g- Long-Term Monitoring and Performance Evaluation: Implement long-term monitoring programs to track slope deformation, groundwater conditions, and operational changes over extended periods. Evaluate the performance of numerical modelling predictions against observed data to refine modelling approaches and improve slope stability assessments.

h-Automation of Back Analysis Technique: Develop automated procedures for conducting back analysis of progressive failure events in open-pit slopes. Explore machine learning algorithms and optimisation techniques to streamline the calibration process, reduce manual intervention, and enhance the efficiency and reliability of numerical modelling studies.

i- Exploration of Advanced Constitutive Models: Investigate alternative constitutive models, such as non-linear viscoelasticity, elastoplasticity with strain softening, or damage mechanics, to improve the representation of progressive failure mechanisms in numerical simulations. Evaluate the ability of these advanced models to capture complex behaviour, including strain localisation, brittle fracturing, and post-failure deformation.

j- Impact of Faults and Discontinuities: Examine the influence of geological structures, such as faults, joints, and minor discontinuities, on the initiation and propagation of progressive failure in deep open-pit slopes. Incorporate detailed representations of structural features into numerical models and assess their effects on slope stability under various excavation sequences and loading conditions.

Bibliography

Ahmed, S., & Hawlader, B. (2016). Numerical analysis of large-diameter monopiles in dense sand supporting offshore wind turbines. *International Journal of Geomechanics, 16*(5), 04016012. https://doi.org/10.1061/(ASCE)GM.1943-5622.0000633

Ai, Z., Zhang, H., Wu, S., Jiang, C., Yan, Q., & Ren, Z. (2022). Study on the slope dynamic stability considering the progressive failure of the slip surface under earthquake. *Frontiers in Earth Science, 10*, Article 981503. https://doi.org/10.3389/feart.2022.981503

Alejano, L. R., Arzúa, J., Bozorgzadeh, N., & Harrison, J. P. (2017). Triaxial strength and deformability of intact and increasingly jointed granite samples. *International Journal of Rock Mechanics and Mining Sciences, 95*, 87–103. https://doi.org/10.1016/j.ijrmms.2017.03.009

Álvarez Avendaño, I. J. (2018). *Propuesta de túneles de drenaje en el rajo Escondida y su caracterización geológica-geotécnica* [Master's thesis, Universidad de Chile]. Repositorio Académico Universidad de Chile. https://repositorio.uchile.cl/handle/2250/169229

An, X., Ning, Y., Ma, G., & Liu, H. (2013). Modeling progressive failures in rock slopes with non-persistent joints using the numerical manifold method. *International Journal for Numerical and Analytical Methods in Geomechanics, 38*(7), 679–701. https://doi.org/10.1002/nag.2226

Araya, A., Nehring, M., Vega, E., & Miranda, N. (2020). The impact of equipment productivity and pushback width on the mine planning process. *Journal of the Southern African Institute of Mining and Metallurgy, 120*(10), 583–591. https://doi.org/10.17159/2411-9717/1256/2020

Attene, M., Campen, M., & Kobbelt, L. (2013). Polygon mesh repairing: An application perspective. *ACM Computing Surveys, 45*(2), Article 15, 1–33. https://doi.org/10.1145/2431211.2431214

Aziz, O., Al-Samarrai, T., & Al-Hakari, S. (2019). Structural and rock slope stability assessment of some sites along Sirwan Road, Sulaimaniyah Governorate, northeast Iraq. *Iraqi Journal of Science, 60*(6), 1304–1311. https://doi.org/10.24996/ijs.2019.60.6.14

Azmi, N., & Yu, Z. (2023). A comprehensive overview of rock strength of Karak Highway affected by tectonic settings [Preprint]. https://doi.org/10.21203/rs.3.rs-3059305/v1

Bagdasaryan, A., & Sytenkov, V. (2014). Change in the pitwall stability with depth. *Journal of Mining Science, 50*(1), 65–68. https://doi.org/10.1134/S1062739114010104

Bakhtiyari, E., Almasi, A., Cheshomi, A., & Hassanpour, J. (2017). Determination of shear strength parameters of rock mass using back analysis methods and comparison of results with empirical methods. *European Journal of Engineering and Technology Research, 2*(11), 35–39. https://doi.org/10.24018/ejers.2017.2.11.518

Becker, S., Fall, A., & Bodnar, R. (2008). Synthetic fluid inclusions. XVII. PVT properties of high salinity H_2O-NaCl solutions (>30 wt % NaCl): Application to fluid inclusions that homogenize by halite disappearance from porphyry copper and other hydrothermal ore deposits. *Economic Geology, 103*(3), 539–554. https://doi.org/10.2113/gsecongeo.103.3.539

Bewick, R., Brzovic, A., Rogers, S., Griffiths, C., & Otto, S. (2022). Benchmarking framework for porphyry copper-gold rock masses for caveability and fragmentation decision-making. *Proceedings of the Caving 2022: Fourth International Symposium on Block and Sublevel Caving*. https://doi.org/10.36487/acg_repo/2205_91

BHP. (2012). *Escondida site visit presentation*. BHP. https://www.bhp.com/-/media/bhp/documents/investors/reports/2012/121001_escondida-site-visit-presentation.pdf

Borges, R., Bacellar, L., Grasso, C., Gomes, G., & Gomes, R. (2023). Slope geometry optimization considering groundwater drawdown scenarios at an open-pit phosphate mine, southeastern Brazil. *Environmental Earth Sciences, 82*(7), Article 10855. https://doi.org/10.1007/s12665-023-10855-w

Bouajaj, A., Bahi, L., Ouadif, L., & Baba, K. (2016). A methodology based on GIS for 3D slope stability analysis. *International Journal of Engineering and Technology, 8*(5), 2259–2264. https://doi.org/10.21817/ijet/2016/v8i5/160805061

Bowa, V., & Gong, W. (2021). Analytical technique for stability analyses of the rock slope subjected to slide head toppling failure mechanisms considering groundwater and stabilization effects. *International Journal of Geo-Engineering, 12*(1), Article 1. https://doi.org/10.1186/s40703-020-00133-0

Broadbent, C. D., & Zavodni, Z. M. (1982). Influence of rock structure on stability. In Hustrulid, W. (Ed.), *Proceedings of the 3rd International Conference on Stability in Surface Mining* (pp. 7–18). Society of Mining Engineers, A.I.M.E.

Brown, E. T., Potvin, Y., Carter, J., Dyskin, A., & Jeffrey, R. (2008). Estimating the mechanical properties of rock masses. In Y. Potvin (Ed.), *Proceedings of the First Southern Hemisphere International Rock Mechanics Symposium* (pp. 3–22). Australian Centre for Geomechanics. https://doi.org/10.36487/ACG_repo/808_16

Brown, I., Wood, P., & Elmouttie, M. (2016). Estimation of in situ strength from back-analysis of pit slope failure. In *A. B. Fourie & M. Tibbett (Eds.), Proceedings of the 12th International Symposium on Field Measurements in Geomechanics* (pp. 221–232). Australian Centre for Geomechanics. https://doi.org/10.36487/acg_rep/1604_18_brown

Burlon, S., Mroueh, H., & Shahrour, I. (2013). Influence of diaphragm wall installation on the numerical analysis of deep excavation. *International Journal for Numerical and Analytical Methods in Geomechanics, 37*(11), 1670–1684. https://doi.org/10.1002/nag.2159

Busto, S., Río-Martín, L., Vázquez-Cendón, M., & Dumbser, M. (2021). A semi-implicit hybrid finite volume/finite element scheme for all Mach number flows on staggered unstructured meshes. *Applied Mathematics and Computation, 402*, Article 126117. https://doi.org/10.1016/j.amc.2021.126117

Cai, M., Kaiser, P. K., Tasaka, Y., & Minami, M. (2007). Determination of residual strength parameters of jointed rock masses using the GSI system. *International Journal of Rock Mechanics and Mining Sciences, 44*(2), 247–265. https://doi.org/10.1016/j.ijrmms.2006.07.005

Carlà, T., Farina, P., Intrieri, E., Botsialas, K., & Casagli, N. (2017). On the monitoring and early-warning of brittle slope failures in hard rock masses: Examples from an open-pit mine. *Engineering Geology, 228*, 71–81. https://doi.org/10.1016/j.enggeo.2017.08.007

Carlà, T., Farina, P., Intrieri, E., Ketizmen, H., & Casagli, N. (2018). Integration of ground-based radar and satellite InSAR data for the analysis of an unexpected slope failure in an open-pit mine. *Engineering Geology, 235*, 39–52. https://doi.org/10.1016/j.enggeo.2018.01.021

Carter, T. G., Lorig, L. J., Eberhardt, E., & de Graaf, P. J. H. (2023). Approaches for estimating slope breakback and stability longevity for closure of large open pits. In *Proceedings of the Rocscience International Conference* (RIC2023-TP-169, pp. 1–18). Toronto, Canada, April 24–26, 2023.

Castro, A., Mayorga, E., & Moreno, F. (2018). Comparison between the finite differences, finite volume and finite element methods for the modelling of convective drying of fruit slices. In *Proceedings of the 5th International Conference on Industrial Drying Science (IDS2018)*. https://doi.org/10.4995/ids2018.2018.7422

Chen, B. (2017). Finite element strength reduction analysis on slope stability based on ANSYS. *Environmental and Earth Sciences Research Journal, 4*(3), 60–65. https://doi.org/10.18280/eesrj.040302

Chen, C., Li, T., Ma, C., Zhang, H., Tang, J., & Zhang, Y. (2021). Hoek-Brown failure criterion-based creep constitutive model and BP neural network parameter inversion for soft surrounding rock mass of tunnels. *Applied Sciences, 11*(21), Article 10033. https://doi.org/10.3390/app112110033

Chen, J., Zhang, J., Wu, T., Hao, J., Wu, X., Ma, X., ... & Zhang, L. (2022). Activity and kinematics of two adjacent freeze–thaw-related landslides revealed by multisource remote sensing of Qilian Mountain. *Remote Sensing, 14*(19), Article 5059. https://doi.org/10.3390/rs14195059

Chen, W., Zhang, D., Fang, Q., Chen, X., & Xu, T. (2022). A new numerical finite strain procedure for a circular tunnel excavated in strain-softening rock masses and its engineering application. *Applied Sciences, 12*(5), Article 2706. https://doi.org/10.3390/app12052706

Chen, X., Liang, H., Zhang, J., Huang, W., Ren, L., & Zou, Y. (2019). Geochemical characteristics and oxidation states of the Xietongmen ore-bearing porphyries: Implication for the genetic types of the Xietongmen No. I and No. II deposits, southern Tibet. *Geological Journal, 55*(6), 4691–4712. https://doi.org/10.1002/gj.3712

Chen, Z. (2023). Influence of recirculation flow on the dispersion pattern of blasting dust in deep open-pit mines. *ACS Omega, 8*(34), 31353–31364. https://doi.org/10.1021/acsomega.3c03528

Colom, A., Agreda, E., & Pinyol, N. (2014). Modelling progressive failure with MPM. In *Proceedings of the 9th European Conference on Numerical Methods in Geotechnical Engineering* (pp. 319–323). CRC Press. https://doi.org/10.1201/b17017-58

Conte, E., Silvestri, F., & Troncone, A. (2010). Stability analysis of slopes in soils with strain-softening behaviour. *Computers and Geotechnics, 37*(5), 710–722. https://doi.org/10.1016/j.compgeo.2010.04.010

Davidsen, J., Goebel, T., Kwiatek, G., Stanchits, S., Ardanuy, J., & Dresen, G. (2021). What controls the presence and characteristics of aftershocks in rock fracture in the lab? *Journal of Geophysical Research: Solid Earth, 126*(10), Article e2021JB022539.

https://doi.org/10.1029/2021jb022539

Delonca, A., Gunzburger, Y., & Verdel, T. (2020). Cascade effect of rock bridge failure in planar rock slides: Explicit numerical modelling with a distinct element code. *Natural Hazards and Earth System Sciences Discussions*. https://doi.org/10.5194/nhess-2020-279

Delonca, A., Gunzburger, Y., & Verdel, T. (2021). Cascade effect of rock bridge failure in planar rock slides: Numerical test with a distinct element code. *Natural Hazards and Earth System Sciences, 21*(4), 1263–1278. https://doi.org/10.5194/nhess-21-1263-2021

Dick, G. J., Eberhardt, E., Cabrejo-Liévano, A. G., Stead, D., & Rose, N. D. (2015). Development of an early-warning time-of-failure analysis methodology for open-pit mine slopes utilizing ground-based slope stability radar monitoring data. *Canadian Geotechnical Journal, 52*(4), 515–529. https://doi.org/10.1139/cgj-2014-0028

Dintwe, T., Sasaoka, T., Shimada, H., Hamanaka, A., Moses, D., Liu, S., ... & Meng, F. (2021). Effects of sublevel open stope underground mining on surface and open pit slopes. *Journal of Geoscience and Environment Protection, 9*(1), 121–131. https://doi.org/10.4236/gep.2021.91010

Donati, D., Stead, D., Elmo, D., & Borgatti, L. (2019). A preliminary investigation on the role of brittle fracture in the kinematics of the 2014 San Leo landslide. *Geosciences, 9*(6), Article 256. https://doi.org/10.3390/geosciences9060256

Du, H., & Song, D. (2021). Failure prediction of open-pit mine landslide containing complex geological structure using inverse velocity method: A case study in West Open-Pit Mine, Pingzhuang, China. *Preprint on Research Square*.

https://doi.org/10.21203/rs.3.rs-573230/v1

Du, S., Saroglou, C., Chen, Y., Lin, H., & Rui, Y. (2022). A new approach for evaluation of slope stability in large open-pit mines: A case study at the Dexing copper mine, China. *Environmental Earth Sciences, 81*(3), Article 10223. https://doi.org/10.1007/s12665-022-10223-0

Du, W., Chen, L., He, Y., Wang, Q., Gao, P., & Li, Q. (2022). Spatial and temporal distribution of groundwater in open-pit coal mining: A case study from Baorixile coal mine, Hailaer Basin, China. *Geofluids, 2022*, Article 8753217, 1–17. https://doi.org/10.1155/2022/8753217

Durán, E., Adam, L., Wallis, I., & Barnhoorn, A. (2019). Mineral alteration and fracture influence on the elastic properties of volcaniclastic rocks. *Journal of Geophysical Research: Solid Earth, 124*(5), 4576–4600. https://doi.org/10.1029/2018jb016617

Eberhardt, E., Stead, D., & Coggan, J. S. (2004). Numerical analysis of initiation and progressive failure in natural rock slopes—the 1991 Randa rockslide. *International Journal of Rock Mechanics and Mining Sciences, 41*(1), 69–87. https://doi.org/10.1016/S1365-1609(03)00076-5

Eberhardt, E. (2008). Twenty-ninth Canadian Geotechnical Colloquium: The role of advanced numerical methods and geotechnical field measurements in understanding complex deep-seated rock slope failure mechanisms. *Canadian Geotechnical Journal, 45*(4), 484–510. https://doi.org/10.1139/T07-116

Eberhardt, E., Stead, D., & Loew, S. (2017). Progressive failure, rock mass fatigue and early warning applied to deep-seated rock slope failures. In *Proceedings of the Progressive*

Rock Failure Conference (pp. 144–145). Ascona, Switzerland.

Fang, T., Ren, F., Liu, H., Zhang, Y., & Cheng, J. (2022). Progress and development of particle jet drilling speed-increasing technology and rock-breaking mechanism for deep well. *Journal of Petroleum Exploration and Production Technology, 12*(6), 1697–1708. https://doi.org/10.1007/s13202-021-01443-4

Fereshtenejad, S., Kim, J., & Song, J. J. (2021). Experimental study on shear mechanism of rock-like material containing a single non-persistent rough joint. *Energies, 14*(4), Article 0987. https://doi.org/10.3390/en14040987

Flandes, N. (2023). The effect of weathering on the variation of geotechnical properties of a granitic rock from Chile. *Quarterly Journal of Engineering Geology and Hydrogeology, 56*(4), Article qjegh2023-022. https://doi.org/10.1144/qjegh2023-022

Frolova, Y., Litvinenko, V., Rogozhin, S., & Zverev, D. (2014). Effects of hydrothermal alterations on physical and mechanical properties of rocks in the Kuril–Kamchatka island arc. *Engineering Geology, 183*, 80–95. https://doi.org/10.1016/j.enggeo.2014.10.011

Froude, M., & Petley, D. N. (2018). Global fatal landslide occurrence from 2004 to 2016. *Natural Hazards and Earth System Sciences, 18*(8), 2161–2181. https://doi.org/10.5194/nhess-18-2161-2018

Galarce Castro, T. F. (2014). *Modelo de esfuerzos in-situ para Chile y su incidencia en el diseño minero subterráneo* [Master's thesis, Universidad de Chile]. Repositorio Académico Universidad de Chile. https://repositorio.uchile.cl/handle/2250/116331

Gao, W., Wang, X., Dai, S., & Chen, D. (2016). Numerical study on stability of rock slope based on energy method. *Advances in Materials Science and Engineering, 2016*, Article 2030238, 1–10. https://doi.org/10.1155/2016/2030238

Garza, R. A. P., Titley, S. R., & Pimentel B., F. (2001). Geology of the Escondida porphyry copper deposit, Antofagasta Region, Chile. *Economic Geology, 96*(2), 307–324. https://doi.org/10.2113/gsecongeo.96.2.307

Geng, J., Li, Q., Li, X., Zhou, T., Liu, Z., & Xie, Y. (2021). Research on the evolution characteristics of rock mass response from open-pit to underground mining. *Advances in Materials Science and Engineering, 2021*, Article 1–15. https://doi.org/10.1155/2021/2046913

Gong, C., Lei, S., Bian, Z., Liu, Y., Zhang, Z., & Cheng, W. (2019). Analysis of the development of an erosion gully in an open-pit coal mine dump during a winter freeze-thaw cycle by using low-cost UAVs. *Remote Sensing, 11*(11), Article 1356. https://doi.org/10.3390/rs11111356

Gong, L. (2021). Modelling of sensitivity of underground space stability to the in situ stress uncertainties: Case study at the Bukov Underground Research Facility Phase II (Rozna Mine, Czechia). *Acta Geodynamica et Geomaterialia, 18*(3), 319–334. https://doi.org/10.13168/agg.2021.0022

Goodfellow, R., & Dimitrakopoulos, R. (2013). Algorithmic integration of geological uncertainty in pushback designs for complex multiprocess open pit mines. *Mining Technology, 122*(2), 67–77. https://doi.org/10.1179/147490013X13639459465736

Google Earth Pro 7.3.6.9796 (64-bit). (02/27/2016). Northern Chile Region. 24° 15' 43.01"S, 69° 04' 15.52"W, Eye alt 7.1 km. Terrain Layer. Image © CNES/Airbus, 2016.

<http://www.google.com/earth/index.html > (Accessed 01/01/2021).

Google Earth Pro 7.3.6.9796 (64-bit). (03/05/2007). Northern Chile Region. 24° 15' 43.01"S, 69° 04' 15.52"W, Eye alt 7.1 km. Terrain Layer. Image © Maxar Technologies, 2007. <http://www.google.com/earth/index.html > (Accessed 01/01/2021).

Google Earth Pro 7.3.6.9796 (64-bit). (03/30/2019). Northern Chile Region. 24° 15' 47.55"S, 69° 04' 24.30"W, Eye alt 7.1 km. Terrain Layer. Image © CNES/Airbus, 2019. <http://www.google.com/earth/index.html > (Accessed 01/01/2021).

Google Earth Pro 7.3.6.9796 (64-bit). (06/02/2017). Northern Chile Region. 24° 15' 43.01"S, 69° 04' 15.52"W, Eye alt 7.1 km. Terrain Layer. Image © Maxar Technologies, 2017. <http://www.google.com/earth/index.html > (Accessed 01/01/2021).

Google Earth Pro 7.3.6.9796 (64-bit). (07/11/2013). Northern Chile Region. 24° 15' 43.01"S, 69° 04' 15.52"W, Eye alt 7.1 km. Terrain Layer. Image © CNES/Airbus, 2013. <http://www.google.com/earth/index.html > (Accessed 01/01/2021).

Google Earth Pro 7.3.6.9796 (64-bit). (11/25/2011). Northern Chile Region. 24° 15' 43.01"S, 69° 04' 15.52"W, Eye alt 7.1 km. Terrain Layer. Image © Maxar Technologies, 2011. <http://www.google.com/earth/index.html > (Accessed 01/01/2021).

Gowda, G., Dinesh, S., Govindaraju, L., & Babu, R. (2022). Effect of liquefaction-induced lateral spreading on seismic performance of pile foundations. *Civil Engineering Journal, 7*(Special Issue), 58–70. https://doi.org/10.28991/cej-sp2021-07-05

Grämiger, L., Moore, J. R., Gischig, V., Ivy-Ochs, S., & Loew, S. (2017). Beyond debuttressing: Mechanics of paraglacial rock slope damage during repeat glacial cycles.

Journal of Geophysical Research: Earth Surface, 122(4), 1004–1036. https://doi.org/10.1002/2016JF003967

Grenon, M., & Laflamme, A.-J. (2011). Inter-ramp and bench design of open-pit mines: The Portage pit case study. *Canadian Geotechnical Journal, 48*(11), 1601–1615. https://doi.org/10.1139/t11-062

Griffiths, D., & Marquez, R. (2007). Three-dimensional slope stability analysis by elasto-plastic finite elements. *Géotechnique, 57*(6), 537–546. https://doi.org/10.1680/geot.2007.57.6.537

Guo, H., Ye, A., Zhang, J., Zhou, Y., & Guo, Y. (2018). Impact of high-rise buildings construction process on adjacent tunnels. *Advances in Civil Engineering, 2018*, Article 5804051, 1–12. https://doi.org/10.1155/2018/5804051

Guo, Q., Pan, J., Cai, M., & Zhang, Y. (2020). Analysis of progressive failure mechanism of rock slope with locked section based on energy theory. *Energies, 13*(5), Article 1128. https://doi.org/10.3390/en13051128

Haghshenas, S., Haghshenas, S., Geem, Z., Kim, T., Mikaeil, R., Pugliese, L., & Troncone, A. (2021). Application of harmony search algorithm to slope stability analysis. Land, 10(11), *Article 1250*. https://doi.org/10.3390/land10111250

Haile, W., & Konka, B. (2021). Optimum open pit design for Kenticha tantalite mine, southern Ethiopia. *Momona Ethiopian Journal of Science, 13*(1), 147–163. https://doi.org/10.4314/mejs.v13i1.8

Han, F., & Tang, C. (2010). Numerical investigation for anisotropy of compressive strength of rock mass with multiple natural joints. *Journal of Coal Science and Engineering (China), 16*(3), 246–248. https://doi.org/10.1007/s12404-010-0305-4

He, J., Xu, X., Fu, Z., An, Y., Chen, T., Xie, Q., Chen, F., & Chen, F. (2021). Decoupling of Sr-Nd isotopic composition induced by potassic alteration in the Shapinggou porphyry Mo deposit of the Qinling–Dabie orogenic belt, China. *Minerals, 11*(8), Article 910. https://doi.org/10.3390/min11080910

Hervé, M., Sillitoe, R. H., Wong, C., Fernández, P., Crignola, F., Ipinza, M., & Urzúa, F. (2012). Geologic overview of the Escondida porphyry copper district, northern Chile. In *J. W. Hedenquist, M. Harris, & F. Camus (Eds.), Geology and genesis of major copper deposits and districts of the world: A tribute to Richard H. Sillitoe* (Special Publication No. 16). Society of Economic Geologists. https://doi.org/10.5382/SP.16.03

Hindy, Y. (2021). A quantum computational approach to the open-pit mining problem. *arXiv*. https://doi.org/10.48550/arxiv.2107.11345

Hoek, E., & Bray, J. D. (1981). *Rock slope engineering* (3rd ed.). CRC Press. https://doi.org/10.1201/9781482267099

Hoek, E., & Brown, E. T. (1997). Practical estimates of rock mass strength. *International Journal of Rock Mechanics and Mining Sciences, 34*(8), 1165–1186. https://doi.org/10.1016/S1365-1609(97)80069-X

Hoek, E., & Karzulovic, A. (2000). Rock mass properties for surface mines. In *W. A. Hustrulid, M. K. McCarter, & D. J. A. van Zyl (Eds.), Slope stability in surface mining* (pp. 59–70). Society for Mining, Metallurgy, and Exploration (SME).

Hoek, E., Rippere, K. H., & Stacey, P. F. (2001). Large-scale slope designs: A review of the state of the art. In *W. A. Hustrulid, M. K. McCarter, & D. J. A. van Zyl (Eds.), Slope stability in surface mining* (pp. 3–10). Society for Mining, Metallurgy, and Exploration (SME).

Holwell, D., & Jordaan, A. (2006). Three-dimensional mapping of the Platreef at the Zwartfontein South Mine: Implications for the timing of magmatic events in the northern limb of the Bushveld Complex, South Africa. *Applied Earth Science, 115*(2), 41–48. https://doi.org/10.1179/174327506X113046

Hong, Y., Shao, Z., Sun, G., Dou, Y., Wang, W., & Zhang, W. (2021). Freeze-thaw effects on stability of open pit slope in high-altitude and cold regions. *Geofluids, 2021*, Article 8409621, 1–10. https://doi.org/10.1155/2021/8409621

Hou, J., Zhang, R., & Kou, X. (2016). Analysis on foundation settlement and island wall deformation of offshore artificial island. *Japanese Geotechnical Society Special Publication, 2*(35), 1263–1266. https://doi.org/10.3208/jgssp.chn-23

Hou, Y., Wang, J. H., & Zhang, L. L. (2007). Three-dimensional numerical modeling of a deep excavation adjacent to Shanghai metro tunnels. In *Y. Shi, G. D. van Albada, J. Dongarra, & P. M. A. Sloot (Eds.), Computational science – ICCS 2007* (pp. 1164–1171). Springer. https://doi.org/10.1007/978-3-540-72588-6_184

Hryhoriev, Y., Lutsenko, S., Kuttybayev, A., Ermekkali, A., & Shamrai, V. (2023). Study of the impact of the open pit productivity on the economic indicators of mining development. *IOP Conference Series: Earth and Environmental Science, 1254*(1), Article 012050. https://doi.org/10.1088/1755-1315/1254/1/012050

Hu, B., Zhang, Q., Li, S., Yu, H., Wang, X., & Wang, H. (2022). Application of numerical simulation methods in solving complex mining engineering problems in Dingxi Mine, China. *Minerals, 12*(2), Article 123. https://doi.org/10.3390/min12020123

Hu, Y., Li, C., Li, J., Long, D., & Wang, Y. (2022). A slope stability-based realm optimization analysis for an open pit mine in a cold region: Taking Jiguanshan molybdenum mine as an example. *Geofluids, 2022*, Article 2150610, 1–12. https://doi.org/10.1155/2022/2150610

Huang, D., Cen, D., Ma, G., & Huang, R. (2014). Step-path failure of rock slopes with intermittent joints. *Landslides, 12*(5), 911–926. https://doi.org/10.1007/s10346-014-0517-6

Huang, X., Qi, S., Zheng, B., Guo, S., Liang, N., & Zhan, Z. (2020). Progressive failure characteristics of brittle rock under high-strain-rate compression using the bonded particle model. *Materials, 13*(18), 3943. https://doi.org/10.3390/ma13183943

Igwe, O. G., Sassa, K. Y., & Fukuoka, H. I. (2006). Excess pore water pressure: A major factor for catastrophic landslides. In *Proceedings of the 10th IAEG International Congress* (Paper No. 159, pp. 1-10). Nottingham, United Kingdom.

Itasca Consulting Group, Inc. (2019). *FLAC3D — Fast Lagrangian Analysis of Continua in Three-Dimensions* (Version 7.0). Minneapolis: Itasca.

Itasca Consulting Group, Inc. (2020). *Griddle* (Version 2.0). Minneapolis: Itasca.

Itasca Consulting Group, Inc. (2019a). *FLAC3D User manual.* Minneapolis: Itasca Consulting Group, Inc. Retrieved February 25, 2022, from https://docs.itascacg.com/flac3d700/contents.html

Jaboyedoff, M., Oppikofer, T., Abellán, A., Derron, M., Loye, A., Metzger, R., ... & Pedrazzini, A. (2010). Use of lidar in landslide investigations: A review. *Natural Hazards, 61*(1), 5-28. https://doi.org/10.1007/s11069-010-9634-2

Jiang, Y., Li, B., & Yamashita, Y. (2009). Simulation of cracking near a large underground cavern in a discontinuous rock mass using the expanded distinct element method. *International Journal of Rock Mechanics and Mining Sciences, 46*(1), 97-106. https://doi.org/10.1016/j.ijrmms.2008.05.004

Kaczmarzyk, M., Gawroński, M., & Piątkowski, G. (2018). Application of finite difference method for determining lunar regolith diurnal temperature distribution. *E3S Web of Conferences, 49*, 00052. https://doi.org/10.1051/e3sconf/20184900052

Keilegavlen, E., & Nordbotten, J. (2017). Finite volume methods for elasticity with weak symmetry. *International Journal for Numerical Methods in Engineering, 112*(8), 939-962. https://doi.org/10.1002/nme.5538

Kong, D., Bai, Y., Chen, Y., & Deng, M. (2019). A study on the seismic response characteristics of an oblique pile group-soil-structure with different pile caps. *Shock and Vibration, 2019*, 1-12. https://doi.org/10.1155/2019/8141045

Krivá, Z., & Mikula, K. (2002). An adaptive finite volume scheme for solving nonlinear diffusion equations in image processing. *Journal of Visual Communication and Image Representation, 13*(1-2), 22-35. https://doi.org/10.1006/jvci.2001.0502

Lees, A. (2016). *Geotechnical Finite Element Analysis*. ICE Publishing.

https://www.icevirtuallibrary.com/doi/book/10.1680/gfea.60876

Li, H. (2021). Study on the shape optimization of composite slope at the end of irregular boundary open-pit mine. *Converter,* 582-596. https://doi.org/10.17762/converter.88

Li, L., Wang, L., Zhou, X., Bai, Y., & Qiang, X. (2022). Study on deformation characteristics and instability failure mode of new suspended diaphragm wall deep excavation in soil-rock strata. *Advances in Technology and Design Engineering, 12*, 1-12. https://doi.org/10.3233/atde220929

Li, S., Zhao, Z., Hu, B., Yin, T., Chen, G., & Chen, G. (2022). Hazard classification and stability analysis of high and steep slopes from underground to open-pit mining. *International Journal of Environmental Research and Public Health, 19*(18), 11679. https://doi.org/10.3390/ijerph191811679

Lin, H.-D., Wang, W.-C., & Li, A.-J. (2020). Investigation of dilatancy angle effects on slope stability using the 3D finite element method strength reduction technique. *Computers and Geotechnics, 118*, 103295. https://doi.org/10.1016/j.compgeo.2019.103295

Locat, A., Jostad, H., & Leroueil, S. (2013). Numerical modeling of progressive failure and its implications for spreads in sensitive clays. *Canadian Geotechnical Journal, 50*(9), 961-978. https://doi.org/10.1139/cgj-2012-0390

Lopes, A., & Moura, M. (2019). The Tocantinzinho Paleoproterozoic porphyry-style gold deposit, Tapajós mineral province (Brazil): Geology, petrology and fluid inclusion evidence for ore-forming processes. *Minerals, 9*(1), 29. https://doi.org/10.3390/min9010029

López-Vinielles, J., Ezquerro, P., Merodo, J., Béjar-Pizarro, M., Monserrat, O., Barra, A., ... & Herrera, G. (2020). Remote analysis of an open-pit slope failure: Las Cruces case study, Spain. *Landslides, 17*(9), 2173-2188. https://doi.org/10.1007/s10346-020-01413-7

Lorig, L., & Varona, P. (2013). Guidelines for numerical modelling of rock support for mines. In *Proceedings of the Seventh International Symposium on Ground Support in Mining and Underground Construction* (pp. 81–105). https://doi.org/10.36487/ACG_rep/1304_04_Lorig

Lu, R., Wei, W., Shang, K., & Jing, X. (2020). Stability analysis of jointed rock slope by strength reduction technique considering ubiquitous joint model. *Advances in Civil Engineering, 2020*, 1-13. https://doi.org/10.1155/2020/8862243

Luan, L., Liu, Y., & Li, Y. (2015). Numerical simulation for the soil-pile-structure interaction under seismic loading. *Mathematical Problems in Engineering, 2015*, 1-7. https://doi.org/10.1155/2015/959581

Luo, Y., Wu, A., Liu, X., & Wang, H. (2004). Stability and reliability of pit slopes in surface mining combined with underground mining in Tonglushan mine. *Journal of Central South University of Technology, 11*(4), 434-439. https://doi.org/10.1007/s11771-004-0090-6

Luo, Z., Li, J., Qiao, J., Zhang, Y., Huang, Y., Assefa, E., ... & Deng, H. (2018). Effect of the water-rock interaction on the creep mechanical properties of the sandstone rock. *Periodica Polytechnica Civil Engineering*. https://doi.org/10.3311/ppci.11788

Lutton, R. J. (1970). Rock slope chart from empirical slope data. *Trans. Society of Mining Engineers, AIME, 247*, 160-162.

Macciotta, R., Creighton, A., & Martin, D. (2020). Design acceptance criteria for operating open-pit slopes: An update. *CIM Journal, 11*, 248–265. https://doi.org/10.1080/19236026.2020.1826830

Maiti, N., Pathak, P., & Samanta, B. (2021). An efficient algorithm for the precedence constraint knapsack problem with reference to large-scale open-pit mining pushback design. *Mining Technology, 130*(1), 8-21. https://doi.org/10.1080/25726668.2020.1866369

Maleki, M., Mahyar, M., & Meshkabadi, K. (2011). Design of overall slope angle and analysis of rock slope stability of Chadormalu mine using empirical and numerical methods. *Engineering, 3*(9), 965-971. https://doi.org/10.4236/eng.2011.39119

Mamot, P., Weber, S., Eppinger, S., & Krautblatter, M. (2020). Stability assessment of degrading permafrost rock slopes based on a coupled thermo-mechanical model. *Earth Surface Dynamics*. https://doi.org/10.5194/esurf-2020-70

Martin, C. D., & Chandler, N. A. (1994). The progressive fracture of Lac du Bonnet granite. *International Journal of Rock Mechanics and Mining Sciences & Geomechanics Abstracts, 31*(6), 643–659. https://doi.org/10.1016/0148-9062(94)90005-1

Mayne, P. W. (2015). In-Situ Geocharacterization of Soils in the Year 2016 and Beyond. In *Geotechnical Synergy in Buenos Aires 2015* (pp. 139–161). IOS Press. https://doi.org/10.3233/978-1-61499-599-9-139

McNeel, R., & others. (2020). *Rhinoceros 3D* (Version 7.0). Robert McNeel & Associates, Seattle, WA.

MEC Mining. (2022). *Five of the largest open-cut mines from around the world*. MEC Mining. Retrieved February 1, 2021, from https://www.mecmining.com.au/five-of-the-largest-open-cut-mines-from-around-the-world/

Meng, Q., Hu, X., Chen, G., Li, P., & Wang, Z. (2021). Estimation of the critical seismic acceleration for three-dimensional rock slopes. *Applied Sciences, 11*(24), 11625. https://doi.org/10.3390/app112411625

Miao, H., Zhao, N., Lixin, M., Zhang, Y., & Wang, L. (2023). Damage characteristics of weak rocks with different dip angles during creep. *Scientific Reports, 13*(1). https://doi.org/10.1038/s41598-023-34246-0

Mohammadi, S., & Taiebat, H. A. (2013). A large deformation analysis for the assessment of failure induced deformations of slopes in strain softening materials. *Computers and Geotechnics, 49*, 279–288. https://doi.org/10.1016/j.compgeo.2012.08.006

Molladavoodi, H., & RahimiRezaei, Y. (2018). Heterogeneous rock simulation using dip-micromechanics-statistical methods. *Advances in Civil Engineering, 2018*, 1-10. https://doi.org/10.1155/2018/7010817

Morales, M., & Panthi, K. (2017). Slope stability assessment of an open pit mine using three-dimensional rock mass modeling. *Bulletin of Engineering Geology and the Environment, 78*(2), 1249-1264. https://doi.org/10.1007/s10064-017-1175-4

McIntyre, J. S., & Hagan, T. N. (1976). The design of overburden blasts to promote highwall stability at a large strip mine. In *Proceedings of the 11th Canadian Rock Mechanics Symposium* (pp. 13–15). Vancouver.

Nishimura, T., Fukuda, T., & Tsujino, K. (2010). Distinct element analysis for progressive failure in rock slope. *Soils and Foundations, 50*(4), 505-513. https://doi.org/10.3208/sandf.50.505

Oberhollenzer, S., Tschuchnigg, F., & Schweiger, H. F. (2018). Finite element analyses of slope stability problems using non-associated plasticity. *Journal of Rock Mechanics and Geotechnical Engineering, 10*(6), 1091–1101. https://doi.org/10.1016/j.jrmge.2018.09.002

Oyebamiji, A., Afolayan, A., Mopa, B., & Tajudeen, O. (2019). Summary of modelling safety factors of slope stability in a tar-sand quarry: A case study. *Asian Journal of Applied Sciences, 7*(5). https://doi.org/10.24203/ajas.v7i5.5758

Pan, X., Jiang, T., Pan, P., Jia, Y., & Zhang, S. (2022). Experimental study on the relationship between the strength of altered rocks and the short wave-length infrared spectral curve. *arXiv*. https://doi.org/10.21203/rs.3.rs-2199466/v1

Papanikos, G., & Gousidou-Koutita, M. (2015). A computational study with finite element method and finite difference method for 2D elliptic partial differential equations. *Applied Mathematics, 6*(12), 2104-2124. https://doi.org/10.4236/am.2015.612185

Park, M., Han, H., & Jin, Y. (2021). Integrated analysis method for stability analysis and maintenance of cut-slope in urban. *IntechOpen*. https://doi.org/10.5772/intechopen.94252

Petley, D. (2020, February 4). Mina Pecket: A dramatic landslide in an open cast coal mine in 2014. *The Landslide Blog*. https://blogs.agu.org/landslideblog/2020/02/04/mina-pecket/

Petley, D. (2020, December 24). The deadly landslide at the Carmen Copper Mine in the Philippines. *The Landslide Blog*. https://blogs.agu.org/landslideblog/2020/12/24/carmen-copper-mine-1/

Potts, D., Dounias, G., & Vaughan, P. (1990). Finite element analysis of progressive failure of Carsington embankment. *Géotechnique, 40*(1), 79-101. https://doi.org/10.1680/geot.1990.40.1.79

Potts, D. M., Kovacevic, N., & Vaughan, P. R. (1997). Delayed collapse of cut slopes in stiff clay. *Géotechnique, 47*(5), 953–982. https://doi.org/10.1680/geot.1997.47.5.953

Preisig, G., Eberhardt, E., Smithyman, M., Preh, A., & Bonzanigo, L. (2016). Hydromechanical rock mass fatigue in deep-seated landslides accompanying seasonal variations in pore pressures. *Rock Mechanics & Rock Engineering, 49*(6), 2333-2351. https://doi.org/10.1007/s00603-016-0912-5

Premasiri, R. (2018). Modelling of rock slope failures due to geological discontinuties to minimize risk from road cut failures. *Journal of the Geological Society of Sri Lanka, 19*(2), 61. https://doi.org/10.4038/jgssl.v19i2.44

Puerta-Mejía, A.F., Deisman, N., Macciotta, R., O'Neil, S., and Eberhardt, E. (in press). Numerical modelling of progressive failure due to mine sequencing of a deep open pit slope: Importance of the geotechnical model in validating against a back-analysis. *Engineering Geology*.

Pysmennyi, S., Chukharev, S., Kyelgyenbai, K., Mutambo, V., & Matsui, A. (2022). Iron ore underground mining under the internal overburden dump at the PJSC "Northern GZK". *IOP Conference Series: Earth and Environmental Science, 1049*(1), 012008. https://doi.org/10.1088/1755-1315/1049/1/012008

Rafiei Renani, H., & Martin, C. D. (2018). Cohesion degradation and friction mobilization in brittle failure of rocks. *International Journal of Rock Mechanics and Mining Sciences, 106*, 1–13. https://doi.org/10.1016/j.ijrmms.2018.04.003

Rafiei Renani, H., & Martin, C. D. (2020a). Factor of safety of strain-softening slopes. *Journal of Rock Mechanics and Geotechnical Engineering, 12*(3), 473–483. https://doi.org/10.1016/j.jrmge.2019.11.004

Rafiei Renani, H., & Martin, C. D. (2020b). Slope stability analysis using equivalent Mohr–Coulomb and Hoek–Brown criteria. *Rock Mechanics and Rock Engineering, 53*(1), 13–21. https://doi.org/10.1007/s00603-019-01889-3

Rajmeny, P., Jain, P., & Vakili, A. (2016). 3D-numerical simulation of a mine using cohesion-softening, friction-softening, and hardening behavior. *Proceedings of the International Conference on Resource and Reserve Estimation (RARE 2016).* https://doi.org/10.2991/rare-16.2016.2

Rapiman, M., & Sepulveda, R. (2006). Slope optimization at Escondida Norte open pit. In *Proceedings of the Southern African Institute of Mining and Metallurgy* (pp. 265–278). The Southern African Institute of Mining and Metallurgy.

Read, J., & Stacey, P. (2009). *Guidelines for open pit slope design*. CSIRO Publishing.

https://doi.org/10.1071/9780643101104

Richer, B., Saeidi, A., Boivin, M., & Rouleau, A. (2020). Overview of retrogressive landslide risk analysis in sensitive clay slope. *Geosciences, 10*(8), Article 279. https://doi.org/10.3390/geosciences10080279

Rimmelin, R., & Vallejos, J. (2020). Rock mass behaviour of deep mining slopes: A conceptual model and implications. In *Proceedings of the 2020 International Symposium on Slope Stability in Open Pit Mining and Civil Engineering* (pp. 591–608). Australian Centre for Geomechanics. https://doi.org/10.36487/ACG_repo/2025_36

Riva, F., Agliardi, F., Amitrano, D., & Crosta, G. (2018). Damage-based time-dependent modeling of paraglacial to postglacial progressive failure of large rock slopes. *Journal of Geophysical Research: Earth Surface, 123*(1), 124–141. https://doi.org/10.1002/2017jf004423

Riveros, K., Veloso, E., Campos, E., Menzies, A., & Véliz, W. (2014). Magnetic properties related to hydrothermal alteration processes at the Escondida porphyry copper deposit, northern Chile. *Mineralium Deposita, 49*(6), 693–707. https://doi.org/10.1007/s00126-014-0514-7

Rose, N., & Hungr, O. (2007). Forecasting potential rock slope failure in open pit mines using the inverse-velocity method. *International Journal of Rock Mechanics and Mining Sciences, 44*(2), 308-320. https://doi.org/10.1016/j.ijrmms.2006.07.014

Roshankhah, S. (2022). Whole behavioral spectrum of jointed rock slopes. *In Proceedings of the PRF2022—Progressive Failure of Brittle Rocks conference* (Paper No. 7-4). Geological Society of America. Flat Rock, NC, USA. https://doi.org/10.1130/abs/2022pr-

376088

Roy, K., Hawlader, B., Kenny, S., & Moore, I. (2016). Finite element modeling of lateral pipeline–soil interactions in dense sand. *Canadian Geotechnical Journal, 53*(3), 490-504. https://doi.org/10.1139/cgj-2015-0171

Rupar, V., Čebašek, V., Milisavljevic, V., Stevanovic, D., & Živanović, N. (2021). Determination of mechanical properties of altered dacite by laboratory methods. *Minerals, 11*(8), 813. https://doi.org/10.3390/min11080813

Sakurai, S. (2017). *Back analysis in rock engineering* (1st ed.). CRC Press. https://doi.org/10.1201/9781315375168

Sazzad, M. M., Mamun, M., & Ibna Rahman, F. (2015, December 11). Effect of material model on the FEM based stability analysis of slope. *Proceedings of the International Conference on Civil, Structural, and Environmental Engineering (ICCSEE).*

Schmidt, R. (1985). *High-alumina hydrothermal systems in volcanic rocks and their significance to mineral prospecting in the Carolina slate belt*. U.S. Geological Survey Bulletin 1562. https://doi.org/10.3133/b1562

Scholtès, L., & Donzé, F. (2015). A DEM analysis of step-path failure in jointed rock slopes. *Comptes Rendus Mécanique, 343*(2), 155-165. https://doi.org/10.1016/j.crme.2014.11.002

Sdvyzhkova, O., Moldabayev, S., Bascetin, A., Babets, D., Kuldeyev, E., Sultanbekova, Z., ... & Issakov, B. (2022). Probabilistic assessment of slope stability at ore mining with steep layers in deep open pits. *Mining of Mineral Deposits, 16*(4), 11-18.

https://doi.org/10.33271/mining16.04.011

Shahin, M., Jaksa, M., & Maier, H. (2009). Recent advances and future challenges for artificial neural systems in geotechnical engineering applications. *Advances in Artificial Neural Systems, 2009*, 1-9. https://doi.org/10.1155/2009/308239

Sillitoe, R. (1973). The tops and bottoms of porphyry copper deposits. *Economic Geology, 68*(6), 799-815. https://doi.org/10.2113/gsecongeo.68.6.799

Sillitoe, R. (2010). Porphyry copper systems. *Economic Geology, 105*(1), 3-41. https://doi.org/10.2113/gsecongeo.105.1.3

Sjöberg, J. (1996). *Large scale slope stability in open pit mining: A review*. Retrieved from Luleå tekniska universitet website: https://urn.kb.se/resolve?urn=urn:nbn:se:ltu:diva-22512

Sjöberg, J. (2001). A slope height versus slope angle database. In *W. A. Hustrulid, M. A. Fox, & M. H. Potts (Eds.), Slope stability in surface mining* (pp. 47-58). Society for Mining, Metallurgy, and Exploration, Inc.

Sjöberg, J. (2001). Failure mechanisms for high slopes in hard rock. In *W. A. Hustrulid et al. (Eds.), Slope stability in surface mining* (pp. 71-80). Society for Mining, Metallurgy, and Exploration, Inc.

Sobko, B., Lozhnikov, O., Chebanov, M., & Vinivitin, D. (2022). Substantiation of the optimal parameters of the bench elements and slopes of iron ore pits. *Naukovyi Visnyk Natsionalnoho Hirnychoho Universytetu, (5)*, 26-32. https://doi.org/10.33271/nvngu/2022-5/026

Song, R., Wang, Y., Sun, S., Cui, M., & Li, J. (2020). Evaluation of elastoplastic properties of brittle sandstone at microscale using micro-indentation test and simulation. *Energy Science & Engineering, 8*(10), 3490-3501. https://doi.org/10.1002/ese3.759

Spross, J., Olsson, L., & Stille, H. (2017). The Swedish Geotechnical Society's methodology for risk management: A tool for engineers in their everyday work. *Georisk: Assessment and Management of Risk for Engineered Systems and Geohazards, 12*(3), 183-189. https://doi.org/10.1080/17499518.2017.1416643

Spross, J., Olsson, L., Stille, H., Hintze, S., & Båtelsson, O. (2021). Risk management procedure to understand and interpret the geotechnical context. *Georisk: Assessment and Management of Risk for Engineered Systems and Geohazards, 16*(2), 235-250. https://doi.org/10.1080/17499518.2021.1884883

Stacey, T. R., Xianbin, Y., Armstrong, R., & Keyter, G. (2003). New slope stability considerations for deep open pit mines. *Journal of the Southern African Institute of Mining and Metallurgy, 103*(6), 373-389.

Stead, D., Eberhardt, E., & Coggan, J. S. (2006). Developments in the characterization of complex rock slope deformation and failure using numerical modelling techniques. *Engineering Geology, 83*(1-3), 217-235. https://doi.org/10.1016/j.enggeo.2005.06.033

Stock, G., Martel, S., Collins, B., & Harp, E. (2012). Progressive failure of sheeted rock slopes: The 2009–2010 Rhombus Wall rock falls in Yosemite Valley, California, USA. *Earth Surface Processes and Landforms, 37*(5), 546-561. https://doi.org/10.1002/esp.3192

Strauhal, T., & Zangerl, C. (2021). The impact of fracture persistence and intact rock bridge failure on the in situ block area distribution. *Applied Sciences, 11*(9), 3973. https://doi.org/10.3390/app11093973

Stupnik, M. (2023). Scientific and technical problems of transition from open pit to combined technologies for raw materials mining. *IOP Conference Series: Earth and Environmental Science, 1254*(1), 012070. https://doi.org/10.1088/1755-1315/1254/1/012070

Error! Reference source not found.

Taji, M., Ataei, M., Goshtasbi, K., & Osanloo, M. (2012). ODM: A new approach for open pit mine blasting evaluation. *Journal of Vibration and Control, 19*(11), 1738-1752. https://doi.org/10.1177/1077546312439911

Tang, H., & Chen, S. (2016). Cosserat continuum model and its application to the studies of progressive failure. *Japanese Geotechnical Society Special Publication, 2*(18), 703-708. https://doi.org/10.3208/jgssp.chn-57

Tang, H., Guan, Y., Xue, Z., & Zou, D. (2017). Low-order mixed finite element analysis of progressive failure in pressure-dependent materials within the framework of the Cosserat continuum. *Engineering Computations, 34*(2), 251-271. https://doi.org/10.1108/ec-11-2015-0370

Tian, G., Tang, L., Wei, H., & Wu, Q. (2016). The composite ground finite layer method and its application to pile foundation analysis. *Latin American Journal of Solids and Structures, 13*(13), 2393-2413. https://doi.org/10.1590/1679-78252668

Toderas, M., & Filatiev, M. (2021). Slopes stability analysis from Rosia Poieni open pit mine, Romania. *MATEC Web of Conferences, 342*, 02005.

https://doi.org/10.1051/matecconf/202134202005

Traykovski, P., Richardson, M., Mayer, L., & Irish, J. (2007). Mine burial experiments at the Martha's Vineyard Coastal Observatory. *IEEE Journal of Oceanic Engineering, 32*(1), 150-166. https://doi.org/10.1109/joe.2007.890956

Trivedi, A. (2010). Strength and dilatancy of jointed rocks with granular fill. *Acta Geotechnica, 5*(1), 15–31. https://doi.org/10.1007/s11440-009-0095-2

Troncone, A. (2005). Numerical analysis of a landslide in soils with strain-softening behaviour. *Géotechnique, 55*(8), 585-596. https://doi.org/10.1680/geot.2005.55.8.585

Troncone, A., Conte, E., & Pugliese, L. D. P. (2019). Analysis of the slope response to an increase in pore water pressure using the material point method. *Water, 11*(7), 1446. https://doi.org/10.3390/w11071446

Tschuchnigg, F., Medicus, G., & Schneider-Muntau, B. (2019). Slope stability analysis: Barodesy vs linear elastic–perfectly plastic models. *E3S Web of Conferences, 92*, 16014. https://doi.org/10.1051/e3sconf/20199216014

Tu, J., Zhang, Y., Mei, G., & Xu, N. (2021). Numerical investigation of progressive slope failure induced by sublevel caving mining using the finite difference method and adaptive local remeshing. *Applied Sciences, 11*(9), 3812. https://doi.org/10.3390/app11093812

Tuheteru, E., Gautama, R., Kusuma, G., Kuntoro, A., Pranoto, K., & Palinggi, Y. (2021). Water balance of pit lake development in the equatorial region. *Water, 13*(21), 3106. https://doi.org/10.3390/w13213106

Valdivia, C., & Lorig, L. (2001). Slope stability at Escondida mine. In W. A. Hustrulid, R. L. Bullock, & J. F. M. (Eds.), *Slope stability in surface mining* (pp. 153-162). Society for Mining, Metallurgy, and Exploration, Inc.

Wang, G., & Sassa, K. (2008). Seismic loading impacts on excess pore-water pressure maintain landslide triggered flowslides. *Earth Surface Processes and Landforms, 34*(2), 232-241. https://doi.org/10.1002/esp.1708

Wang, G., Sun, F., & Tang, Q. (2018). Reliability analysis of rock slope excavation considering the stochasticity and finite persistence of wedges. *Periodica Polytechnica Civil Engineering*. https://doi.org/10.3311/ppci.11806

Wang, H., Zhao, W., Sun, D., & Guo, B. (2012). Mohr-Coulomb yield criterion in rock plastic mechanics. *Chinese Journal of Geophysics, 55*(6), 733-741. https://doi.org/10.1002/cjg2.1767

Wang, M., Zhou, J., Shi, A., Han, J., & Li, H. (2020). Key factors affecting the deformation and failure of surrounding rock masses in large-scale underground powerhouses. *Advances in Civil Engineering, 2020*, 1-20. https://doi.org/10.1155/2020/8843466

Ward, J. (2015). *Bingham Canyon Landslide: Analysis and Mitigation* [Thesis]. https://scholarworks.unr.edu//handle/11714/410

Wei, Y., Lundberg, A., & Resare, F. (2019). Systematic slope stability assessment through deformation field monitoring. *E3S Web of Conferences, 92*, 18009. https://doi.org/10.1051/e3sconf/20199218009

Wu, Q., Kou, Z., & Wan, S. (2012). Numerical simulation for the effect of joint inclination on the stability of stratified rock slopes. *Proceedings of the International Conference on Civil, Architectural and Structural Engineering*, 8. https://doi.org/10.2991/iccasm.2012.8

Wu, R., Li, Z., Zhang, W., Hu, T., Xiao, S., Xiao, Y., ... & Ming, C. (2023). Stability analysis of rock slope under sujiaba overpass in chongqing city based on kinematic and numeric methods. *Frontiers in Earth Science*, 11. https://doi.org/10.3389/feart.2023.1181949

Wu, R., Li, Z., Zhang, W., Hu, T., Xiao, S., Xiao, Y., ... & Ming, C. (2023). Stability analysis of rock slope under Sujiaba overpass in Chongqing city based on kinematic and numeric methods. *Frontiers in Earth Science*, 11. https://doi.org/10.3389/feart.2023.1181949

Wyllie, D. C., & Mah, C. W. (2017). *Rock slope engineering: Civil and mining* (4th ed.). Taylor & Francis.

Xiong, H., Yin, Z., & Nicot, F. (2019). A multiscale work-analysis approach for geotechnical structures. *International Journal for Numerical and Analytical Methods in Geomechanics, 43*(6), 1230-1250. https://doi.org/10.1002/nag.2893

Yang, X., & Zou, J. (2009). Estimation of compaction grouting pressure in strain softening soils. *Journal of Central South University of Technology, 16*(4), 653-657. https://doi.org/10.1007/s11771-009-0108-1

Yan-hui, S., Feng, M., & Chen, P. (2022). Modified rock slope equivalent Mohr-Coulomb strength parameters satisfying the Hoek-Brown criterion. *Research Square*. https://doi.org/10.21203/rs.3.rs-1899609/v1

Ye, G., Zhang, F., Yashima, A., Sumi, T., & Ikemura, T. (2005). Numerical analyses on progressive failure of slope due to heavy rain with 2D and 3D FEM. *Soils and Foundations, 45*(2), 1-15. https://doi.org/10.3208/sandf.45.2_1

Yerro, A., Pinyol, N., & Alonso, E. (2015). Internal progressive failure in deep-seated landslides. *Rock Mechanics and Rock Engineering, 49*(6), 2317-2332. https://doi.org/10.1007/s00603-015-0888-6

Yu, B., Zeng, Q., Wang, Y., He, H., & Su, F. (2017). The sources of ore-forming fluids from the Jinchang gold deposit, Heilongjiang Province, NE China: Constraints from the He–Ar isotopic evidence. *Resource Geology, 67*(3), 330-340. https://doi.org/10.1111/rge.12131

Yu, Y. S., & Coates, D. F. (1979). Canadian experience in simulating pit slopes by the finite element method. In *Developments in Geotechnical Engineering* (Vol. 14, pp. 709-758). Elsevier.

Yuan, L., Li, C., Li, S., Xiangsong, M., Zhang, W., Liu, D., ... & Hou, X. (2022). Mine slope stability based on fusion technology of InSAR monitoring and numerical simulation. *Scientific Programming, 2022*, 1-10. https://doi.org/10.1155/2022/8643586

Zangerl, C., Schneeberger, A., Steiner, G., & Mergili, M. (2021). Geographic-information-system-based topographic reconstruction and geomechanical modelling of the Köfels rockslide. *Natural Hazards and Earth System Science, 21*(8), 2461-2483. https://doi.org/10.5194/nhess-21-2461-2021

Zareifard, M. (2020). Ground reaction curve for deep circular tunnels in strain-softening Mohr–Coulomb rock masses considering the damaged zone. *International Journal of Geomechanics, 20*(10). https://doi.org/10.1061/(asce)gm.1943-5622.0001822

Zhan, Q., Sun, X., Li, C., Yong, Z., Zhou, X., He, Y., ... & Zhang, Y. (2019). Stability analysis and reinforcement of a high-steep rock slope with faults: Numerical analysis and field monitoring. *Advances in Civil Engineering, 2019*, 1-8. https://doi.org/10.1155/2019/3732982

Zhang, H., Tao, P., Meng, X., Liu, M., & Liu, X. (2021). An optimum deployment algorithm of camera networks for open-pit mine slope monitoring. *Sensors, 21*(4), 1148. https://doi.org/10.3390/s21041148

Zhang, H., Wu, Y., Huang, S., Zheng, L., & Miao, Y. (2022). Analysis of flexural toppling failure of anti-dip rock slopes due to earthquakes. *Frontiers in Earth Science, 9*. https://doi.org/10.3389/feart.2021.831023

Zhang, J., Tang, W., & Zhang, L. (2010). Efficient probabilistic back-analysis of slope stability model parameters. *Journal of Geotechnical and Geoenvironmental Engineering, 136*(1), 99-109. https://doi.org/10.1061/(asce)gt.1943-5606.0000205

Zhang, K., Cao, P., & Bao, R. (2013). Progressive failure analysis of slope with strain-softening behaviour based on strength reduction method. *Journal of Zhejiang University Science A, 14*(2), 101-109. https://doi.org/10.1631/jzus.a1200121

ZHANG, M., Yuan, Q., Chen, J., Fan, J., Jiang, D., & Lu, D. (2023). Role of temperature effect on the strength deterioration of wet shotcrete in cold area construction. *Research Square*. https://doi.org/10.21203/rs.3.rs-2510627/v1

Zhang, Y., Bandopadhyay, S., & Liao, G. (1989). An analysis of progressive slope failures in brittle rocks. *International Journal of Surface Mining, Reclamation and Environment, 3*(4), 221–227. https://doi.org/10.1080/09208118908944278

Zhang, Y., Chen, C., Lei, M., Zheng, Y., Zhang, H., & Shao, Y. (2020). Preliminary numerical analysis of a novel retaining system in dry sandy soil and its first application to a deep excavation in Wuhan (China). *Applied Sciences, 10*(6), 2006. https://doi.org/10.3390/app10062006

Zhang, Y., Guo, J., Ou, Q., Liu, S., & Wang, L. (2021). Study on the catastrophic evolution of Tianshan road slope under the freeze-thaw cycles. *Geofluids, 2021*, 1-12. https://doi.org/10.1155/2021/6128843

Zhang, Y., Zhang, J., & Ma, J. (2022). Stability analysis of a steep rock slope in a large open-pit mine in a high-intensity area: A case study of the Yejiagou boron iron mine. *Geofluids, 2022*, 1-14. https://doi.org/10.1155/2022/9113173

Zhou, Z., Shen, Y., & Chen, Z. (2021). Failure of rock slopes with intermittent joints: Failure process and stability calculation models. *Preprints*. https://doi.org/10.21203/rs.3.rs-731901/v1

Appendix: Details about the calibration process

The following procedures apply to each of the models enclosed in blue in Figure 3-8, which define models with different geological and material model complexity levels (from Homogeneous to lithologies+alterations and Elastic Perfectly Plastic to Strain Softening, respectively). It is essential to say that models with a linear elastic material model with different geological model complexity levels, as they do not accumulate plastic deformations, cannot reproduce the case study observed failure in Chapter 3. However, as will be shown, they serve for numerical modelling correctness verifications.

For each defined plastic model in Figure 3-8, in Rhinoceros 3D V. 7.0., McNeel, R., & others. (2020), and deploying the commands and tools there, we constructed a geometric model constrained to the assumptions mentioned in numeral 3.10.1 (Model Characteristics and Assumptions) regarding model limits, actual pushback sequencing, pushback slope shape, and pre-mining terrain model. It is essential to mention that a Rhino 3D geometrical model to be further successfully meshed and imported into FLAC3D must be a closed watertight group of either surfaces or poly surfaces, where these cannot intercept each other. No repeated surfaces in model regions (like neighbour regions delimiting different materials or excavation blocks); see Figure 7-1 showing watertight surfaces, where each colour represents an enclosed region.

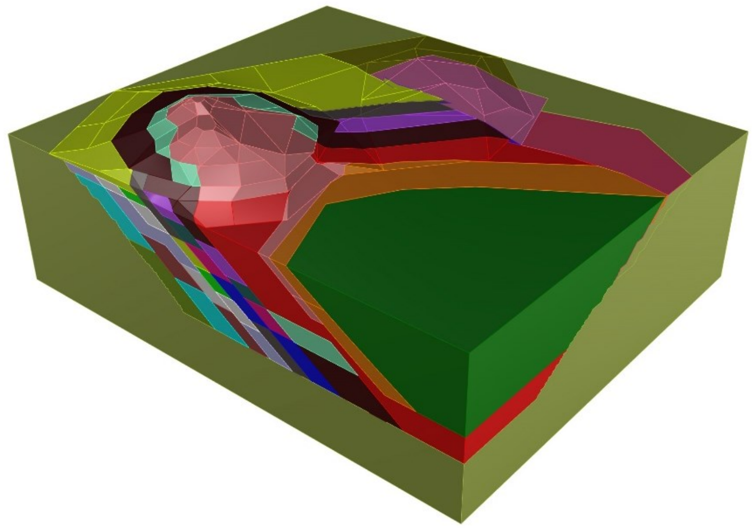

Figure 7-1. Rhino 3D model (Isometric View) comprised of surfaces and poly-surfaces enclosing watertight regions.

Once the latter is complete, Rhino's built-in command to create an initial mesh can be used. The initial mesh is a source of Griddle v.2.0 (Itasca's plug-in embedded in Rhino) to first, based on the desired mesh element size and type (see numeral 3.10.1), create a more suitable FLAC3D surface mesh (re-meshing of the previously created surfaces and poly-surfaces), and after, make a volumetric mesh (filling voids among surfaces). The volumetric mesh in the thesis body shows a tetrahedral element (Figure 3-12). Tetrahedral elements were selected because of their flexibility to accommodate the excavation shape, pushback sequence mining out blocks form, and the irregularity of the regions defined by each of the lithological and alteration regions. The element size chosen, ranging from 25 to 100 meters, guarantees more accuracy in the failed region and a smooth transition to less interesting areas.

The final optimal mesh for the FLAC3D model is without defects and has adequate shape and aspect ratio elements. Cracks, gaps, voids, holes, uneven or unmatched element nodes, repeated elements, self-intercepted elements, and twisted or degenerated elements (for example, elements with very acute angles or sharp elements) are considered no-allowed defects that must be fixed. Figure 7-2 shows some examples of this type of defect and others, according to Attene et al. (2013).

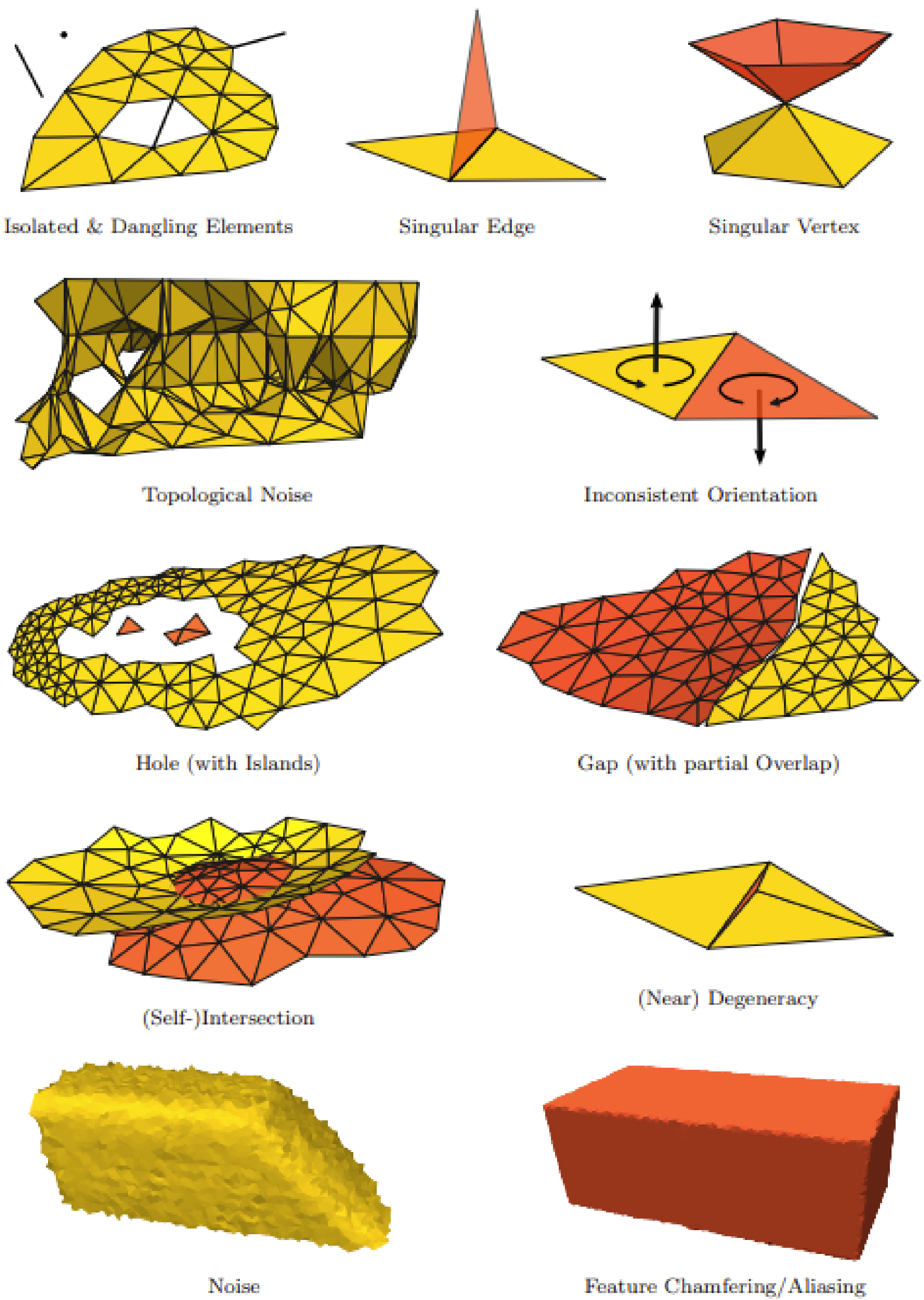

Figure 7-2. Illustration of the various types of flaws and defects that can occur in polygon meshes. Taken from Attene et al (2013).

The recommendations and criteria in the Griddle user manual were followed to avoid these defects: Griddle Utilities for Working with Surface Meshes, Griddle V. 2.0., Itasca Consulting Group, Inc. (2020). As a recommendation, the Griddle verification tool must be used first (GHeal command). Their automatic fixer tool eliminates most of the issues, and then, finally, the user can make manual reparations with other Rhino tools and commands for meshes. Unfortunately, this is a very time-consuming process, but it is fundamental to avoid most of the further issues when running models in FLAC3D, which will be treated later when talking about the model calibration process.

A meshed model, complying with previous requirements, is the starting point for setting up the model's analysis configuration in FLAC3D. In FLAC3D, the following characteristics are set:

- Set model stages: This refers to assigning the sequences in which the different blocks of the excavated material will be mined. In this case, it assigns the actual excavation sequence with the assumptions made per numerals 3.10 and 3.10.1 mentioned.
- Boundary Conditions: These were assigned as fixed in any direction at the model's sides and bottom because the model's extent and size ensure no interference with the ongoing stress distribution as the excavation progresses (see Figure 3-11 and Figure 3-12).
- Set In-Situ Stress condition: To represent better the tectonic environment where the case study is immersed, recommendations according to the stress ratio from Galarce (2014) were followed. As the effects of the pre-mining stresses are out of the scope of the present work, the K coefficient was uniformly applied to the entire model and its materials for simplicity. See numerals 3.6 and 3.10 about model characteristics and assumptions.
- Set material constitutive models: Among research work objectives is not the assessing of choosing different constitutive models and their effects on reproducing the observed failure. For simplicity, the Mohr-Coulomb material

model was selected. By choosing this, it would be more manageable to tune up parameters during calibration and reproduce the failure. Additionally, since the observed failure, according to the failure mechanism presented in numeral 3.9, describes a slip surface about 90 meters below the slope surface through the rock mass and shear rupture, the quoted model represents this well.

- Set material properties: For the first time running, these correspond to those properties from Table 3-2 for each previously defined model type in Figure 3-8. In case the model required residual strength parameters, these were initially estimated to be between 37% and 51% of the peak ones, according to Cai et al. (2007), as stated in numeral 3.10.

The previous encompasses the model type definition and models' set-up steps shown in Figure 3-8 and Figure 3-9, which are requirements for the calibration step in Figure 3-10. The objective of this research stage is to reproduce the actual failure mechanism on each model type, the six defined at the beginning (H-EPP, Lit-EPP, Lit+Alt-EPP, H-SS, Lit-SS, Lit+Alt-SS). The calibration of each model comprises the following:

An elastic run is undergone for each model using parameters in Table 3-2. The elastic run for each model serves to verify that on each model stage or pushback, the model calculates deformations and stresses, the mining out of the implemented pushback sequencing corresponds to the one defined in Figure 3-11 (b), and that throughout the several pushbacks, no stress concentrations or excessive deformations are present in the model, like, for example, the one shown in Figure 7-3. Additionally, each of these stages, where excavations do not perturb stresses, must show a distribution according to the pre-mining state, which increases with depth but also exhibits deformations towards where the material has been removed. See Figure 7-4 and Figure 7-5 with the expected stress distributions and Figure 7-6 and Figure 7-7 for displacements as related previously. This type of feature represents what is called coherent results in the thesis in Figure 3-10. If the model achieves the previous, it is now ready for a plastic run; if not, this suggests that there are issues with the mesh or any of the model configurations, and they must be sorted out before running a plastic analysis.

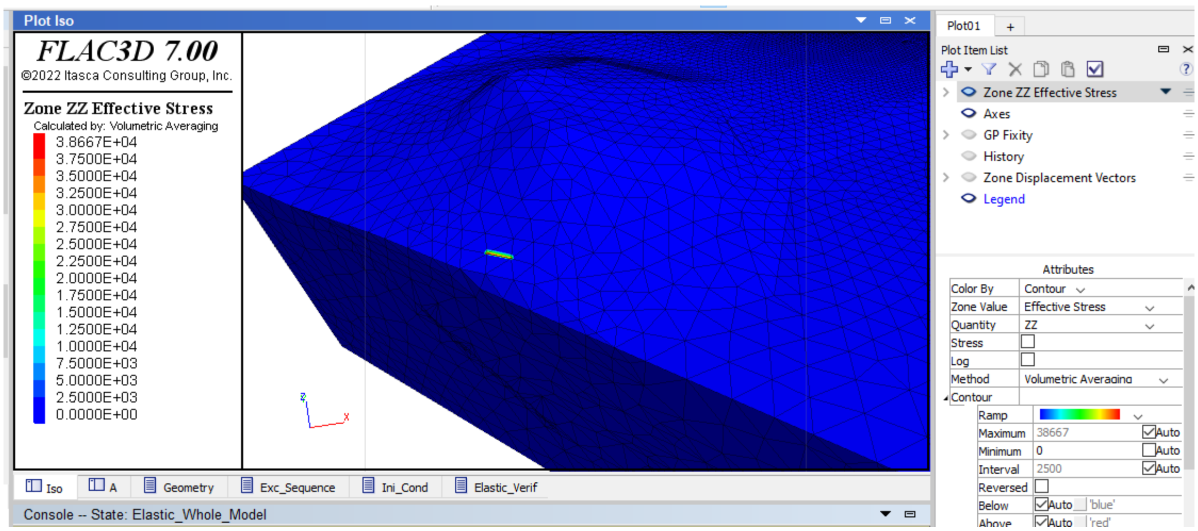

Figure 7-3. Spotted stress concentration after an elastic running at a previous to open-pit excavation stage.

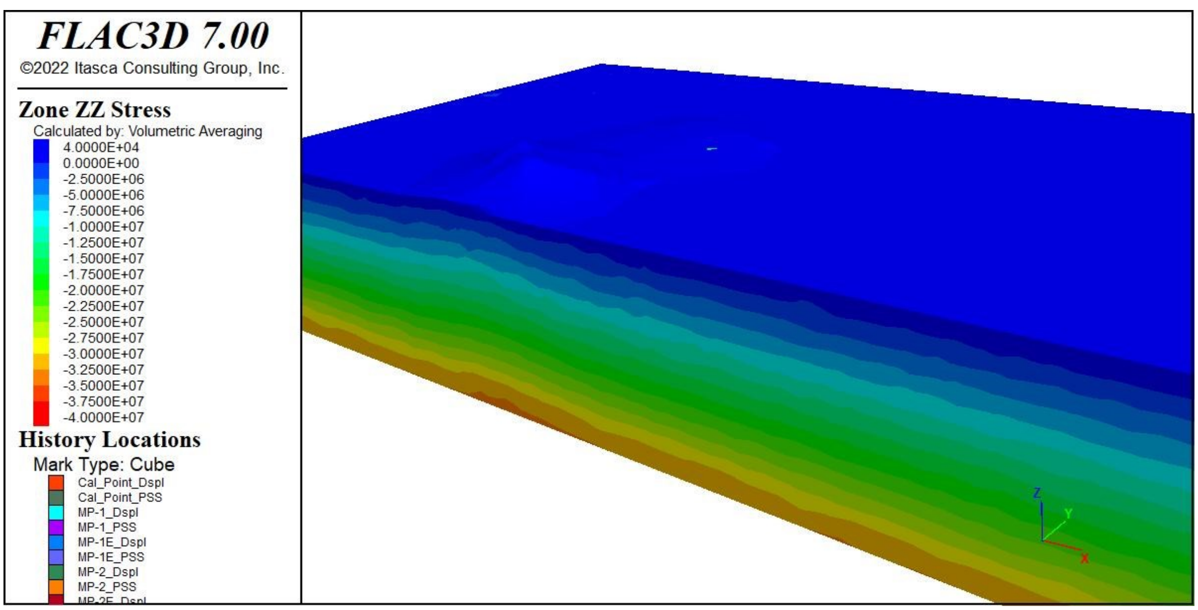

Figure 7-4. Elastic run showing vertical stresses increasing at depth. The stage is previous to any pushback excavation in the open-pit.

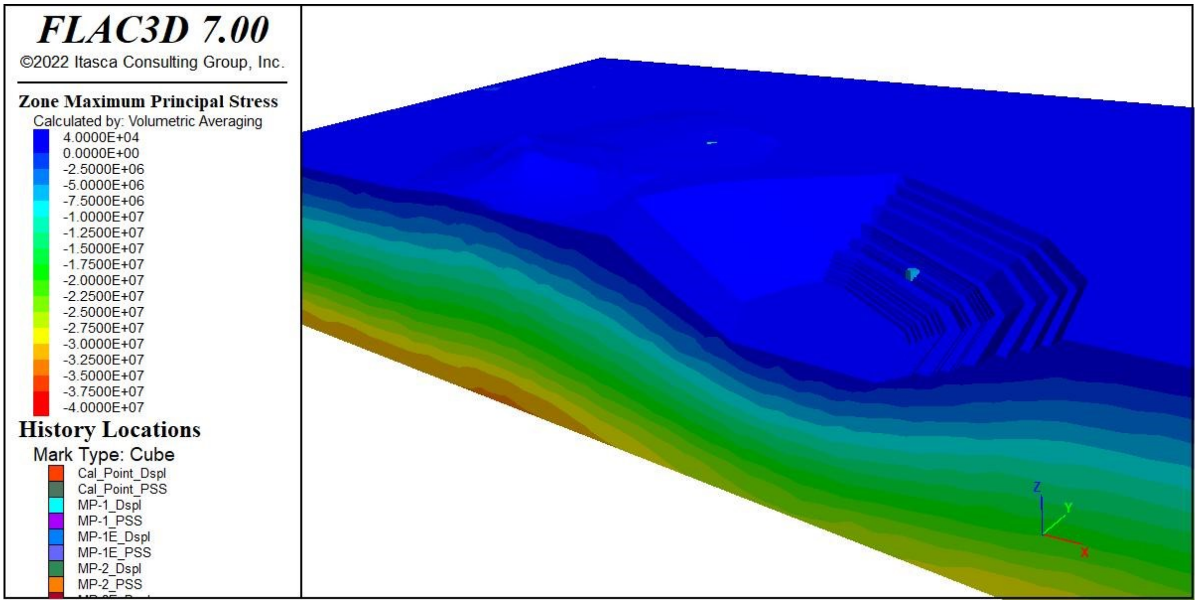

Figure 7-5. Elastic run showing maximum principal stresses increasing at depth and redistributed by a pushback excavation.

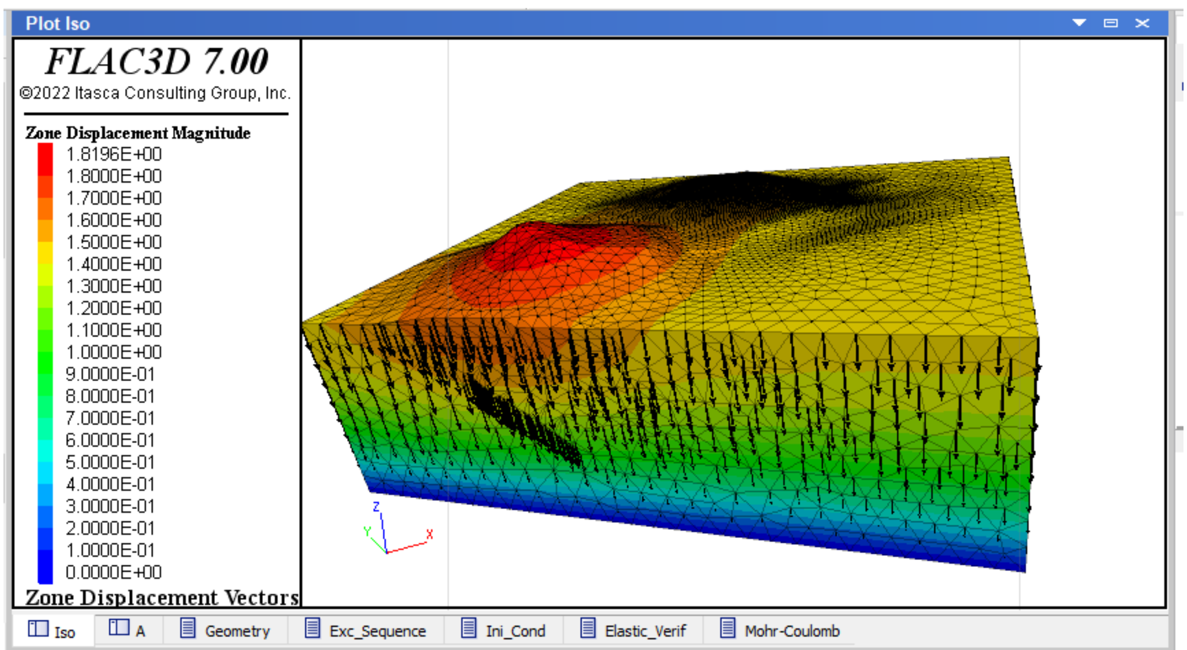

Figure 7-6. Elastic run showing displacement settlements with vectors before any open-pit pushback excavation.

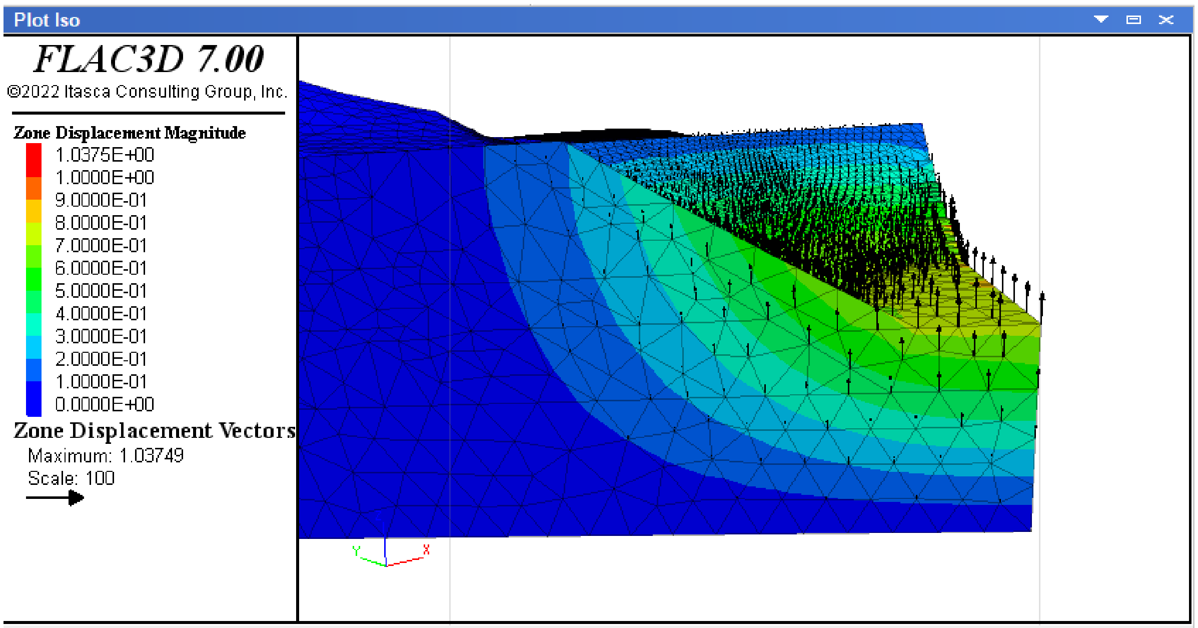

Figure 7-7. Elastic run showing displacement (Elastic rebound) with vectors at an open-pit pushback excavation.

For the models compliant with the coherency of results from the elastic run, the next step encompasses the iterative process of producing a failure as close as possible to actual failure characteristics in numeral 3.9 (Figure 3-6 and Figure 3-7). This was done by tunning up key model parameters starting from those in Table 3-2 (initial parameters) depending on the material model type (EPP or SS).

For EPP models, Mohr-Coulomb resistance parameters (C and f, referred to herein as cohesion and friction angle or Phi, respectively) and dilatancy angle (ψ) / dilation angle for every material were modified, depending on the results (three parameters to adjust per model material). For EPP models, the tension resistance was a dependent parameter and varied depending on the cohesion value assigned to the material; it was supposed to be 10% of the cohesion.

For those deploying SS models, the depending on results tunned up parameters were the peak and residual values for cohesion, friction angle, the peak dilation angle, and the plastic strain at which residual behaviour starts (critical strain parameter, ε_crit) for every one of the materials intervening in the model (Five parameters to vary per model's material). For all models, the material deformation moduli did not vary in any way from those defined initially in Table 3-2. The following considerations were also followed during the calibration process:

- If plastic run produces failure at any pushback in areas other than the actual affected area (mainly at the isometric view), this indicates that resistance parameters in those areas must be higher than initially supposed. Parameters then increased to the minimum needed to avoid failure in the regions quoted.
- If no failure is observed at nowhere within the model domain at any pushback, this indicates that resistance parameters for the outer actual failure area are probably okay but not for the material involved in the actual failure or at the indeed failed zone. Hence, materials at the actual failure zone must be decreased to allow failure to come up.
- Runnings exhibiting failure at any pushback with closer characteristics to the ones shown in numeral 3.9 (description of the case study progressive failure event) must be refined to match as closely as the criteria in Table 3-3 (calibration criteria) by following these additional criteria:

    - Either for EPP or SS models, yielded material depth extent is controlled by C and Phi peak resistance and residual parameters, respectively. The higher the C, the more profound and circular the failure. Conversely, higher Phi with low cohesion produces shallower slope surfaces. An example of the effect of varying C and Phi parameters on failure surface geometrical characteristics is depicted in Figure 7-8.

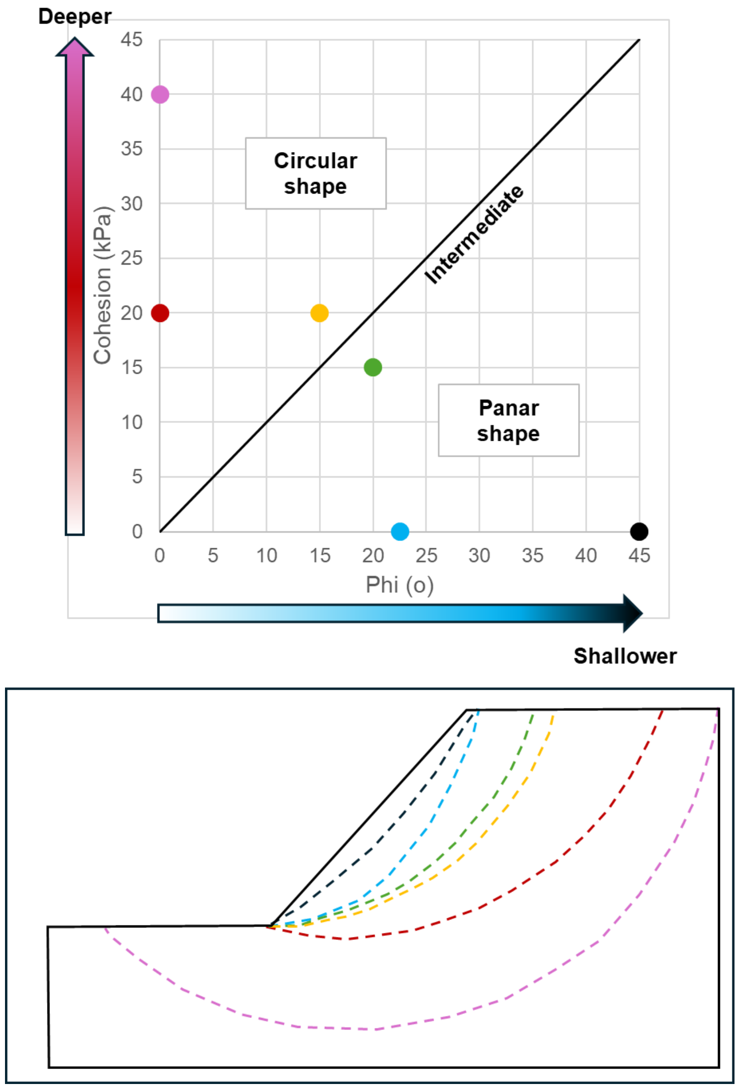

Figure 7-8. Schemme showing different C and Phi combinations and their effects regarding slip surface shape and position.

- The timing of failure must match the criteria in Table 3-3 and the displacement history plot for the CP monitoring point presented at the numeral 3.9, falling between the boundary limits presented in Figure 3-6. To do so, the following recommendations were deployed:
  - For EPP models, timing can only be roughly modified by C and Phi parameters. The lower the resistance parameters, the sooner failure starts. However, this also impacts failure location and

other geometric characteristics. Additionally, in an indirect fashion, dilation can make materials harder to flow artificially, slowing the plastic failure and material-yielding propagation, which can slow down the onset of failure. See Figure 7-9, which schematically shows the effect of varying the material's peak dilation angle on the onset of failure timing and failure extent.

- In SS models, there is more control over the onset of failure timing and afterwards propagation. Other than peak resistance values, for the onset of failure timing, likewise EPP models, the plastic deformation at which residual parameters (for C, Phi, dilation, tension resistance), the critical strain, controls post-peak material behaviour. The lower the critical strain values, the faster the materials' yielding propagation after the onset of failure. In contrast, if critical strain increases, the failure propagation can be slowed down; see Figure 7-10. The post-failure curve shape also influences the previous; see comparative examples in Figure 7-11.

Overall, parameter changes depend on the results of a case study numerical modelling assessment. However, they must be within the materials' feasible boundaries. Figure 7-9 and Figure 7-12 illustrate the feasible boundaries for materials parameters of the present case study grouped by the main lithological bodies (Andesite, Stockwork, and Rhyolite).

Figure 7-13 to Figure 7-15 present a hypothetical example of a three-material model employing an SS material model and illustrate how parameters are changed based on results to adjust the modelled failure to an actual failure. This procedure, but involving several more steps until the model was calibrated, was applied to each of the six model types shown in Figure 3-8 in the thesis body.

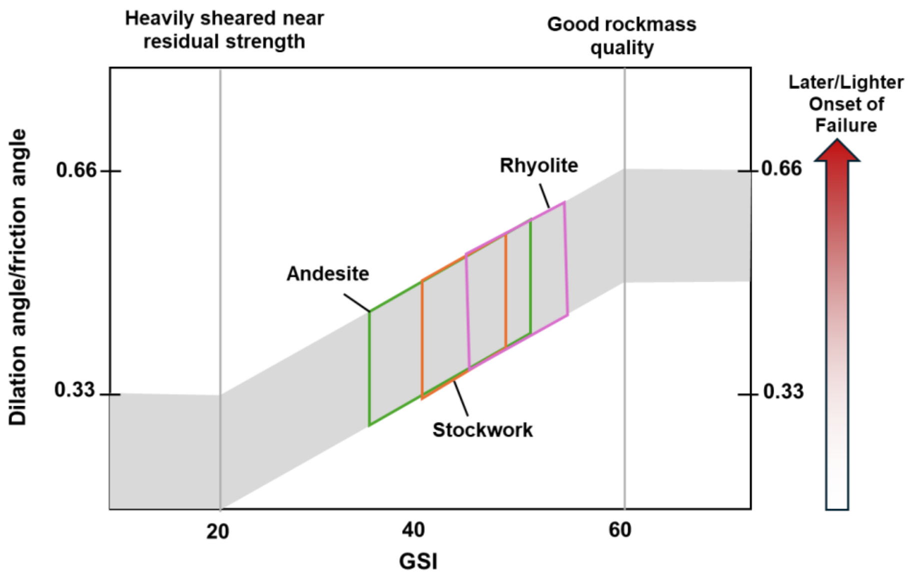

Figure 7-9. A plot of recommended dilation angle to friction angle relationships according to GSI material values from Lorig and Varona (2013) guidelines for the numerical assessment of underground structures. Enclosed are the values considered for the main lithologies for the present case study. The plot also depicts the effect of varying dilatancy on the model´s failure development.

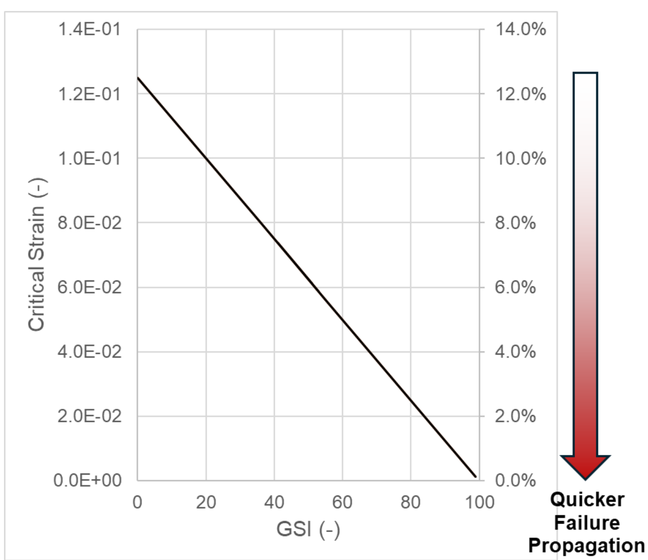

critical strain = (12.5 – 0.125 × GSI) / (100)

Figure 7-10. A plot of recommended critical strain relationships according to GSI material values, from Lorig and Varona (2013) guidelines to underground structures numerical assessment. The plot also depicts the effect of varying critical strain on the model´s failure development.

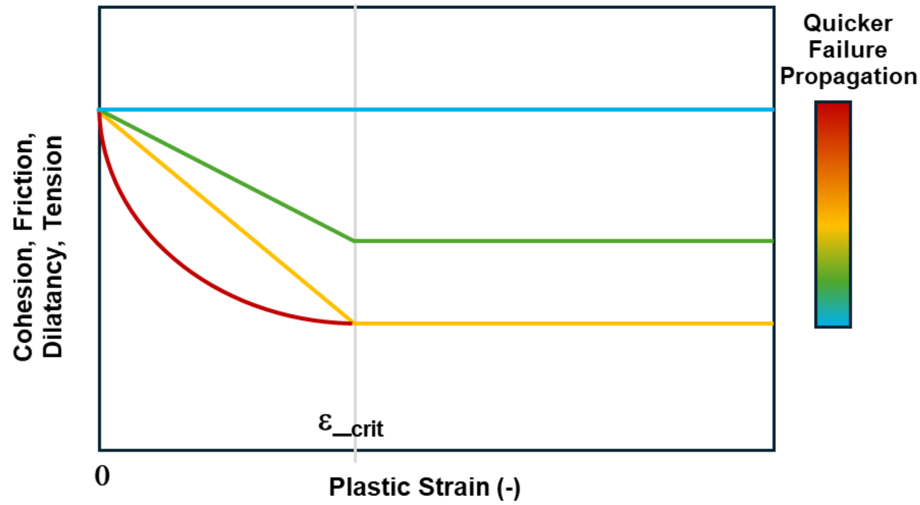

Figure 7-11. Plot depicting the effect of different post-peak degradation parameters shape curves on the model´s failure development.

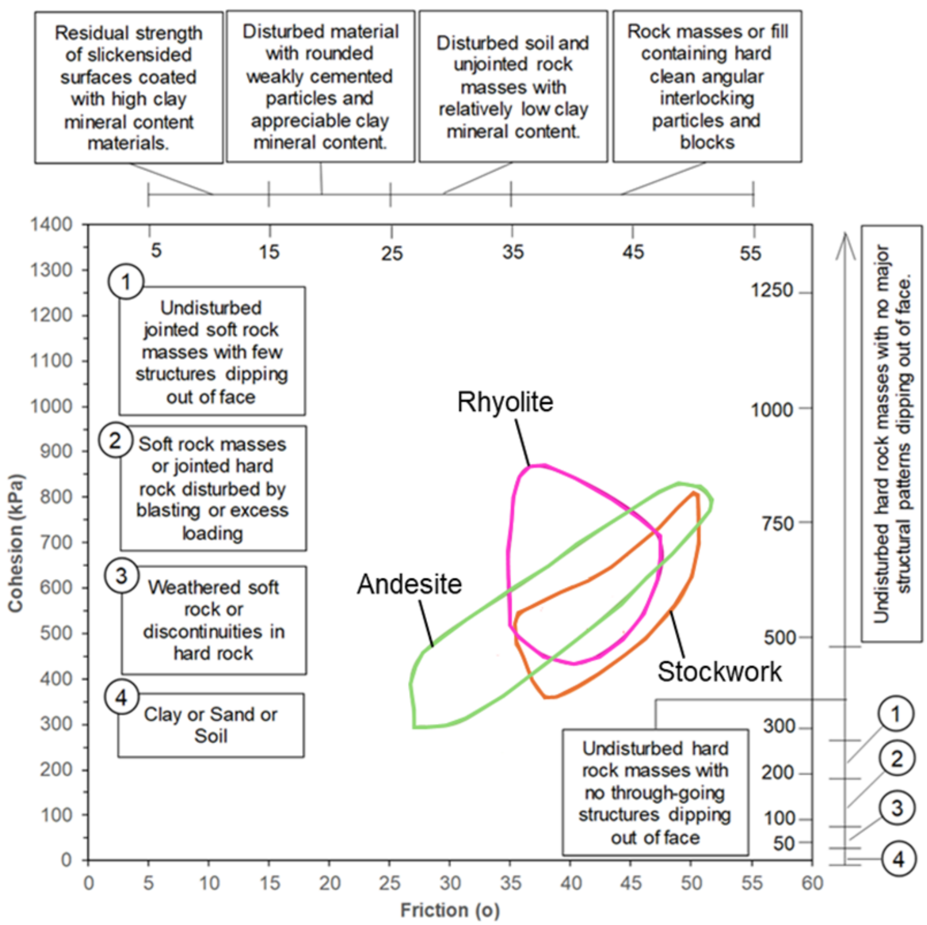

Figure 7-12. Plot of typical values obtained in previous studies involving porphyry deposit lithologies (modified from Wyllie & Mah, 2017 after Hoek & Bray, 1981).

In Figure 7-13, a) Isometric view of an open pit with three lithologies, failure surficial extent (dashed line) and monitoring point (blue dot) and cross profile location (A – A black line); b) A – A cross profile view showing lithology distribution, monitoring point location and slip surface characteristics (black dashed line); c) History plot comparing monitoring point throughout pushbacks displacements (blue line) with regards actual movement (dot and dashed lines); d) Adopted initial peak resistance parameters (triangular dot for rhyolite, circular dot for andesite, and squared dot for stockwork) with regards allowable material ranges; e) Adopted peak dilation angles (dots following previous conventions) compared with materials allowable values for the present case study in thesis body; f) Horizontal scale showing how far from the quickest failure propagation are the adopted materials critical strain (dotted points following previous conventions).

In Figure 7-14, a) Isometric view of an open pit with three lithologies, failure surficial extent (dashed line) and monitoring point (blue dot) and cross profile location (A – A black line), the failure extent is highlighted in red with a dashed line contour; b) A – A cross profile view showing lithology distribution, monitoring point location, actual slip surface characteristics (black dashed line), and obtained slip surface (dashed red line); c) History plot comparing monitoring point throughout pushbacks displacements (red line) with regards previous calibration step (grey line) and actual movement (dot and dashed lines); d) Adjusted peak resistance parameters (triangular dot for rhyolite, circular dot for andesite, and squared dot for stockwork) with regards allowable material ranges, previous adopted are in grey; e) Adopted peak dilation angles (dots following previous conventions) compared with materials allowable values for the present case study in thesis body, and previous in grey colour; f) Horizontal scale showing how far from the quickest failure propagation are the adjusted materials critical strain values (dotted points following previous conventions and previous values in grey colour).

In Figure 7-15, a) Isometric view of an open pit with three lithologies, failure surficial extent (dashed line) and monitoring point (blue dot) and cross profile location (A – A black line), the failure extent is highlighted in red with a dashed line contour; b) A – A cross profile view showing lithology distribution, monitoring point location, actual slip surface characteristics (black dashed line), and obtained slip surface (dashed red line); c) History plot comparing monitoring point throughout pushbacks displacements (red line) with regards previous calibration step (grey line) and actual movement (dot and dashed lines); d) Adjusted peak resistance parameters (triangular dot for rhyolite, circular dot for andesite, and squared dot for stockwork) with regards allowable material ranges, previous adopted are in grey; e) Adopted peak dilation angles (dots following previous conventions) compared with materials allowable values for the present case study in thesis body, and previous in grey colour; f) Horizontal scale showing how far from the quickest failure propagation are the adjusted materials critical strain values (dotted points following previous conventions and previous values in grey colour).

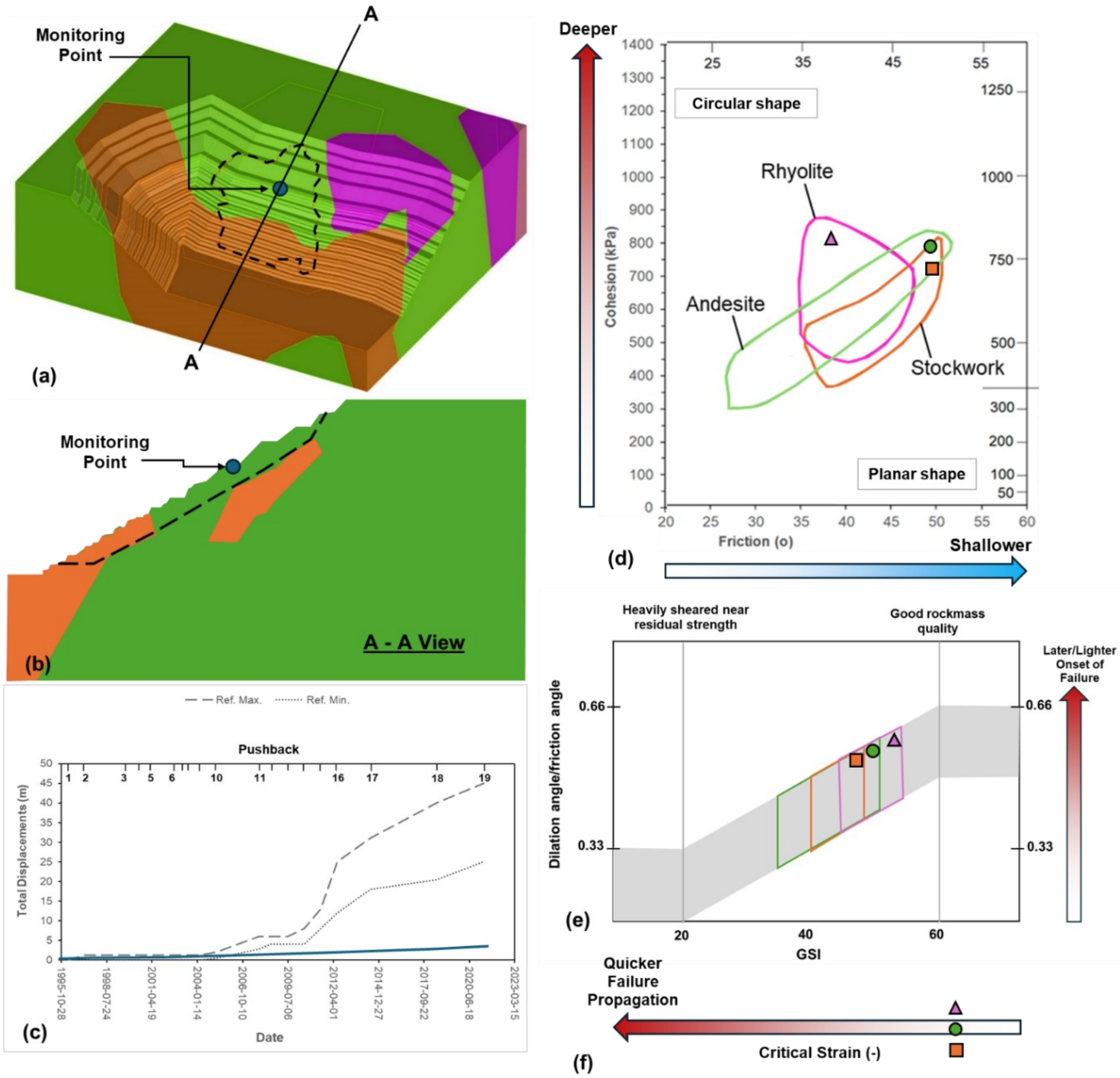

Figure 7-13. Scheme showing results of a hypothetical plastic run for an SS-type model after applying initial geomechanical parameters where no significant displacements or failure is produced.

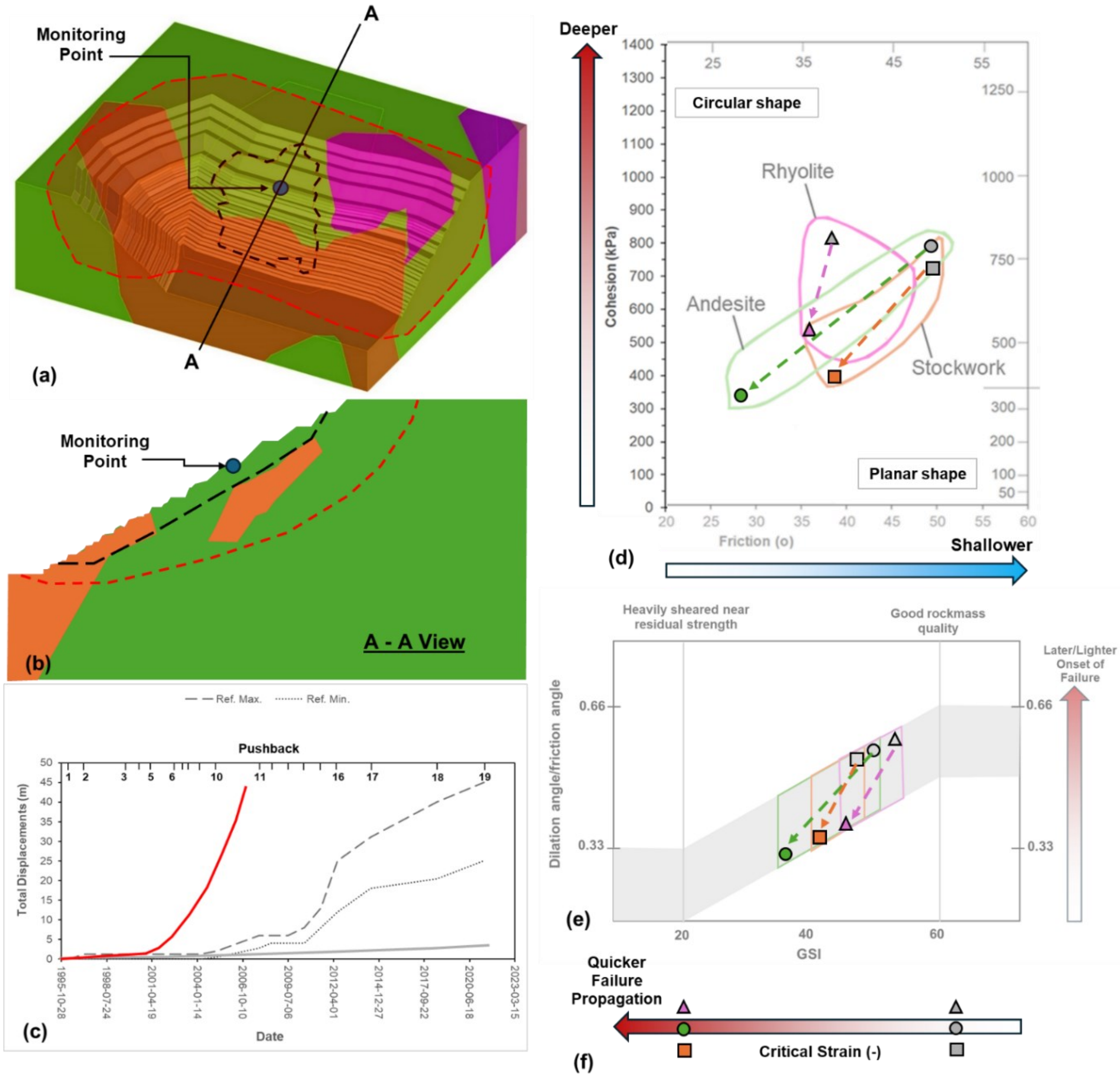

Figure 7-14. Scheme showing results of a hypothetical plastic run for a SS type model after applying adjusts to the initial geomechanical parameters in Figure 7-13, at this time significant displacements or failure is produced. Previous adopted parameters are represented as grey dots.

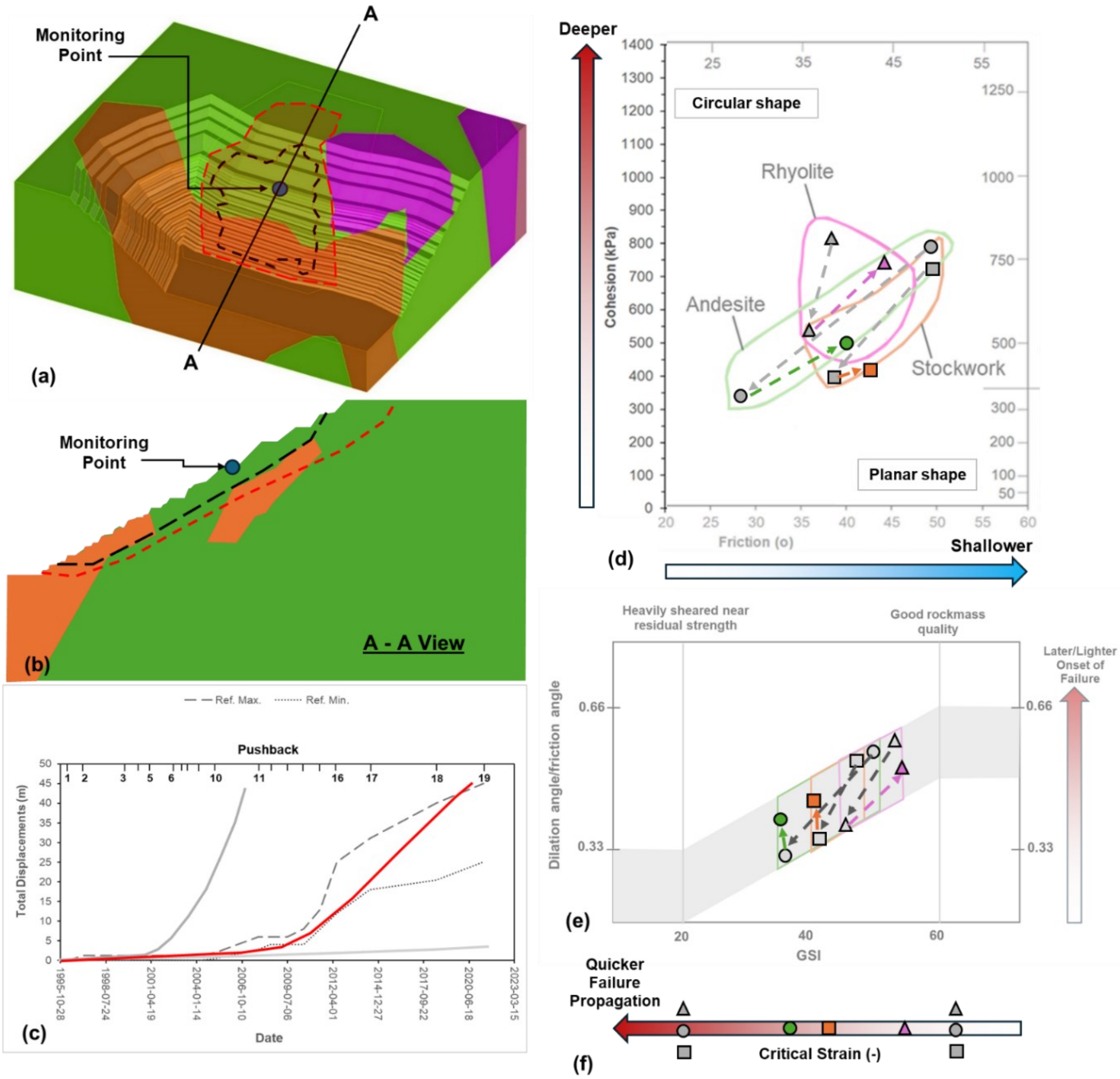

Figure 7-15. Scheme showing results of a hypothetical plastic run for an SS-type model after applying adjusts to the previous step in Figure 7-14; at this time, failure is close to the actual characteristics. Previously adopted parameters are represented as grey dots.